universität
wien

MASTERARBEIT / MASTER'S THESIS

Titel der Masterarbeit / Title of the Master's Thesis

„Ponderomotive Phase Modulation within a Modified Scanning Electron Microscope"

verfasst von / submitted by

Lucas Aaron Grandits BSc BSc

angestrebter akademischer Grad / in partial fulfilment of the requirements for the degree of

Master of Science (MSc)

Wien, 2023 / Vienna, 2023

Studienkennzahl lt. Studienblatt / degree programme code as it appears on the student record sheet:	UA 066 876
Studienrichtung lt. Studienblatt / degree programme as it appears on the student record sheet:	Masterstudium Physik
Betreut von / Supervisor:	Assoz. Prof. Dipl.-Ing. Dr. Thomas Juffmann

Acknowledgements

I would like to express my sincerest gratitude to all those who have supported and contributed to the completion of this research and my thesis, be it either through scientific or moral support.

First and foremost, I want to thank my supervisor Thomas Juffmann for giving me the opportunity to work on this project and for his help all along the way. While certain tasks such as PSF analysis, image processing with Fiji, and relativistic analysis of the theory were carried out individually, the majority of the work was conducted collaboratively as a team. Thus, I want to thank my amazing colleagues Marius-Constantin Chirita-Mihaila, Philipp Weber, and Matthias Schneller. All of them showed a tremendous amount of effort and dedication for this project, and I was lucky to be able to work with them.

Outside of my scientific field, I want to give my special thanks to my family and friends, especially Peter, Manuel, Jan, and George, for proofreading, showing genuine interest in this project, and for fruitful discussions.

Abstract

The intersection of electrons and light opens up exciting possibilities in ultrafast electron microscopy, quantum control of electrons, and advanced imaging techniques. In this thesis, the method of electron wave-front shaping in free space through the use of laser-generated ponderomotive potentials is presented, based on our publication [1]. Ponderomotive electron wave-front shaping enables the creation of both convex and concave electron lenses with a focal length similar to that of modern electron microscopes. Additionally, nearly any desired electron deflection pattern can be achieved by shaping the ponderomotive potentials with a spatial light modulator. Thus, programmable almost arbitrary electron wave-front shaping is realized.

Kurzfassung

Im Zusammenspiel von Elektronen und Licht eröffnen sich faszinierende Möglichkeiten in den Bereichen der ultraschnellen Elektronenmikroskopie, der quantenbasierten Kontrolle von Elektronen und in fortschrittlichen Abbildungsmethoden. In dieser Studie wird die Methode der Elektronenwellenfrontformung im freien Raum durch lasergenerierte ponderomotorische Potenziale vorgestellt, die auf unserer Veröffentlichung [1] basiert. Durch die ponderomotorische Elektronenwellenfrontformung können sowohl konvexe als auch konkave Elektronenlinsen mit einer Brennweite erzeugt werden, die vergleichbar mit modernen Elektronenmikroskopen ist. Darüber hinaus kann durch Formen des ponderomotorischen Potenzials mit einem räumlichen Lichtmodulator nahezu jedes gewünschte Elektronenbündelmuster erreicht werden. Dies ermöglicht eine programmierbare, fast beliebige Elektronenwellenfrontformung.

Contents

1. Introduction

In 1924, Louis de Broglie proposed the idea that not only light but also matter could exhibit both wave-like and particle-like behavior [2]. This idea was confirmed through experiments conducted by Davisson and Germer in 1927, which showed electron diffraction on a nickel crystal lattice [3]. De Broglie's theory has since led to the development of several devices and experiments that use matter, such as electrons and atoms, for various applications. One of the most important adaptations from light to matter was the creation of the electron microscope [4].

The precise control of electrons has enabled the development of electron microscopes that have transformed materials science [5] and structural biology [6]. One important technology for this is aberration correction [7], which allows for atomic-resolution imaging and wave-front engineering [8]. In light optics, mirror arrays and so-called spatial light modulators are used to gain programmable wave-front control [9]. This has led to significant advances in fields such as astronomy, deep-tissue imaging, and optical information processing. However, this level of control is not yet available in electron optics, despite its potential applications in areas such as random-probe ptychography [10], structure identification [11], and phase contrast microscopy [12].

Several techniques have been developed to control electron wave-fronts. Transmission of electron beams through sculpted material thin films has shown the ability to shape electron waves [13], leading to applications in aberration correction [14], orbital angular momentum manipulation [15], and contrast enhancement in biological imaging [16]. Yet, since this technique is based on the interaction between electrons and nano-structures, problems like electron loss, charging, and material aging remain.

Nano-fabrication has also enabled beam-shaping devices based on tunable electro- and magnetostatic potentials [17]. Such devices already enable tasks like symmetry mapping [18] or electron orbital momentum sorting [19]. Due to the tunable nature of the potentials, they also offer more flexibility than sculpted thin films. However, limitations such as electron loss, diffraction, charging, and beam-induced deterioration still exist.

Electron waves can also be shaped by optical fields near matter [20], enabling attosecond coherent control of the electron wave function[21] and multidimensional nano-scale imaging and spectroscopy [22]. Nevertheless, these methods are still impacted by inelastic scattering and material deterioration.

The control of electrons in free space through ponderomotive interaction with light avoids many of these challenges [1] and has been used to characterize [23] and create [24] ultrashort electron pulses, modulate the spectrum [25] and phase [26] of electron beams. Free electron-photon interactions are described by ponderomotive forces. Ponderomotive forces are second-order effects of the interaction Hamiltonian [27] since the first order of the interaction Hamilton vanishes due to an energy-momentum mismatch of the electron-photon coupling. This mismatch forbids single photon emission and absorption by free electrons, and thus, only an even number of virtual photon events is possible within this interaction [28].

The presented research demonstrates controllable transverse shaping of free electrons using the ponderomotive potential of a spatially modulated light pulse [1]. The theoretical framework outlined in Chapter 2 entails both the semi-classical (Chapter 2.4) and quantum description (Chapter 2.5) of ponderomotive interactions between electrons and light. In Chapter 3, the various equipment and its implementation are detailed. The research results are presented in Chapter 4. Chapter 5 offers a comprehensive discussion of the results, and the outlook and conclusion are presented in Chapter 6.

2. Theory

In 1924, Louis de Broglie suggested in his dissertation "Recherches sur la theorie des quanta" [2] that not only light but also matter can be described as a particle and a wave. The connection from particle to wave is provided by the now famous de Broglie wavelength, which is only dependent on the momentum of the particle p together with the Planck constant h:

$$\lambda_{dB} = \frac{h}{p} \tag{2.1}$$

Only three years later, his theory was experimentally verified when Davisson and Germer showed electron diffraction on a crystal lattice of nickel [3].

Since then, numerous different devices and ideas adapted from light experiments have been proposed and built, using matter like electrons, atoms, ions, or molecules. One of the most important adaptations from light to matter was the electron microscope [4]. An electron microscope provides a system of free electrons traversing through a vacuum characterized by boundary conditions (microscope type, detection mechanism, etc.), electron properties (pulse properties, coherence, etc.), and measurement outcomes (electron count, etc.).

Similar to the description of the wave nature of light, the description of a wave packet of free electrons within an electron microscope can be related to its longitudinal, spectral and transverse properties. Having accurate control over these properties within an electron microscope is crucial for atomic-scale imaging [29], spectroscopy [30], material sciences [5], and cryogenic microscopy [6].

The longitudinal properties of an electron beam include its pulse length (for pulsed beams) and its frequency. Control over the longitudinal properties of an electron beam in the femtosecond domain via coherent control techniques allows for the investigation of structural and excitation dynamics [31].

Spectral properties are related to the electron energy, which determines the de Broglie wavelength, the electron velocity and the mean free path in materials. Thus, control over the energy is of utter importance in electron microscopy. Furthermore, the electron energy and total density, i.e. the intensity, have to be considered for radiation damage and transmission through the sample [32].

Transverse properties of the electron beam are associated to the transverse profile of the wave packet, i.e. the electron wave-front. The transverse profile is mostly governed by aberrations, which the electron beam inevitably accumulates throughout the electron microscope column. Of these, spherical aberrations have one of the biggest impacts on the electron beam profile in traditional electron microscopes. As Scherzer already mentioned in 1936 [33], static, energy preserving and circularly symmetric electron lenses unavoidably impose spherical aberrations onto an electron beam. Correcting for these spherical aberrations, as well as further possible aberrations, is a task in electron microscopy, which has been thoroughly studied and improved over decades. Yet, it still calls for better and better aberration correction designs to gain better resolution while using less electrons to avoid sample damage. Furthermore, flexible aberration correction schemes are desired, preferably at low costs.

Many different approaches have been made to gain full control over electron beam properties. In this thesis, transverse electron beam control via electron-photon interaction is presented. The applications of free electron-photon interactions are found mainly in electron microscopy [34], but also in electron accelerators [35] and X-ray sources [36]. In this thesis the theoretical discussion, and naturally the experiment as well, is restricted to electron microscopy.

The theory encompasses the wave-front shaping of light (Chapter 2.1) as a means to comprehend the mechanism of wave-front shaping via phase modulation. Following this, Chapter 2.2 discusses different electron wave-front shaping mechanisms. Chapter 2.3 introduces the ponderomotive potential, which provides insight into the behavior of electrons in a light field. It is succeeded by a semi-classical description of ponderomotive interaction (Chapter 2.4). Here, electron wave packets (Chapter 2.4.1) and wave-fronts (Chapter 2.4.2) within a light field are discussed. Subsequently, Chapter 2.5 details the quantum description via Dirac equation (Chapter 2.5.1), which ultimately leads to an effective scattering phase of the electron wave function (Chapter 2.5.2) that can be used to connect to a classical description of ballistic electrons (Chapter 2.5.3). Finally, coherence (Chapter 2.6) and ponderomotive electron lenses (Chapter 2.7) are discussed in theoretical detail.

2.1. Wave-Front Shaping of Light

As discussed in Chapters 1 and 2, the discovery of the wave nature of electrons sparked the idea of substituting light with electrons for various experiments. Basic ideas regarding the manipulation of light wave functions are also valid for the manipulation of electron wave functions.

In this thesis, electron wave-front shaping via phase modulation (as detailed in Chapter 2.5) is presented. Thus, an overview of light wave-front shaping is given first, to give a basic idea of wave-front shaping in general. Furthermore, as later seen in Chapter 2.5.2, the ability to shape electron wave-fronts is directly connected to our ability to shape the wave-front of light.

The incredibly vast research field of light optics was always one of the great interests of humankind. From single lenses, used for magnifying glasses and eyeglasses, to whole systems of lenses and mirrors, used for microscopes and telescopes. The theoretical and technical advances in light optics were always important for many different branches of science like physics, astronomy, medicine, and biology.

The introduction of quantum physics meant not only immense advances in the theoretical understanding of light and its interactions with matter, but also new experimental designs. The laser, short for light amplification by stimulated emission of radiation [37], is still arguably the most important discovery in that regard. Its invention was an important milestone, as it provided a highly monochromatic, coherent, and directional source of light.

The laser is of great importance for various fields in physics like microscopy and spectroscopy. Thus, control over a laser beam is crucial for the development of many applications in these fields. Longitudinal properties of a laser beam are characteristics like pulse shape, width, frequency, and repetition rate. Spectral properties are characteristics like wavelength and linewidth. Transverse properties are characteristics like beam waist and transverse profile. All of them are initially governed by the construction and operational mode of the laser and can be changed along the beam's path through various optical elements like lenses, crystals, polarizers, and phase plates [38].

For the control of a beam's wave-front, spatial light modulators (SLM) are particularly powerful tools. They led to advances in deep-tissue imaging [39], optical quantum encryption [40], endoscopic imaging [41], laser welding [42], second harmonic imaging [43], and were important for the Nobel prize-winning technique of stimulated emission depletion microscopy [44]. Spatial light modulators are capable of imprinting a transverse phase pattern $\varphi_\perp(\mathbf{r})$ onto the light beam with initial wave function $\Phi_{in}(\mathbf{r}, t)$, with temporal and spatial coordinates t and $\mathbf{r}$. The wave function after the SLM $\Phi_f(\mathbf{r}, t)$ is given by:

$$\Phi_f(\mathbf{r}, t) = \Phi_{in}(\mathbf{r}, t)e^{i\varphi_\perp(\mathbf{r})} \tag{2.2}$$

Additionally, an SLM can also be used for amplitude modulation by reflecting part of the light beam out of the beam path. The information about the desired phase pattern is digitally delivered onto the SLM, as described later in Chapter 3.3.

2.2. Wave-Front Shaping of Electrons

After gaining an insight into light wave-front shaping, the following chapter provides a brief overview of various techniques for electron wave-front shaping.

The transverse electron beam density distribution at a certain point in space is initially governed by the electron source. It is further influenced by apertures and by the acquired phase of the electron wave function along its path. The major phase contributors on electron beams are the magneto- and electrostatic lenses as well as beam shift, tilt and astigmatism. Lenses are necessary to guide the electron beam through the column as well as control its focus to hit the specimen at a given spot. Common electron lenses modify the electron phase in a way that cannot be changed flexibly. Thus, having an additional method of imprinting an arbitrary phase is necessary for full control of the transverse electron beam shape.

So far, several techniques have been developed and proposed to get on-demand electron beam phase control, with each of them having their respective advantages and disadvantages.

Modern aberration correctors in electron lenses use different symmetries for the electromagnetic fields, which guide the electron beam through the electron microscope [45]. While already being able to achieve atomic-resolution imaging, other techniques such as structure identification [11] and optimized phase contrast microscopy [12] require better, more flexible control over the electron beam.

Electrostatic [17] and magnetostatic [16] lens arrays with tunable fields offer more flexibility. However, such lenses are often limited by achievable transmission, unwanted diffraction from subaperatures [17], charging, or beam-induced deterioration. Although the field shaping flexibility is advantageous compared to other modern aberration correctors, they still only provide a very limited degree of wave-front engineering.

Another way of transversely modulating the phase of an electron beam is achieved by using thin films of electron-transparent materials [13]. These thin films are nano-fabricated and add a phase contribution in the transverse plane proportional to the local thickness of the material. Sculpted thin films were already successfully used for the generation of Airy [46] and Bessel [47] beams. Further applications include aberration correction [14], diffractive probe engineering [48], and contrast enhancement in bio-imaging [49]. Thus, thin films provide a feasible way of arbitrary phase modulation that does not require large structures like electromagnetic electron lenses. However, a specific phase imprint always requires a specifically fabricated thin film that has to be inserted into the electron microscope. Since materials interact with the electron beam, charging, electron loss, and decoherence effects may occur.

Photon-induced near-field electron microscopy (PINEM) maps the evanescent light field in the vicinity of matter [20]. These can be used to gain attosecond coherent control of electrons [21] and can also facilitate aberration correction [50]. Thus, PINEM provides a way of transverse electron beam shaping. The evanescent field of so-called optical near-field plates is used there to imprint a transverse phase on the electron wave function. But just as other phase modulation techniques using nanostructures, charging and decoherence are challenges to be aware of.

A direct way of transverse electron wave-front shaping is possible by using electron-photon interactions to imprint a transverse phase profile onto the electron wave. This technique does not require nanostructures or tediously assembled electromagnetic lenses.

Chapter 3 describes the experimental setup that facilitates such interactions. It consists of a pulsed electron beam in an electron microscope interacting with a parallel pulsed laser beam [1], similar to a setup proposed by Konečná and García de Abajo [28]. The interaction results in a modulated electron wave function analogously to wave-front shaping in light optics in eq. 2.2.

2.3. The Ponderomotive Potential

To get a first idea of free electron-photon interactions, the classical motion of an electron within a light field is considered [51]. The light field is described by a fast oscillating electro-magnetic field. This oscillating field gives rise to an average force and, consequently, to an average potential. Thus, electron-light interactions can be described by free electrons within a potential.

Historically, in 1933, soon after the confirmation that electrons show, in fact, diffraction [3], Kapitza and Dirac [52] proposed the idea that electrons should not only diffract at crystal structures but also at standing light waves. This paved the way for an understanding of free electron-light interactions. However, this diffraction effect was too weak to be observable with the technologies of their time.

The invention of the first functioning laser [37] has led to the re-emergence of the question of observable electron-photon interactions. However, it was not until 1988 when Bucksbaum *et al.* [53] experimentally showed how a standing light wave affected the classical motion of free electrons.

The experimental realization of the diffraction of matter on a standing light wave, the nowadays called Kapitza-Dirac effect, was first achieved with atoms [54]. The diffraction of electrons at a standing light wave perpendicular to the electron beam was first observed by Freimund *et al.* [55].

The light field is mathematically described by its oscillating magnetic vector field $\vec{A}(\vec{r},t)$, which, in the rest frame of the electron, can be written as

$$\mathbf{A}(\mathbf{r},t) = -\mathbf{n}_E \frac{\mathcal{E}(\mathbf{r})}{\omega_0} \sin(\omega_0 t) \;, \tag{2.3}$$

with the normalized polarization vector $\mathbf{n}_E$, the electric field strength $\mathcal{E}(\mathbf{r})$ and the electron rest frame light field frequency ω_0.

The quantities that are usually taken to represent the light field in the Lorenz gauge are its electric $\mathbf{E}(\mathbf{r},t) = -\partial_t \mathbf{A}(\mathbf{r},t)$ and magnetic field $\mathbf{B}(\mathbf{r},t) = \nabla \times \mathbf{A}(\mathbf{r},t)$:

$$\mathbf{E}(\mathbf{r},t) = \mathbf{n}_E \mathcal{E}(\mathbf{r}) \cos(\omega_0 t) \;, \tag{2.4}$$

and

$$\mathbf{B}(\mathbf{r},t) = -\mathbf{n}_B \frac{1}{\omega_0} \frac{\mathrm{d}\mathcal{E}(\mathbf{r})}{\mathrm{d}r} \sin(\omega_0 t) \;, \tag{2.5}$$

with the magnetic field polarization vector $\mathbf{n}_B$, such that $\mathbf{n}_B \perp \mathbf{n}_E$.

An electron at rest within the light field starts moving, according to the Lorentz force $\mathbf{F}_L = e\mathbf{E}(\mathbf{r},t) = \mathrm{d}\mathbf{p}/\mathrm{d}t$, along the electric field. Here, the electron momentum $\mathbf{p} = E_e \mathbf{v}/c^2$ is chosen in a form using the relativistic electron energy E_e. Thus, it is consistent in any inertial frame.

Taking the temporal integral and rearranging the equation shows that the velocity $\mathbf{v}(\mathbf{r},t)$ is oscillating $\pi/2$ out of phase with respect to the driving electric field:

$$\mathbf{v}(\mathbf{r},t) = \mathbf{n}_E \frac{ec^2 \mathcal{E}(\mathbf{r})}{E_e \omega_0} \sin(\omega_0 t) \tag{2.6}$$

The electron acquires a velocity and therefore couples to the magnetic field. This induces an additional term to the Lorentz force via $\mathbf{F}_L(\mathbf{r},t) = e\mathbf{E}(\mathbf{r},t) + e\mathbf{v} \times \mathbf{B}(\mathbf{r},t)$.

To get the full averaged motion of the electron within the light field, consider the cycle-averaged Lorentz force. It is immediately clear that the first part of the Lorentz force, i.e. $e\mathbf{E}(\mathbf{r},t)$ averages out to zero. The second part, however, gives a non-zero cycle-averaged force in direction of the wave vector $\mathbf{n}_k$ via:

$$\langle \mathbf{F}_L(\mathbf{r},t) \rangle_t = -\mathbf{n}_k \frac{e^2 c^2}{2 E_e \omega_0^2} \mathcal{E}(\mathbf{r}) \frac{\mathrm{d}\mathcal{E}(\mathbf{r})}{\mathrm{d}r} \tag{2.7}$$

The cycle-averaged potential of this force, i.e. the ponderomotive potential $U_p(\mathbf{r})$, is found via $\langle F_L(\mathbf{r},t)\rangle_t = -\nabla U_p(\mathbf{r})$. Rearranging eq. 2.7 with $\mathcal{E}(\mathbf{r})\mathrm{d}_r\mathcal{E}(\mathbf{r}) = \mathrm{d}_r\mathcal{E}^2(\mathbf{r})/2$ and $\mathbf{n}_r\mathrm{d}_r = \nabla$ gives the ponderomotive potential:

$$U_p(\mathbf{r}) = \frac{e^2c^2\mathcal{E}^2(\mathbf{r})}{4E_e\omega_0^2} \tag{2.8}$$

The ponderomotive potential of eq. 2.8 gives an expression for a cycle-averaged potential for an electron at rest, i.e. $E_e = m_ec^2$. An approximation for the relativistic ponderomotive potential can be obtained by performing a Lorentz boost in the given direction. A simple Lorentz boost on the cycle-averaged potential, i.e. the time dependence was averaged out, is only a feasible approximation when the optical oscillation period of the light field is much shorter than the interaction time. Otherwise relativistic reversal effects occur [56]. In our experiment (Chapter 3) the interaction time is equal to the pulse length, or pulse duration, of $\Delta t = 280$fs, since the speed of light is constant in any inertial frame. This is sufficiently larger than the optical oscillation period of the laser used for the experiment (Chapter 3), i.e. $T_L = 3.5$fs. Thus, it can be assumed that no relativistic reversal takes place.

By setting the coordinate system such that the electron motion is in z-direction, the electron energy transforms via $E_e' = \gamma m_ec^2$, the light field frequency is the laboratory frame frequency ω_L. The field strength, originally written in vector form as $\mathcal{E}(\mathbf{r})\mathbf{n}_E = \mathcal{E}(\mathbf{r})$, gets transformed due to relativistic length contraction, i.e. $\mathcal{E}_z(\mathbf{r})/\gamma$. Therefore, the relativistic ponderomotive potential for an electron in the laboratory frame moving in z-direction is:

$$U_p(\mathbf{r},t) = \frac{e^2}{4m_e\gamma\omega_L^2}\left(\mathcal{E}_x^2(\mathbf{r}) + \mathcal{E}_y^2(\mathbf{r}) + \frac{\mathcal{E}_z^2(\mathbf{r})}{\gamma^2}\right) \tag{2.9}$$

Thus, for a relativistic electron, the direction of motion of the electron with respect to the light field induces a relativistic correction for the electric field strength. This ultimately makes it dependent on the polarization of the light field.

The interaction between electrons and a light field is used in various different fields to gain control over the electron beam. For instance, the characterization of electron pulses in the femtosecond domain has been achieved by ponderomotive diffraction using a light field grating [23]. Electron beam spectra can be modulated via ponderomotive forces for electron energy selection [25]. Ponderomotive generation of attosecond electron pulse trains have been realized [24]. This is accomplished by periodic energy modulation via inelastic scattering using two femtosecond laser pulses with different frequencies.

2.4. Semi-Classical Description of Ponderomotive Interaction

The following chapter compares properties of the electron wave packet, i.e. group velocity $\mathbf{v}_g$ and phase velocity $\mathbf{v}_p$, outside and within the light field. Carrying on with a semi-classical picture like in Chapter 2.3, this comparison then leads to the definition of the electron-optical refractive index n_e. The light field characterizes a potential hill, described by the ponderomotive potential.

On the one hand, the relativistic energy of an electron can be expressed as a function of its canonical momentum $\mathbf{P}$ as $E_e = \sqrt{m^2c^4 + \mathbf{P}^2c^2}$. For a free electron in an electron microscope, the canonical momentum is the free electron momentum, i.e. $\mathbf{P} = \mathbf{p}_f$. For an electron in a light field, the canonical momentum describes the free electron momentum modified by the vector potential of the light field, i.e. $\mathbf{P} = \mathbf{p}_{EM} = \mathbf{p}_f - e\mathbf{A}$ [57].

On the other hand, the relativistic energy of an electron can be expressed as a sum of the energy contributions to the electron [58]. These are the rest energy $E_0 = m_ec^2$, the acceleration energy $E_{acc} = eU$ with the acceleration voltage U, and, when applicable, the ponderomotive potential U_p. The ponderomotive potential, as seen in eq. 2.9 from the derivation in Chapter 2.3, is strictly positive and therefore describes a potential hill.

To get an estimation of the semi-classical parameters presented in this chapter, the magnitude of U_p is estimated first. The electron rest energy is $E_0 = 511keV$, and the electron acceleration energy is $E_{acc} = 30keV$, as discussed in Chapter 3.2. The expression for the ponderomotive potential from eq. 2.9 is rearranged using the intensity $I(\mathbf{r}) = c\epsilon_0\mathcal{E}^2(\mathbf{r})/2$, the relativistic free electron energy $E_e = \gamma m_ec^2 = E_0 + E_{acc} = E_f$ and the fine structure constant $\alpha = e^2/(2\epsilon_0 hc)$. Furthermore, the spatial dependency of the intensity is omitted assuming constant intensity. $I(\mathbf{r}) = I$. The value for the ponderomotive potential is calculated to:

$$U_p = \frac{\alpha hc^2 I}{E_f \omega_L^2} \tag{2.10}$$

The intensity is obtained by dividing the laser pulse energy by the pulse duration and the interaction area. The maximum value for the pulse energy in the interaction region is $E_L = 17.2\mu J$ and the minimal focus spot area is about $12.6\mu m^2$ (see Chapter 3.1). This leads, with a pulse duration of $\Delta t = 280fs$, to an intensity of about $I = 5000kW/\mu m^2$. With this intensity, eq. 2.10 gives a ponderomotive potential of $U_p = 46.2eV$. This is much smaller than the electron rest energy and the acceleration energy, but much higher than the electron acceleration energy spread $\Delta E_{acc} = 0.5$ [59]. Thus, the influence of the ponderomotive potential is not negligible.

The free and interacting electron energies, i.e. E_f and E_{EM}, are approximately the same and are calculated via

$$E_f = \sqrt{m_e^2c^4 + p_f^2c^2} = E_0 + E_{acc} \tag{2.11}$$

and

$$E_{EM} = \sqrt{m_e^2c^4 + p_{EM}^2c^2} = E_0 + E_{acc} - U_p, \tag{2.12}$$

whereas the notation $|\mathbf{p}| = p$ is used. This notation will be used throughout the following chapter since only the magnitudes of the velocities will be important in this discussion. Plugging in the energy values in eq. 2.11 and 2.12 gives an energy difference of $E_f - E_{EM} = 2.9$eV.

Using the right-hand side and middle of eq. 2.11 and 2.12 respectively, the canonical momenta can be expressed in terms of energies via

$$p_f = \frac{1}{c}\sqrt{2E_{acc}E_0 + E_{acc}^2} \tag{2.13}$$

and

$$p_{EM} = \frac{1}{c}\sqrt{2(E_{acc} - U_p)E_0 + (E_{acc} - U_p)^2}\ . \tag{2.14}$$

Plugging energy values into eq. 2.13 and 2.14 gives a momentum difference of $p_f - p_{EM} =$ 8.8eV/c.

2.4.1. Electron Wave Packet within a Light Field

In quantum mechanics, an electron propagating through an electron microscope can be described by a wave packet. The velocity of the wave packet is called the group velocity. As such, the group velocity is the velocity of the wave packet envelope. The group velocity is defined as [60]:

$$v_g = \frac{\partial E}{\partial p} = \frac{pc^2}{E} \tag{2.15}$$

Using the energies in eq. 2.11 and 2.12 and the momenta in eq. 2.13 and 2.14, the group velocities for the free and interacting cases are

$$v_{g,f} = c\sqrt{\frac{E_{acc}^2 + 2E_{acc}E_0}{E_{acc}^2 + 2E_{acc}E_0 + E_0^2}} \tag{2.16}$$

and

$$v_{g,EM} = c\sqrt{\frac{E_{acc}^2 + 2E_{acc}E_0 - U_p(2(E_0 + E_{acc}) - U_p))}{E_{acc}^2 + 2E_{acc}E_0 + E_0^2 - U_p(2(E_0 + E_{acc}) - U_p))}}\ . \tag{2.17}$$

To compare the two group velocities $v_{g,f}$ and $v_{g,EM}$, it is convenient to use the substitutions $A = E_{acc}^2 + 2E_{acc}E_0$, $B = E_0^2$ and $C = U_p(2(E_0 + E_{acc}) - U_p))$, such that $v_{g,f} = c\sqrt{A/(B + C)}$ and $v_{g,EM} = c\sqrt{(A - C)/(A + B - C)}$. Since the numerator is the magnitude of the canonical momentum $\mathbf{P} = \sqrt{A - C}$ it follows that $C < A$ for real momenta. The experimental reality is already considered in this assumption, i.e. it was shown that the ponderomotive potential is much smaller than the free electron energy. Otherwise, reflection and tunneling effects would occur.

Using the substitutions, it can be deduced that if $-BC < 0$, the free electron wave packet group velocity is higher than the group velocity within the light field:

$$v_{g,EM} < v_{g,f} \tag{2.18}$$

Since B and C are per definition always positive definite, inequality 2.18 holds. Plugging energy values into eq. 2.16 and 2.17 gives a ratio of $v_{g,EM}/v_{g,f} = 1 - 7 \times 10^{-4}$. The electron wave packet gets slowed down by the light field, and the stronger the light field, the slower the group velocity of the electrons. The temporal retardation, assuming an interaction duration of 280fs, amounts to 12as. It follows that, if the intensity is not constant within the plane of incident, i.e. $I = I(x, y)$, pulse broadening of the electron beam occurs.

2.4.2. Electron Wave-Fronts within a Light Field

In contrast to the group velocity, the phase velocity is the propagation velocity of the phase of a wave within the wave packet. The phase velocity of a wave is defined as [60]:

$$v_p = \frac{E}{p} \tag{2.19}$$

From eq. 2.15 follows that

$$v_{p,f} = \frac{c^2}{v_{g,f}} \tag{2.20}$$

and

$$v_{p,EM} = \frac{c^2}{v_{g,EM}} \ . \tag{2.21}$$

This means, that the phase velocity of an electron wave packet within a light field is higher than the phase velocity of a freely propagating electron wave packet, i.e.

$$v_{p,EM} > v_{p,f} \ . \tag{2.22}$$

The phase velocities $v_{p,f}$ and $v_{p,f}$ are superluminar, as typical for matter waves. Their ratio is $v_{p,EM}/v_{p,f} = 1 + 7 \times 10^{-4}$.

Thus, the higher the ponderomotive potential at a given point in the transverse plane, the higher the phase velocity of the wave at this point. This leads to the conclusion that a light field intensity distribution similar to a quadratic function will curve the phase velocity similarly to convex lenses for light optics. Additionally, a light field intensity distribution similar to a negative quadratic function will curve the phase velocity similarly to concave lenses for light optics. Both cases are sketched in fig. 2.1.

The ratio between the phase velocities is, in light optics, often used to calculate the dimensionless refractive index. In electron optics, however, the definition of the electron-optical refractive index n_e with regard to the phase velocities has to be slightly corrected due to the mass of the electron and consequential relativistic effects. Thus, the relativistic electron-optical index is defined over the wave vectors and, as such, over the wavelengths of the electron wave packet [58]:

$$n_e = \frac{\lambda_f}{\lambda_{EM}} = \frac{p_{EM}}{p_f} = \frac{v_{p,f}}{v_{p,EM}} \frac{E_{EM}}{E_f} = \sqrt{\frac{2(E_{acc} - U_p)E_0 + (E_{acc} - U_p)^2}{2E_{acc}E_0 + (E_{acc})^2}} \tag{2.23}$$

Since the ponderomotive potential is positive, the numerator of eq.2.23 is smaller than the denominator. Thus, contrary to most materials in electron and light optics, the electron-optical refractive index for electrons propagating through a light field is smaller than unity. This is seen by plugging the energy values into eq. 2.24, which gives $n_e = 0.9999503$.

Furthermore, coming back to the original case of spatially varying intensity, i.e. $I = I(x, y)$, the electron-optical refractive index is spatially varying with the varying intensity of the light field:

$$n(I) = n(x, y) < 1 \tag{2.24}$$

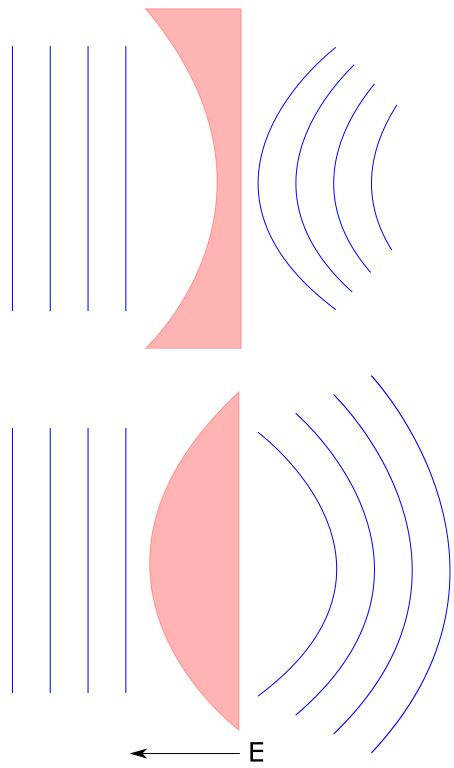

Figure 2.1.: Sketch of the wave curvatures of electron waves (blue) after traversing a parallel-propagating light field (red). The thickness of the light field is proportional to the energy density of the light pulse and, therefore, to the intensity. Thus, the upper case of a quadratic intensity distribution leads to converging wave-fronts, while the lower case leads to diverging wave-fronts.

Equation 2.24 shows that control over the intensity of a parallel-propagating light wave-front enables electron wave-front shaping.

2.5. Quantum Description of Ponderomotive Interaction

Electrons and photons are fundamental particles. Thus, a quantum description is necessary to describe their interaction.

Due to their fermionic nature, the equation of motion applicable for electrons is the Dirac equation [61]. The Dirac equation is a wave equation that considers both special relativity and quantum mechanics and, for free electrons, reads as:

$$[m_e c^2 \beta_4 + c\vec{\alpha}\mathbf{p}]\Psi(\mathbf{r},t) = i\hbar\partial_t\Psi(\mathbf{r},t) \tag{2.25}$$

Here, $\Psi(\mathbf{r},t)$ is the 4-component spinor electron wave function dependent on spatial coordinates $\mathbf{r} = (x, y, z)$ and time t. Furthermore, $\mathbf{p} = -i\hbar\nabla$ is the electron momentum operator in configuration space, and $\hbar$, c and m_e are the reduced Planck constant, the speed of light, and the electron mass respectively, while β_4 and $\vec{\alpha}$ are Dirac matrices of the form

$$\beta_4 = \begin{pmatrix} \mathcal{I}_2 & 0 \\ 0 & -\mathcal{I}_2 \end{pmatrix}, \quad \vec{\alpha} = \begin{pmatrix} 0 & \vec{\sigma} \\ \vec{\sigma} & 0 \end{pmatrix} , \tag{2.26}$$

where $\mathcal{I}_2$ is a 2×2 identity matrix and $\vec{\sigma}$ are the three Pauli matrices.

For the interaction with photons, the Dirac equation has to be modified using an interaction Hamiltonian that couples the electrons and the light field.

2.5.1. The Effective Schrödinger Equation

For electron-photon interactions, a photon is mathematically described by a real vector field $\mathbf{A}(\mathbf{r},t)$ and scalar field $\Phi_s(\mathbf{r},t)$. The Dirac equation (eq. 2.31) is then modified by the electron-photon coupling via the electromagnetic coupling constant, i.e. the elementary charge e:

$$[m_e c^2 \beta + c\vec{\alpha}\mathbf{p} + ce\vec{\alpha}\mathbf{A}(\mathbf{r},t) - e\Phi_s(\mathbf{r},t)]\Psi(\mathbf{r},t) = i\hbar\partial_t\Psi(\mathbf{r},t) \tag{2.27}$$

Following [28], the 4-component spinor $\Psi(\mathbf{r},t)$ can be expressed in terms of a complete basis set of plane wave solutions with spinor amplitudes $\Psi^{\pm}_{\mathbf{k},j}$, where $\mathbf{k}$ denotes the wave vector of that spinor, j the spin states and the upper sign $\pm$ denotes electron and positron solutions respectively, i.e. positive and negative energy solutions, such that

$$\Psi(\mathbf{r},t) = \frac{1}{V}\sum_{\pm}\sum_{j}\sum_{\mathbf{k}} \phi^{\pm}_{\mathbf{k},j} e^{i(\mathbf{kr} \mp E_k t/\hbar)}\Psi^{\pm}_{\mathbf{k},j} , \tag{2.28}$$

with the quantization volume V, the electron energies corresponding to the wave vectors E_k and the expansion coefficients $\phi^{\pm}_{\mathbf{k},j}$. The negative energy solutions for positrons are depicted as $-E_k$, taking care of the sign outside of the positive definite energy value in this definition.

The 4-component spinor amplitudes $\Psi^{\pm}_{\mathbf{k},j}$ introduced in eq. 2.28 are the eigenstates of the unperturbed eigenvalue equation

$$(m_e c^2 \beta_4 + c\hbar\vec{\alpha}\mathbf{k})\Psi^{\pm}_{\mathbf{k},j} = \pm E_k \Psi^{\pm}_{\mathbf{k},j} \ , \tag{2.29}$$

with the momentum expressed by the wave vector $\mathbf{k}$ via $\mathbf{p} = \hbar\mathbf{k}$.

Requiring normalization, it is shown in appendix A.2 that these eigenstates can be written as:

$$\Psi^{+}_{\mathbf{k},j} = \sqrt{\frac{E_k + m_e c^2}{2E_k}} \begin{pmatrix} \hat{\mathbf{s}}_j \\ \frac{\hbar c(\mathbf{k}\vec{\sigma})}{E_k + m_e c^2}\hat{\mathbf{s}}_j \end{pmatrix}, \quad \Psi^{-}_{\mathbf{k},j} = \sqrt{\frac{E_k + m_e c^2}{2E_k}} \begin{pmatrix} -\frac{\hbar c(\mathbf{k}\vec{\sigma})}{E_k + m_e c^2}\hat{\mathbf{s}}_j \\ \hat{\mathbf{s}}_j \end{pmatrix} \tag{2.30}$$

Here, the $\hat{\mathbf{s}}_j$ are orthonormal 2-component spinors, which represent the two electron spin states (j=1/2,-1/2). A suitable orthonormal basis for $\hat{\mathbf{s}}_j$, regarding the complex inner product, is $\hat{\mathbf{s}}_{1/2} = (1, 0)$ and $\hat{\mathbf{s}}_{-1/2} = (0, 1)$.

Since the 4-component spinor amplitudes of eq. 2.30 within the plane wave expansion of eq. 2.28 represent solutions to the unperturbed Dirac equation 2.29, the first two terms in eq. 2.27 can be substituted with $\pm E_k$, as shown in appendix A.2, such that:

$$\left[\frac{1}{V}\sum_{\mathbf{k},j,\pm} \phi^{\pm}_{\mathbf{k},j}(\pm E_k)e^{i(\mathbf{kr}\mp E_k t/\hbar)}\Psi^{\pm}_{\mathbf{k},j}\right] + [ce\vec{\alpha}\mathbf{A}(\mathbf{r},t) - e\Phi_s(\mathbf{r},t)]\Psi(\mathbf{r},t) = i\hbar\partial_t\Psi(\mathbf{r},t) \tag{2.31}$$

To simplify this equation, the first assumption is made that all wave vectors $\mathbf{k}$ are tightly packed around a central wave vector $\mathbf{k}_0$, i.e. $|\mathbf{k}_0 - \mathbf{k}| \ll k_0$, which is well satisfied within an electron microscope [28]. Furthermore, a non-recoil approximation is considered, implying that after the interaction with the light field, the electron beam still satisfies the central wave vector approximation. Hence, the non-recoil approximation insinuates that there is only a negligible amount of momentum exchange between photons and electrons.

Within these assumptions, the energies $E_{\mathbf{k}}$ can be Taylor expanded around $\mathbf{k}_0$, with $E_{\mathbf{k}_0} \equiv E_0$, such that

$$E_k \approx E_0 + \hbar\mathbf{v}(\mathbf{k} - \mathbf{k}_0) \ , \tag{2.32}$$

where the central electron beam velocity $\mathbf{v}$ is recognised as $\mathbf{v} = \hbar c^2\mathbf{k}_0/E_0$ by considering $\mathbf{p}_0 = \hbar\mathbf{k}_0 = \gamma m_e\mathbf{v}$ and $E_0 = \gamma m_e c^2 = \sqrt{p_0^2c^2 + m_e^2c^4}$. To use eq. 2.32 later on in configuration space, it is necessary to recognize the momentum operator represented by $\mathbf{k} = -i\nabla$, such that

$$E_k \approx E_0 - \hbar\mathbf{v}(i\nabla + \mathbf{k}_0) \ , \tag{2.33}$$

within the sum over the wave vectors.

Due to the central wave vector approximation, the spinor amplitudes $\Psi^{\pm}_{\mathbf{k},j}$ in eq. 2.30 are set to the central wave vector spinor amplitude $\Psi^{\pm}_{\mathbf{k}_0,j}$. This leads to a more compact expression for the 4-component electron wave function via

$$\Psi(\mathbf{r},t) = \frac{1}{V}\sum_{\mathbf{k},j,\pm} \phi^{\pm}_{\mathbf{k},j}e^{i(\mathbf{kr}\mp E_k t/\hbar)}\Psi^{\pm}_{\mathbf{k},j} \approx \sum_{j,\pm}\psi^{\pm}_j(\mathbf{r},t)\Psi^{\pm}_{\mathbf{k}_0,j} \ , \tag{2.34}$$

where $\psi_j^{\pm}(\mathbf{r},t)$ are scalar wave-functions, which consist per definition of the quantization volume, the expansion coefficients and the plane wave exponential functions within the sum over all wave vectors.

Plugging eq. 2.33 and 2.34 into eq. 2.31 leads to:

$$\sum_{j,\pm}[\pm E_0 \mp \hbar\mathbf{v}(i\nabla + \mathbf{k}_0) + ce\vec{\alpha}\mathbf{A}(\mathbf{r},t) - e\Phi_s(\mathbf{r},t)]\psi_j^{\pm}(\mathbf{r},t)\Psi_{\mathbf{k}_0 j}^{\pm} = i\hbar\partial_t \sum_{j,\pm}\psi_j^{\pm}(\mathbf{r},t)\Psi_{\mathbf{k}_0 j}^{\pm} \tag{2.35}$$

Equation 2.35 is now multiplied from the left with $(\Psi_{\mathbf{k}_0 l}^{+})^{\dagger}$ and $(\Psi_{\mathbf{k}_0 l}^{-})^{\dagger}$, leading to two equations. Since no spin-coupling effects are expected, it is advantageous to reduce the four-dimensional equation to two scalar equations, which will carry the electron and positron scalar functions. Thus, the multiplications of electron and positron conjugate transpose spinors are the most straight-forward choices to get equations for the scalar functions. Therefore, it is convenient to first derive the following identities, which are proven in appendix A.3:

$$[\Psi_{\mathbf{k}_0 l}^{\pm}]^{\dagger}\Psi_{\mathbf{k}_0 j}^{\pm} = \delta_{lj} \tag{2.36}$$

$$[\Psi_{\mathbf{k}_0 l}^{\mp}]^{\dagger}\Psi_{\mathbf{k}_0 j}^{\pm} = 0 \tag{2.37}$$

$$[\Psi_{\mathbf{k}_0 l}^{\pm}]^{\dagger}\vec{\alpha}\Psi_{\mathbf{k}_0 j}^{\pm} = \pm\frac{\mathbf{v}}{c}\delta_{lj} \tag{2.38}$$

$$[\Psi_{\mathbf{k}_0 l}^{\mp}]^{\dagger}\vec{\alpha}\Psi_{\mathbf{k}_0 j}^{\pm} = \hat{\mathbf{s}}_l^{\dagger}[\vec{\sigma} - (1-1/\gamma)\hat{\mathbf{v}}(\hat{\mathbf{v}}\vec{\sigma})]\hat{\mathbf{s}}_j =: \mathbf{b}_{lj} \tag{2.39}$$

Here, $\gamma = 1/\sqrt{1-(v/c)^2}$ is the relativistic Gamma factor and $\hat{\mathbf{v}} = \mathbf{v}/v$ is a unit vector pointing in direction of the electron velocity.

The two resulting equations read as

$$[E_0 - \hbar\mathbf{v}(i\nabla + \mathbf{k}_0) + e\mathbf{v}\mathbf{A}(\mathbf{r},t) - e\Phi_s(\mathbf{r},t)]\psi_l^{+}(\mathbf{r},t) + e\sum_j \mathbf{b}_{lj}\mathbf{A}(\mathbf{r},t)\psi_j^{-}(\mathbf{r},t) = i\hbar\partial_t\psi_l^{+}\ , \tag{2.40}$$

and

$$-[E_0 - \hbar\mathbf{v}(i\nabla + \mathbf{k}_0) + e\mathbf{v}\mathbf{A}(\mathbf{r},t) + e\Phi_s(\mathbf{r},t)]\psi_l^{-}(\mathbf{r},t) + e\sum_j \mathbf{b}_{lj}\mathbf{A}(\mathbf{r},t)\psi_j^{+}(\mathbf{r},t) = i\hbar\partial_t\psi_l^{-}\ . \tag{2.41}$$

Using the central wave vector approximation again, the scalar electron wave function $\psi_j^{\pm}(\mathbf{r},t)$ from eq. 2.34 can be rewritten in terms of a central plane wave with slowly varying amplitudes $\phi_j^{\pm}(\mathbf{r},t)$:

$$\psi_j^{\pm}(\mathbf{r},t) = e^{i(\mathbf{k}_0\mathbf{r}\mp E_0 t/\hbar)}\phi_j^{\pm}(\mathbf{r},t) \tag{2.42}$$

Plugging eq. 2.42 into eq. 2.40 and 2.41 and differentiating by parts via

$$\nabla\psi_j^{\pm}(\mathbf{r},t) = i\mathbf{k}_0 e^{i(\mathbf{k}_0\mathbf{r}\mp E_0 t/\hbar)}\phi_j^{\pm}(\mathbf{r},t) + e^{i(\mathbf{k}_0\mathbf{r}\mp E_0 t/\hbar)}\nabla\phi_j^{\pm}(\mathbf{r},t) \tag{2.43}$$

and

$$\partial_t \psi_j^{\pm}(\mathbf{r},t) = \mp \frac{iE_0}{\hbar} e^{i(\mathbf{k}_0\mathbf{r} \mp E_0 t/\hbar)} \phi_j^{\pm}(\mathbf{r},t) + e^{i(\mathbf{k}_0\mathbf{r} \mp E_0 t/\hbar)} \partial_t \phi_j^{\pm}(\mathbf{r},t) \ , \tag{2.44}$$

while multiplying the equations by $e^{-i(\mathbf{k}_0\mathbf{r} \mp E_0 t/\hbar)}$, eq. 2.40 and 2.41 reduce to

$$[-i\hbar(\mathbf{v}\nabla + \partial_t) + e\mathbf{v}\mathbf{A}(\mathbf{r},t) - e\Phi_s(\mathbf{r},t)]\phi_l^{+}(\mathbf{r},t) + e\sum_j \mathbf{b}_{lj}\mathbf{A}(\mathbf{r},t)\phi_j^{-}(\mathbf{r},t)e^{2iE_0t/\hbar} = 0 \tag{2.45}$$

and

$$[i\hbar(\mathbf{v}\nabla - \partial_t) + e\mathbf{v}\mathbf{A}(\mathbf{r},t) + e\Phi_s(\mathbf{r},t)]\phi_l^{-}(\mathbf{r},t) + e\sum_j \mathbf{b}_{lj}\mathbf{A}(\mathbf{r},t)\phi_j^{+}(\mathbf{r},t)e^{-2iE_0t/\hbar} = 0 \ . \tag{2.46}$$

For an electron beam within an electron microscope, the only mechanism to generate positrons is pair production. Since acceleration energy in electron microscopes is well below the positron rest energy, the effect of positrons and their spatial variation is very weak compared to the electrons [28]. Therefore, all terms regarding $\phi_l^{-}(\mathbf{r},t)$ and $\nabla\phi_l^{-}(\mathbf{r},t)$ are considered zero compared to the electron part $\phi_l^{+}(\mathbf{r},t)$ in eq. 2.46. The temporal variation is not neglected due to the fast oscillation of possible positrons. Doing this leaves a differential equation for the slowly varying amplitude of the positron:

$$-i\hbar\partial_t\phi_l^{-}(\mathbf{r},t) + \sum_j \mathbf{b}_{lj}\mathbf{A}(\mathbf{r},t)\phi_j^{+}(\mathbf{r},t)e^{-2iE_0t/\hbar} = 0 \tag{2.47}$$

In the second term of eq. 2.47 the time variation is dominated by the plane wave exponential factor, since the electrons have an oscillation period of $\sim 10^{-20}$s for an acceleration energy of $E_{acc} = 30$keV, such that $E_0 = m_e c^2 + E_{acc}$, while the photons described by $\mathbf{A}(\mathbf{r},t)$ have an oscillation period of $\sim 10^{-15}$s and $\phi(\mathbf{r},t)$ is a slowly varying amplitude in time. Thus, the slowly varying amplitude for the positron wave function can be expressed in leading order as:

$$\phi_l^{-}(\mathbf{r},t) \approx \frac{e}{2E_0}\sum_j \mathbf{b}_{lj}\mathbf{A}(\mathbf{r},t)\phi_j^{+}(\mathbf{r},t)e^{-2iE_0t/\hbar} \tag{2.48}$$

Inserting this expression into eq. 2.45 gives an equation for the slowly varying amplitude $\phi_j^{+}(\mathbf{r},t)$ for electrons:

$$i\hbar(\mathbf{v}\nabla + \partial_t)\phi_j^{+}(\mathbf{r},t) = (e\mathbf{v}\mathbf{A}(\mathbf{r},t) - e\Phi_S(\mathbf{r},t))\phi_j^{+}(\mathbf{r},t) + \frac{e^2}{2E_0}\sum_{jj'} \mathbf{b}_{lj}\mathbf{A}(\mathbf{r},t)\mathbf{b}_{jj'}\mathbf{A}(\mathbf{r},t)\phi_{j'}^{+}(\mathbf{r},t) \tag{2.49}$$

Since the coordinate system can be set arbitrarily, the direction of the velocity $\mathbf{v}$ is, for simplicity, set to a main axis, here $\hat{\mathbf{v}} = \hat{\mathbf{z}}$. Furthermore, it is shown in appendix A.3, that the following relation holds:

$$\sum_j (\mathbf{A}(\mathbf{r},t)\mathbf{b}_{lj})(\mathbf{b}_{jj'}\mathbf{A}(\mathbf{r},t)) = \delta_{lj'}\left(A_x^2(\mathbf{r},t) + A_y^2(\mathbf{r},t) + \frac{1}{\gamma^2}A_z^2(\mathbf{r},t)\right) \tag{2.50}$$

Using this relation for eq. 2.49, the Delta-Distribution $\delta_{lj'}$ gets rid of the sum over all spin states, showing that the solution for 2.49 is spin state independent, hence the spin index can be omitted. Furthermore, due to the experimental setup, the positron solution is negligible compared to the electron solution of the wave function, i.e. $|\phi^-/\phi^+| \approx ceA/E_0$, and only the electron solutions $\phi^+ \equiv \phi$ will be considered.

Consequently, eq. 2.49 can be rewritten as:

$$i\hbar(\mathbf{v}\nabla+\partial_t)\phi(\mathbf{r},t) = (e\mathbf{v}\mathbf{A}(\mathbf{r},t)-e\Phi_S(\mathbf{r},t)+\frac{e^2}{2m_e\gamma}\left(A_x^2(\mathbf{r},t)+A_y^2(\mathbf{r},t)+\frac{1}{\gamma^2}A_z^2(\mathbf{r},t)\right)\phi(\mathbf{r},t) \tag{2.51}$$

This equation can be seen as an effective Schrödinger equation with the interaction Hamiltonian $U(\mathbf{r},t)$:

$$U(\mathbf{r},t) = e\mathbf{v}\mathbf{A}(\mathbf{r},t) - e\Phi_S(\mathbf{r},t) + \frac{e^2}{2m_e\gamma}\left(A_x^2(\mathbf{r},t)+A_y^2(\mathbf{r},t)+\frac{1}{\gamma^2}A_z^2(\mathbf{r},t)\right) , \tag{2.52}$$

The cycle-averaged second order interaction Hamiltonian, i.e. the quadratic terms in eq. 2.52, is consistent with the relativistically corrected ponderomotive potential in eq. 2.9.

2.5.2. The Effective Scattering Phase

The effective Schrödinger equation for the slowly varying amplitude $\phi(\mathbf{r},t)$ can be seen as the transverse electron beam profile. Therefore, the scalar wave function is renamed via $\phi(\mathbf{r},t) \equiv \phi_\perp(\mathbf{r},t)$ to highlight this. A more concise way of writing eq. 2.51 using eq. 2.52 gives:

$$(\partial_t + \mathbf{v}\nabla)\phi_\perp(\mathbf{r},t) = -\frac{i}{\hbar}U(\mathbf{r},t)\phi_\perp(\mathbf{r},t) \tag{2.53}$$

The general solution for this equation shows the evolution of the state $\Psi_\perp$ between two times, with an initial time t_0 and a final time t, where $t > t_0$. The final state can generally be written as:

$$\phi_\perp(\mathbf{r},t) = \phi_\perp(\mathbf{r}-\mathbf{v}t+\mathbf{v}t_0)\exp\left[-\frac{i}{\hbar}\int_{t_0}^{t} U(\mathbf{r}-\mathbf{v}t+\mathbf{v}\tau,\tau)\mathrm{d}\tau\right] \tag{2.54}$$

The first part of the right-hand-side of eq. 2.54 describes the free propagation of the system. The second part can be seen as an additional phase $\varphi(\mathbf{r},t) = -\int U(\mathbf{r}-\mathbf{v}t+\mathbf{v}\tau,\tau)\mathrm{d}\tau/\hbar$, acquired over the course of the interaction between t_0 and t.

As seen by the fact that $\mathbf{v} = v\hat{\mathbf{z}}$, the z and t coordinates are coupled by the velocity. Thus, the retarded coordinate $\mathbf{r}-\mathbf{v}t$ can be used, which characterizes the movement of the wave-front. The terms $+\mathbf{v}t_0$ and $+\mathbf{v}\tau$ characterize the initial translation of the wave and the translation to the interaction region.

To check for the validity of the general solution, eq. 2.54 is plugged into eq. 2.53.

The time derivative of the wave function 2.54 is

$$\begin{aligned}
&\partial_t \phi_\perp(\mathbf{r}, t) \\
&= e^{i\varphi(\mathbf{r},t)}(\partial_t \phi_\perp(\mathbf{r} - \mathbf{v}t + \mathbf{v}t_0)) - \frac{i}{\hbar}\phi_\perp(\mathbf{r}, t)\left(\partial_t \int_{t_0}^{t} U(\mathbf{r} - \mathbf{v}t + \mathbf{v}\tau, \tau)\mathrm{d}\tau\right) \\
&= -e^{i\varphi(\mathbf{r},t)}\mathbf{v}(\nabla\phi_\perp(\mathbf{r} - \mathbf{v}t + \mathbf{v}t_0)) - \frac{i}{\hbar}\phi_\perp(\mathbf{r}, t)\partial_t\left(\mathcal{U}(\mathbf{r} - \mathbf{v}t + \mathbf{v}t, t) - \mathcal{U}(\mathbf{r} - \mathbf{v}t + \mathbf{v}t_0, t_0)\right) \\
&= -e^{i\varphi(\mathbf{r},t)}\mathbf{v}(\nabla\phi_\perp(\mathbf{r} - \mathbf{v}t + \mathbf{v}t_0)) - \frac{i}{\hbar}\phi_\perp(\mathbf{r}, t)U(\mathbf{r}, t) - \frac{i}{\hbar}\phi_\perp(\mathbf{r}, t)\mathbf{v}\nabla\mathcal{U}(\mathbf{r} - \mathbf{v}t + \mathbf{v}t_0, t_0)\ ,
\end{aligned}$$

whereas $\mathcal{U}$ is the primitive function of U.

The spatial derivative, together with the velocity, of eq. 2.54 is:

$$\begin{aligned}
&\mathbf{v}\nabla\phi_\perp(\mathbf{r}, t) \\
&= e^{i\varphi(\mathbf{r},t)}\mathbf{v}\nabla\phi_\perp(\mathbf{r} - \mathbf{v}t + \mathbf{v}t_0) - \frac{i}{\hbar}\phi_\perp(\mathbf{r}, t)\mathbf{v}\nabla\mathcal{U}(\mathbf{r}, t) + \frac{i}{\hbar}\phi_\perp(\mathbf{r}, t)\mathbf{v}\nabla\mathcal{U}(\mathbf{r} - \mathbf{v}t + \mathbf{v}t_0, t_0)
\end{aligned}$$

Adding these two derivatives to get the left-hand-side of eq. 2.53, leads to:

$$(\partial_t + \mathbf{v}\nabla)\phi_\perp(\mathbf{r}, t) = -\frac{i}{\hbar}\phi_\perp(\mathbf{r}, t)\left(U(\mathbf{r}, t) - \mathbf{v}\nabla\mathcal{U}(\mathbf{r}, t)\right) \tag{2.55}$$

The electron-photon interaction only takes place in the interaction region. Therefore, if only the electron state before and after the interaction is taken into consideration, the interaction can be seen as a scattering event in a fixed interaction plane, which is perpendicular to the z-axis.

Thus, U is taken to be constant in z and consequently its primitive function as well, leading to $\partial_z\mathcal{U}(\mathbf{r}, t) \approx 0$. This is also consistent with the fact, that $\Psi_\perp$ is the slowly varying amplitude to the whole wave function. With the direction of motion in z-direction, the product $\mathbf{v}\nabla\mathcal{U}(\mathbf{r}, t)$ is zero.

Moreover, the treatment of the interaction as a scattering event allows one to expand the integral to infinity, i.e. $[t_0, t] \to (-\infty, \infty)$. This leads to the loss of the explicit time dependence of the phase, i.e. $\varphi(\mathbf{r}, t) = \varphi(\mathbf{r})$.

Therefore, eq. 2.54 is a solution to the effective Schrödinger equation 2.53 and can be written as

$$\phi_\perp(\mathbf{r}, t) = \phi_\perp(\mathbf{r} - \mathbf{v}t + \mathbf{v}t_0)e^{i\varphi(\mathbf{r})}\ , \tag{2.56}$$

with the scattering phase

$$\varphi(\mathbf{r}) = -\frac{1}{\hbar}\int_{-\infty}^{\infty} U(\mathbf{r} - \mathbf{v}t + \mathbf{v}\tau, \tau)\mathrm{d}\tau\ . \tag{2.57}$$

Note that the framework of wave-front shaping within the assumptions (eq. 2.56), is similar to the principle of wave-front shaping of light (eq. 2.2) with a spatial light modulator.

To describe the electron wave function after the electron-photon scattering process, the ponderomotive potential from eq. 2.52 has to be inserted in eq. 2.57. The first two terms in the interaction Hamiltonian in eq. 2.52 show a first-order interaction Hamiltonian $U^{(1)}$, which describes the interaction between one electron and one photon. The second term, a second-order interaction effect $U^{(2)}$, describes a one-electron-two-photon interaction.

Separating these two parts for now and taking the gauge freedom of the system into account, which enables one to set the scalar potential to zero, i.e. $\Phi_S(\mathbf{r}, t) = 0$, the effective scattering phase for the first order interaction reads as:

$$\varphi^{(1)}(\mathbf{r}, t) = \int_{-\infty}^{\infty} \mathrm{d}\tau U^{(1)}(\mathbf{r} - \mathbf{v}t + \mathbf{v}\tau, \tau) = e \int_{-\infty}^{\infty} \mathrm{d}\tau \mathbf{v}\mathbf{A}(\mathbf{r} - \mathbf{v}\mathbf{t} + \mathbf{v}\tau, \tau) \tag{2.58}$$

In general, the electric field at every point can be expressed as a superposition of plane waves via

$$\mathbf{E}(\mathbf{r}, t) = \sum_{\mathbf{k}_L, \sigma} C_{\mathbf{k}_L, \sigma} \hat{\mathbf{e}}_{\mathbf{k}_L, \sigma} e^{i(\mathbf{k}_L \mathbf{r} - \omega_L t)} \ , \tag{2.59}$$

where $\mathbf{k}_L$ are wave vectors of the light field, ω_L is the light field frequency, σ is the polarization, $C_{\mathbf{k}_L, \sigma}$ are weighting coefficients and $\hat{\mathbf{e}}_{\mathbf{k}_L, \sigma}$ are polarization vectors.

With the relationship between vector potential and electric field $\mathbf{E}(\mathbf{r}, t) = -\partial t \mathbf{A}(\mathbf{r}, t)$, one can deduce that

$$\int_{-\infty}^{\infty} \mathrm{d}\tau \mathbf{v}\mathbf{A}(\mathbf{r} - \mathbf{v}\mathbf{t} + \mathbf{v}\tau, \tau) \propto \int_{-\infty}^{\infty} \mathrm{d}\tau e^{i(\mathbf{k}_L(\mathbf{r} - \mathbf{v}t + \mathbf{v}\tau) - \omega_L \tau)} \ , \tag{2.60}$$

and since the velocity v of the electrons points in positive z-direction, the integral to solve is:

$$\int_{-\infty}^{\infty} \mathrm{d}\tau e^{i(\mathbf{k}_L(\mathbf{r} - \mathbf{v}t + \mathbf{v}\tau) - \omega_L \tau)} \propto \int_{-\infty}^{\infty} \mathrm{d}\tau e^{i\tau(k_z v - \omega_L)} \tag{2.61}$$

Comparing the integral in eq. 2.61 to the definition of the Dirac-Delta distribution via the Fourier transform, the integral reduces to

$$\int_{-\infty}^{\infty} \mathrm{d}\tau e^{i\tau(k_z v - \omega_L)} = \delta(k_z v - \omega_L) \tag{2.62}$$

For free electrons, this Dirac-Delta distribution is always zero, since

$$k_z v \leq k v = \frac{\omega_L v}{c} < \omega_L \ , \tag{2.63}$$

because the electron speed is always smaller than the speed of light.

Thus, in the non-recoil approximation, there is no first-order interaction between free propagating electrons and photons [28], i.e. $\varphi^{(1)} = 0$, and the effective scattering phase reduces to :

$$\varphi(\mathbf{r}, t) = -\frac{e^2}{2m_e \gamma \hbar} \int \mathrm{d}\tau \left(A_x^2(\mathbf{r} - \mathbf{v}t + \mathbf{v}\tau, \tau) + A_y^2(\mathbf{r} - \mathbf{v}t + \mathbf{v}\tau, \tau) + \frac{1}{\gamma^2} A_z^2(\mathbf{r} - \mathbf{v}t + \mathbf{v}\tau, \tau) \right) \tag{2.64}$$

For the second-order interaction, as suggested by $e^2 A^2(\mathbf{r}, t)$, a similar approach can be made to further constrain the possible solutions for the effective scattering phase. For

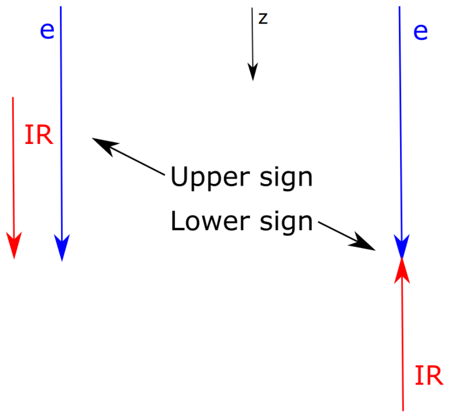

Figure 2.2.: Sketch of the co- and counter-propagating free electron e (blue) and IR laser (red) pulses. In the derivations, the upper sign of a double sign, i.e. $\pm$ or $\mp$, is always referring to a co-propagating setting, while the lower sign refers to a counter-propagating setting.

real fields in plane wave expansion, i.e. $A(\mathbf{r},t) \propto \sin(\mathbf{k}_L\mathbf{r} - \omega_L t)$, the associated complex field is found via:

$$A^2(\mathbf{r},t) \propto \sin^2(\mathbf{k}_L\mathbf{r} - \omega_L t) = \frac{1-\cos(2(\mathbf{k}_L\mathbf{r} - \omega_L t))}{2} \widehat{=} \frac{1-e^{i2(\mathbf{k}_L\mathbf{r} - \omega_L t)}}{2} \tag{2.65}$$

Here, the oscillating part is written as a complex function, keeping in mind that only the real part is taken for physical properties. Using the same argumentation as for the first order interaction case, it is clear that the time-varying part of the light field, i.e. $e^{-i2\omega_L t}$, is vanishing within the integral such that φ is not anymore explicitly dependent on the time. The non-time varying components remain, such that $\varphi(\mathbf{r},t) = \varphi(x,y)$. The 2-photon absorption and emission event is of a virtual nature, representing stimulated elastic Compton scattering.

To find a solution to the integral in eq. 2.64, the light field, represented by the electro-magnetic vector potential $\mathbf{A}(\mathbf{r},t)$ in the chosen gauge, has to be defined. Given the experimental setup as seen in Chapter 3, the light field is a pulsed paraxial laser beam propagating along the same axis as the electron beam, which is assumed to be monochromatic [1].

In the experiment (Chapter 3.1), optics of small numerical apertures are used, i.e. $NA < 0.2$. This implies that a paraxial approximation ($\sin(\theta) = \theta$)) for the light field can be used [60] with an error of $< 1\%$. Therefore, the z-axis component of the light field vanishes in first order, i.e. $A_z^2(\mathbf{r},t) \approx 0$.

The parallel setup allows for a laser beam co- or counter-propagating to the electron beam. This is denoted here by $\pm z$, with positive definite z, where the upper sign always denotes the co- and the lower sign always the counter-propagating setting. A sketch of the two notation settings is shown in fig. 2.2.

For a parallel pulsed laser light setting it is convenient to couple the time coordinate t to the coordinate of direction of propagation z with the retarded time coordinate $t \mp z/c$. Retarded time refers to the specific point in time at which the light is detected at a particular location in space, taking into account the time required for the electromagnetic field to propagate from its source to that location. The electric field component $\mathbf{E}(\mathbf{r}, t)$ of the pulsed laser can be written as:

$$\mathbf{E}(\mathbf{r}, t) = \mathcal{E}_0 \mathbf{n}_{(x,y)} g(x, y) e^{-i\omega_L(t \mp z/c)} u\left(t \mp \frac{z}{c}\right) \tag{2.66}$$

With the central laser frequency ω_L, the characteristic field strength $\mathcal{E}_0$, the polarization unit vector $\mathbf{n}$ in the transverse plane (x, y), the transverse beam profile $g(x, y)$ and the temporal pulse envelope $u(t \mp z/c)$. Complete separation of transverse $[\mathbf{n}_{(x,y)} g(x, y)]$ and longitudinal $[\exp(-i\omega_L(t \mp z/c))u(t \mp z/c)]$ profile is possible due to the fact, that the electrons only interact with the light field in focus.

The real-valued vector potential is connected to the electric field component via $\mathcal{R}e\{\mathbf{E}(\mathbf{r}, t)\} = -\partial_t \mathbf{A}(\mathbf{r}, t)$. Since the pulse width of the laser pulse ($\Delta t = 280$fs) is much larger than the optical oscillation period $2\pi/\omega_L = 3.5$fs, the vector potential, to leading order, is:

$$\mathbf{A}(\mathbf{r}, t) = -\frac{\mathcal{E}_0}{\omega_L} \mathbf{n}_{(x,y)} g(x, y) \sin\left(\omega_L\left(t \mp \frac{z}{c}\right)\right) u\left(t \mp \frac{z}{c}\right) \tag{2.67}$$

Using the vector potential of eq. 2.67 for the calculation of the effective scattering phase in eq. 2.64, the phase reads as:

$$\varphi(\mathbf{r}) = \frac{e^2 \mathcal{E}_0^2 g^2(x, y)}{2m_e \gamma \hbar \omega_L^2} \int \mathrm{d}\tau \sin^2\left(\omega_L\left(\tau \mp \frac{z - vt + v\tau}{c}\right)\right) u^2\left(\tau \mp \frac{z - vt + v\tau}{c}\right) \tag{2.68}$$

Performing a substitution by $\tau \mp \frac{z-vt+v\tau}{c} \longrightarrow t$, and introducing $\beta = v/c$, the calculation further reduces to:

$$\varphi(\mathbf{r}) = \frac{e^2 \mathcal{E}_0^2 g^2(x, y)}{2m_e \gamma \hbar \omega_l^2 (1 \mp \beta)} \int \mathrm{d}t \sin^2(\omega_L t) u^2(t) \tag{2.69}$$

The squared sine function can be rewritten as $\sin^2(\omega_L t) = (1 - \cos(2\omega_L t))/2$. Consequently, the integral over $u^2(t)\cos(2\omega_L t)$ can be neglected just like in eq. 2.65, because $u(t)$ is a slowly varying envelope. This effectively leads to the cosine function within the integral to average out to zero.

Thus, the calculation reduces to:

$$\varphi(\mathbf{r}) = \frac{e^2 \mathcal{E}_0^2 g^2(x, y)}{4m_e \gamma \hbar \omega_L^2 (1 \mp \beta)} \int_{-\infty}^{\infty} \mathrm{d}t u^2(t) \tag{2.70}$$

In order to solve this integral, it is convenient to use the definition of the laser pulse energy E_L. The laser pulse energy is obtained by integrating the absolute of the Poynting vector $|\mathbf{S}|$ over the pulse duration, as well as over the surface through which the laser traverses. The Poynting vector is defined as the cross product between the electric and magnetic field $\mathbf{S} = \mathcal{R}e(\mathbf{E}) \times \mathcal{R}e(\mathbf{H})$ with $\mathbf{H} = c\epsilon_0 \hat{\mathbf{e}}_z \times \mathbf{E}$ to leading order, where ϵ_0 is the vacuum permittivity.

The laser pulse energy is then:

$$E_L \approx c\epsilon_0 \mathcal{E}_0^2 \int \mathrm{d}t u^2(t) \cos^2(\omega_L t) \int \mathrm{d}x\mathrm{d}y g^2(x,y) \tag{2.71}$$

Using the same trick as in eq. 2.69 by rewriting $\cos^2(\omega_L t) = (1 + \cos(2\omega_L t))/2$ and neglecting the integral over $u^2(t)\cos(2\omega_L t)$, eq. 2.71 can be rearranged to:

$$\int u^2(t) = \frac{2E_L}{c\epsilon_0 \mathcal{E}_0^2} \frac{1}{\int \mathrm{d}x\mathrm{d}y g^2(x,y)} \tag{2.72}$$

Substituting eq. 2.72 into eq. 2.70, and using the definitions for the laser wavelength $\lambda_L = 2\pi c/\omega_L$, the fine structure constant $\alpha = e^2/(4\pi\epsilon_0\hbar c)$ and the relativistic electron energy $E_e = \gamma m_e c^2$, the effective scattering phase is:

$$\varphi(x,y) = -\frac{\alpha}{2\pi(1 \mp \beta)} \frac{E_L}{E_e} \frac{\lambda_L^2 g^2(x,y)}{\int \mathrm{d}x\mathrm{d}y g^2(x,y)} \tag{2.73}$$

The magnitude of this scattering phase is governed by the ratio of the laser pulse energy to the electron energy, while the shape is dependent on the square of the transverse light field profile $g^2(x,y)$.

An additional check for the validity of eq. 2.73 is its Lorentz covariance. The same value is obtained in the electron rest frame, when using the transformed rest frame values $\beta' = 0$, $E_e' = m_e c^2$, $\lambda_L' = \lambda_L \sqrt{(1 \pm \beta)/(1 \mp \beta)}$ and $E_L' = E_L \sqrt{(1 \mp \beta)/(1 \pm \beta)}$.

Furthermore, it can be seen in eq.2.73, that a different setting of the parallel-propagation, i.e. co- or counter-, does not impose different effects on the phase modulation, but gives a different scaling. This scaling is comprised in the relativistic Doppler factor $1/(1 \mp \beta)$, which accounts for any change of electron velocity along the propagation axis, while keeping the laboratory frame values in eq. 2.73.

Figures 2.3 and 2.4 show a colormap for the induced phase shift to get a first impression of the energies typically required to get phase shifts of a few multiples of π.

Figure 2.5 displays the required laser pulse energy per μm^2 to get a phase shift to a maximum of 2π for an electron acceleration energy of 30keV. Figure 2.6 displays the required electron acceleration energy to get a phase shift to a maximum of 4π for a laser pulse energy of $0.3\mathrm{nJ}/\mu m^2$. In anticipation to the presented experiment in Chapter 3, where a 30keV electron beam is used in counter-propagating mode, it is shown in fig. 2.5, that already a laser pulse energy of $0.6\mathrm{nJ}/\mu m^2$ is enough to generate a 2π phase shift. Energies of such scales are easily achieved with modern pulsed lasers. Further images of phase shifts for different laser pulse energies and electron acceleration energies are shown in appendix A.5.

In summary, equation 2.73 shows that the transverse profile of an electron pulse $\phi_\perp(\mathbf{r},t)$ can be shaped by a parallel-propagating light field, i.e. as realized through a pulsed laser. Thus, having control over this intensity pattern leads to control over the phase profile of the electron beam. Control over the light intensity pattern is experimentally realized through a spatial light modulator, which will be described in Chapter 3.3.

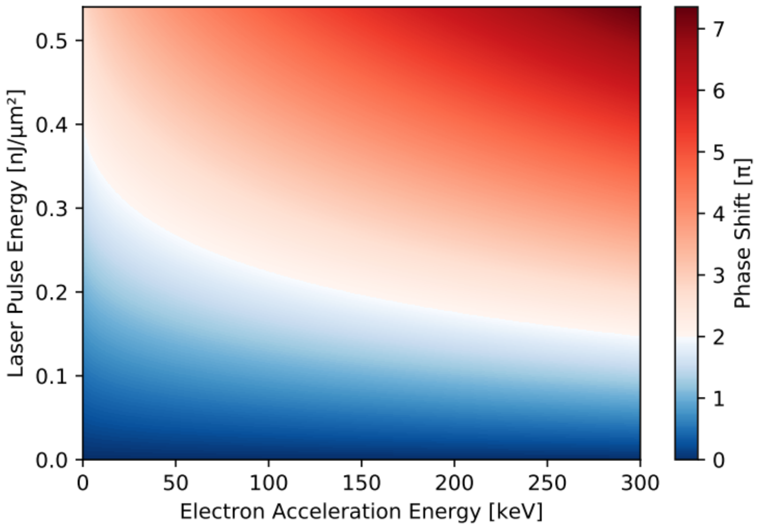

Figure 2.3.: Colormap of the phase shift as a function of laser pulse energy and acceleration energy for co-propagating light and electrons. The white line visualizes the 2π phase shift.

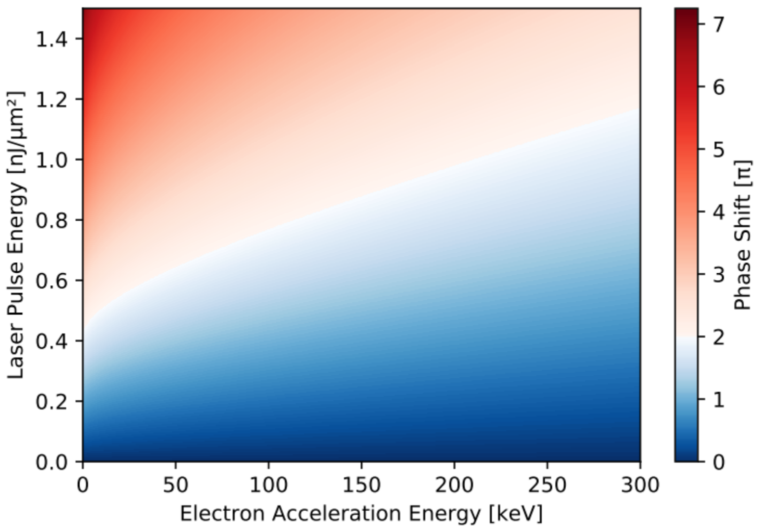

Figure 2.4.: Colormap of the phase shift as a function of laser pulse energy and acceleration energy for counter-propagating light and electrons. The white line visualizes the 2π phase shift.

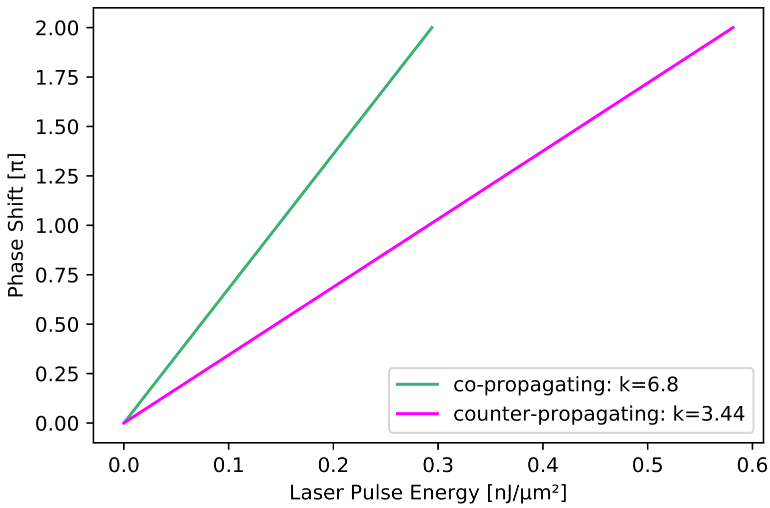

Figure 2.5.: Phase shift as a function of light pulse energy density at a constant electron acceleration energy of 30keV. Both the co- (green) and counter- (magenta) propagating cases are displayed. The slopes k are for the linear functions $\varphi(E_L) = kE_L$.

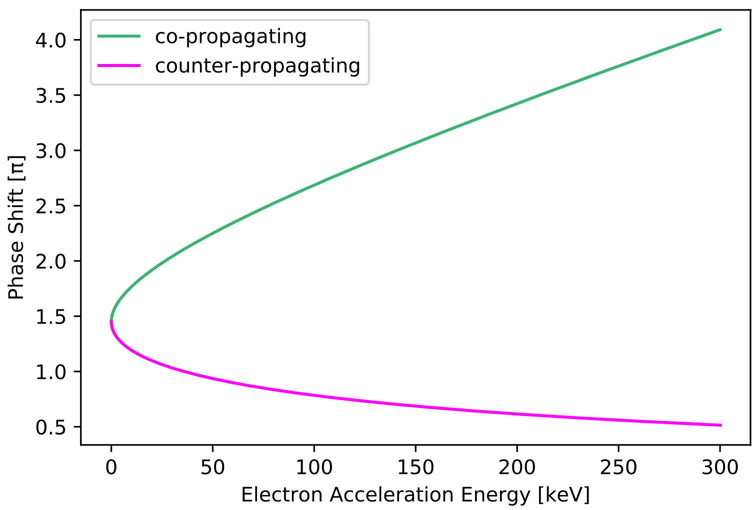

Figure 2.6.: Phase shift as a function of electron acceleration energy at constant light pulse energy density $0.3\text{nJ}/\mu m^2$. Both the co- (green) and counter- (magenta) propagating cases are displayed.

2.5.3. From the Scattering Phase to Classical Mechanics

The scattering phase in eq. 2.73 can effectively lead to a change of direction of electrons in a classical picture. Thus, a different approach to understanding electron-photon interactions in parallel-propagating mode is realized by looking at the electrons as ballistic particles with classical position and momentum within a light field.

The classical Hamiltonian for such an electron [57] is the total energy as discussed in Chapter 2.4:

$$\mathcal{H}(\mathbf{r}, t) = \sqrt{m_e^2 c^4 + c^2(\mathbf{p} - e\mathbf{A}(\mathbf{r}, t))^2} \tag{2.74}$$

Solving the Hamilton equations for this Hamiltonian by using the vector field of eq. 2.67, as well as using several approximations already made in Chapter 2.5, leads to an expression for the transverse momentum kick $\mathbf{\Delta p}(x, y)$. This momentum kick is received by an electron as a result of scattering off the light field:

$$\mathbf{\Delta p}(x, y) \approx -\frac{\alpha}{2\pi(1 \mp \beta)} \frac{E_L}{E_e} \frac{\lambda_L^2 \hbar \nabla g^2(x, y)}{\int g^2(x, y)} \tag{2.75}$$

Comparing this to eq. 2.73, it is clear that a direct connection between classical transverse momentum kick and quantum mechanical phase modulation φ can be made via:

$$\Delta\mathbf{p} = \int \mathbf{F}_p \mathrm{d}t = -\int \nabla U_p \mathrm{d}t = -\nabla \int U_p \mathrm{d}t = \hbar\nabla\varphi \tag{2.76}$$

Equation 2.76 is especially suitable for raytracing of electron beams. Furthermore, since the spatial dependence of the phase modulation comes from the intensity of the light field, the direction of the momentum kick is determined by the gradient of the intensity:

$$\Delta\mathbf{p}(x, y) \propto -\nabla I(x, y) \tag{2.77}$$

2.6. Coherence of Ponderomotively Affected Electron Beams

Coherence is a measure of the ability of two or more separated waves to show interference. Coherence is distinguished between transverse and longitudinal coherence. Transverse (longitudinal) coherence is the ability of two transversely (longitudinally) separated points in the wave packet to interfere.

This chapter discusses, whether ponderomotive beam shaping affects the coherence of an incoming electron beam. As discussed in Chapter 2.5.1, the electron-photon interaction is of a virtual nature. Thus, no energy transfer occurs, and the interaction per se should not cause decoherence due to a change of wavelengths [28].

However, the interacting light field imposes a spatial change onto the electron beam. This change is either of longitudinal nature, as seen in Chapter 2.4, or of transverse nature, as seen in Chapter 2.5.3.

Regarding the longitudinal change as seen in Chapter 2.4.1, the group velocity of electrons within a light field gets smaller with the light field intensity. As discussed, if the light field intensity varies in the transverse plane, spatially separated partial electron waves have different group velocities. Consequently, decoherence occurs when either the longitudinal shift Δz of the wave exceeds the coherence length l_c of the electron pulse [62]. In an extreme case, the longitudinal shift can even be larger than the electron pulse length l_e itself.

The longitudinal shift is calculated via the group velocities in eq. 2.16 and 2.17 and the laser pulse duration via

$$\Delta z = (v_{g,f} - v_{g,EM})\Delta t \ . \tag{2.78}$$

The coherence length depends on the energy properties of the electron beam, expressed via the electron wavelength and its spread, i.e.

$$l_c = a\frac{\lambda_e^2}{\Delta\lambda_e} \ , \tag{2.79}$$

where a is a numerical factor of the order of 1 [63]. The electron wavelength in the presented research is about $\lambda_e = 7$pm, while its spread is about $\Delta\lambda_e = 0.06$fm. The spread of the wavelength is calculated using an energy spread of $\Delta E_{acc} = 0.5eV$, which is typical for pulsed electron Schottky emitters [59] as presented in Chapter 3.2.

Thus, the longitudinal shift with $\Delta z = 0.41$pm is much smaller than both the coherence length with $l_c = 0.8\mu$m and the electron pulse length with $l_e = 127\mu$m and should therefore only impose very weak broadening and decoherence effects.

Since the phase shifts are proportional to $I(x, y)$, noise on $I(x, y)$ would lead to decoherence. Due to the stability of the used laser (Chapter 3.1), this effect can be neglected in the presented experiment.

2.7. Ponderomotive Electron Lenses

In this chapter, a first application of electron beam phase modulation via light fields is discussed. As already suggested in Chapter 2.4 and sketched in fig. 2.1, different shapes of light fields could be used for negative and positive electron lensing.

A perfect lens with focal length f_e induces a phase modulation of [60]

$$\varphi_{lens}(R) = -\frac{\pi}{f_e\lambda_e}R^2 \ . \tag{2.80}$$

In order to create a ponderomotive lens, an intensity distribution has to be found, such that the induced phase shifts (eq. 2.73) match eq. 2.80. Here, $R = \sqrt{x^2 + y^2}$ is the radial distance from the optical axis, i.e. the propagation axis of the electron beam, and f_e is the focal length of the perfect lens. The focus length is positive for convex and negative for concave lenses.

The creation of a convex lens is accomplished by using the center of a Laguerre-Gauß mode with azimuthal and radial indices 1 and 0 (LG10) for the spatial intensity profile, i.e. $g^2(x, y) = g_{10}^2(R)$, with

$$g_{10}^2(R) = \left(\frac{R}{w_{10}}\right)^2 \exp\left[-2\left(\frac{R}{w_{10}}\right)^2\right] \ , \tag{2.81}$$

where w_{10} is the beam waist of the Laguerre-Gauß light beam.

The Taylor expansion around the centre $R = 0$ gives $g_{10}^2(R) \approx (R/w_{10})^2 + \mathcal{O}(R^4)$, which has the sought for positive quadratic dependency on R. The integral of the spatial light intensity profile over the two-dimensional space is $\int_{\mathbb{R}^2} g_{10}^2(R) = \pi w_{10}^2/4$. Using the integral in the denominator and the Taylor expansion in the numerator in eq. 2.73 gives the convex electron lens focus length:

$$f_e = \frac{(1 \mp \beta)\pi^3}{2\alpha} \frac{E_e}{E_L} \frac{w_{10}^4}{\lambda_L^2 \lambda_e} \tag{2.82}$$

On the other hand, the creation of a concave lens is accomplished by using the center of a Gauß mode (LG00) for the spatial intensity profile, i.e. $g^2(x, y) = g_{00}^2(R)$, with

$$g_{00}^2(R) = \exp\left[-2\left(\frac{R}{w_{00}}\right)^2\right] , \tag{2.83}$$

where w_{00} is the beam waist of the Gaussian light beam.

Using the same process as for the convex lens, the Taylor expansion around the center $R = 0$ gives $g_{00}^2(R) \approx 1 - 2(R/w_{00})^2 + \mathcal{O}(R^4)$. This has the required negative quadratic dependency on R, omitting the overall constant phase modulation in the zeroth order. The integral of the spatial light intensity profile over the two-dimensional space is $\int_{\mathbb{R}^2} g_{00}^2(R) = \pi w_{00}^2/2$. Again, using the integral in the denominator and the Taylor expansion in the numerator in eq. 2.73 gives the concave electron lens focus length:

$$f_e = -\frac{(1 \mp \beta)\pi^3}{2\alpha} \frac{E_e}{E_L} \frac{w_{00}^4}{\lambda_L^2 \lambda_e} \tag{2.84}$$

In a very different setup, but still using electron-light interactions, Uesugi *et al.* [64] proposed the creation of convex and concave lenses for non-relativistic electrons as a result of similar spatial intensity profiles as in eq. 2.81 and 2.83.

3. Experiment

The theory in Chapter 2 describes the possibility of pulsed free electron beam wave-front shaping. This shaping is realized by a parallel-propagating pulsed light field satisfying the paraxial approximation and having a well-known intensity shape.

Thus, the main parts of the experiment consist of:

- A pulsed laser to generate the interacting light field as well as to trigger the pulsed electron beam (Chapter 3.1)
- A modified scanning electron microscope (SEM) to generate a pulsed free electron beam (Chapter 3.2)
- A spatial light modulator (SLM) to have control over the wave-front of the light field (Chapter 3.3)
- An electron detection system (Chapter 3.4)

Naturally, all these parts are connected. Therefore, alignment methods are either described in the respective chapter or in Chapter 3.5.

3.1. The Femtosecond Laser

The laser that is used in the presented research is a commercial Coherent Monaco femtosecond laser with an infrared (IR) wavelength of 1035nm, and a pulse length of 280fs [1]. The repetition rate is set to 1MHz for the whole experiment. At the same time, the pulse energy is varied depending on the required electron wave-front modulation, with a maximum of 40μJ initial pulse energy. The laser beam path is split into various beam paths, each with its task in the experiment.

First, the IR beam is split with a 93:7 beam splitter. The beam splitter sends 7% intensity of the IR beam through two β-barium borate nonlinear crystals (BBO). The first BBO (EKSMA Optics, 6x6x3mm, phase matching angle θ =23.4) uses the IR light and partly generates green light via parametric up-conversion [65], while the second BBO (EKSMA Optics 6x6x0.5mm, θ =49.6) generates ultraviolet (UV) light using green light. Second, a semi-transparent mirror, which reflects UV light and is transparent in green light, is used to separate the two wavelengths, having in total three beam paths, i.e. green, UV, and IR.

As later described in Chapter 3.2, the original SEM sample chamber door was replaced by a custom-made door that possesses mounts to hold an optical breadboard on which optical elements for the laser beam are placed. Furthermore, optical breadboards are placed around the SEM for the UV beam. The SEM is not placed on the same pneumatic optical table as the laser. Therefore, an active beam-pointing stabilizing system (Aligna, TEM-Messtechnik) is necessary to adjust for vibrations between the SEM and the optical table of the laser and correct for pointing instabilities of the laser, i.e. 25μrad for the used laser. Thus, two piezo-actuated mirrors are placed on the optical tables of the SEM and the laser respectively, which are controlled digitally to compensate for instabilities.

The UV beam propagates through a half-wave plate to have control over its polarization and is then focused with a 15cm focal length lens into the SEM and onto the Schottky electron gun. Here, the laser pulses generate electron pulses, which is described in more detail in Chapter 3.2.

The main part of the IR, i.e. 97%, is used to create the ponderomotive potentials for electron beam shaping. It first passes a delay stage, which is used to prolong or shorten the length of the IR compared to the UV path. Thus, the delay stage ensures that the electron and IR pulses overlap in the interaction plane within the SEM. Furthermore, IR and UV traverse through motorized half-wave plates (HWP) placed in front of polarizing beam splitters to adjust the laser power separately.

After the delay stage, the IR path leads to the optical breadboard mounted to the chamber door. There, the IR pulse gets magnified to a 7.5mm $1/e^2$ diameter onto the SLM. After getting reflected and acquiring a phase distribution from the SLM, described in more detail in Chapter 3.3, the beam propagates through a lens with a focal length of 200mm, where the sought-for intensity distribution is visible in the focal plane. The focus spot is further five times de-magnified by a 4f-system with 250mm and 50mm convex lenses. The resulting focus spot has a diameter of 4.3μm full-width-half-maximum (FWHM) for a Gaussian beam, as seen in Chapter 4, or typically 16μm for more complex shapes. It defines the interaction plane (IP) within the sample chamber.

Within the SEM sample chamber, the electron and IR pulse are made parallel by an unprotected gold mirror on a copper substrate as seen in fig. 3.1a. The gold mirror reflects the IR, and transmits electrons through a drilled hole in the center. The gold layer is unprotected to minimize charging, the substrate is made from copper to minimize heating.

After propagating through all the necessary components, the IR pulse has a pulse energy of $< 17.2\mu$J. Extrapolating the linear plot of fig. 2.5 shows that the given pulse energy would be enough to modulate the phase several hundreds of rad. Furthermore, a small CMOS (OV5647), modified for high vacuum use, can be placed in the IP to image the focus spot directly.

After the IP, the IR beam is out-coupled with a second mirror and a lens. This out-coupling multiple reasons. First, reducing heating processes within the SEM. Second, imaging of the laser beam after the interaction via a CMOS outside the sample chamber. Third, spatial and temporal overlapping of electron and laser pulse, as described in detail in Chapter 3.5.2.

3.2. Modification of the Scanning Electron Microscope

The most basic distinction between electron microscope types can be made between transmission electron microscopes (TEM) [58] and scanning electron microscopes (SEM) [66]. TEMs operate by the transmission of electrons through the sample with common electron acceleration energies of 70-300keV, creating an image via diffraction. As opposed to that, SEMs use a beam of electrons that is focused and directed onto the surface of a specimen. As the beam interacts with the atoms of the material, it induces the emission of diverse signals, such as secondary electrons, backscattered electrons, and X-rays. These can be detected and utilized to create an image. Common electron acceleration energies of SEMs are 5-30keV.

Due to the operational mode, TEMs rely heavily on coherence, while SEMs do not [67]. Furthermore, due to the operating modes, TEMs, while being larger than SEMs, have much smaller sample chambers of about 3-7mm diameter in contrast to SEMs with sample chambers of about 30cm in diameter.

The optical elements for the IR beam path are placed in the sample chamber. Therefore, a larger sample chamber is much more convenient for observing ponderomotive phase modulation. Consequently, the electron microscope used for the presented research is a self-modified version of a commercial SEM (FEI XL30). A sketch of the electron beam path through the electron microscope is shown in fig. 3.1a. The three main modifications of the SEM are [1]:

First, instead of using the commercial tip in continuous mode, the Schottky electron gun is triggered by a focused pulsed UV beam [67]. The UV beam is polarized parallel to the tip via a half-wave plate. This generates a pulsed electron beam with, initially, approximately the same pulse length Δt_e as the laser, i.e. 280fs. After propagating through the electron column, the pulsed electron beam broadens due to space charge effects. This broadening is minimized using less than one electron per pulse on average, circumventing space charge effects [68]. At the interaction region, approximately at the same place as the specimen would have been in an ordinary SEM, the electron pulse has a pulse length of $<$500fs FWHM [69] with a Gaussian shape in the temporal domain.

Second, the SEM sample chamber is completely rebuilt to fit two mirrors and lenses. A 3D image of the elements in the sample chamber is shown in fig. 3.1b. The optical elements are necessary to focus the IR laser beam used for the electron-light interaction and to set it parallel to the electron beam. The mirrors have a central 1.5mm hole drilled in through which the electron beam can propagate. Thus, the IP is between those mirrors and under the objective lens of the SEM. The custom sample door is made of aluminum with a CF 100 window, such that the IR laser beam can propagate through the window. Furthermore, a mechanical stage was mounted between the mirrors. This stage holds either the small CMOS that images the IR in the IP or a scintillator and a copper grid necessary for accomplishing spatial and temporal overlap, as later described in Chapter 3.5.2.

Third, the bottom of the SEM was opened, and a microchannel plate (MCP) was placed beneath the sample chamber, i.e. 550mm below the IP, so that the SEM is used in

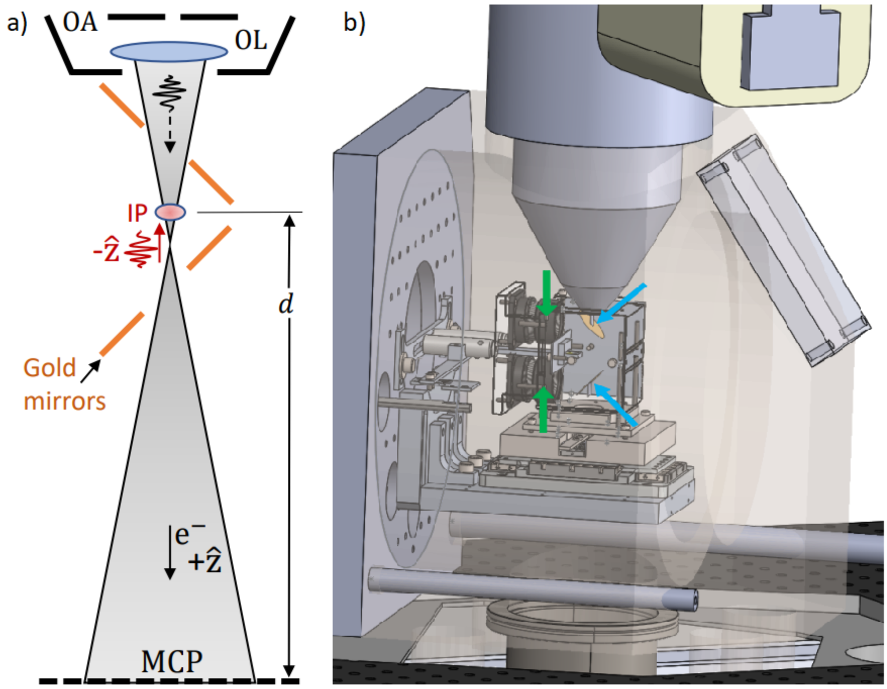

Figure 3.1.: a) Sketch of the electron beam path (e^-, grey area in positive z-direction) after the 100μm objective aperture (OA) in the modified SEM. The tunable objective lens (OL) focuses the electron pulse (black pulse) below the interaction plane (IP), where the interaction with the counter-propagating laser pulse (red pulse in negative z-direction) takes place. The electron pulse propagates through the holes in the gold mirrors (yellow), while the laser pulses are in- and out-coupled by them. The electron beam can be steered to propagate through the holes and overlap with the laser beam. The optical elements are mounted on a piezo stage for fine tuning of the electron-light overlap. After the interaction, the electron pulse is recorded in transmission mode by a microchannel plate (MCP) (dashed line). b) 3D image of the modified sample chamber. The original SEM sample chamber door was replaced by a custom-made aluminum door with a window in the center for the laser pulse. Thus, the laser pulse traverses through the window, comes into the chamber from the left, gets focused by a lens (see bottom green arrow), and is reflected onto a counter-propagating path by the first gold mirror (see bottom blue arrow). In between the mirrors is the IP. After the interaction, the laser pulse is out-coupled by the second gold mirror and imaged onto a CMOS outside of the vacuum chamber. A mechanical stage is implemented that can slide a scintillator and copper grid or a small CMOS from the left in the interaction region. The images were taken and adapted from Mihaila *et al.* [1].

transmission mode. The MCP functions as the electron detection system, as described in Chapter 3.4.

Since the electron microscope works with charged particles, magnetic fields coming from sources outside the SEM can influence the electron beam. The noise level from these stray magnetic fields should be lower than 0.1mG root-mean-square [70]. To prevent such noise, magnetic field compensation is implemented via active shielding (Stefan Mayer Instruments).

Thus, electron phase modulation via counter-propagating electron and IR beam, as described in Chapter 2, is achieved and observed. A full sketch of the interplay between laser and SEM is shown in fig. 3.2.

3.3. Light Wave-Front Shaping Mechanism

It is shown in eq. 2.73, that the scattering phase modulation of the electron wave-front is proportional to the intensity pattern of the light field. Thus, having control over the intensity pattern implies control over the effective scattering phase pattern.

As mentioned in Chapter 2.1, control over the wave function of a light field can be realized by an SLM via eq. 2.2. The following chapters describe the functional principle of an SLM (Chapter 3.3.1) and the algorithm used to create the applied phase masks (Chapter 3.3.2).

3.3.1. The Spatial Light Modulator

The SLM used for the presented research is a commercial Meadowlark Spatial Light Modulator with 1920x1152 pixels and a pixel size of 9.2μm [1]. It is water-cooled to avoid heating effects and damage due to high laser pulse powers.

A sketch and the working principles of a liquid crystal SLM are shown in fig. 3.3. The light field propagates through the cover glass, the first transparent electrode, and liquid crystals before getting reflected at the second electrode. The electric field between the electrodes is controlled pixel-by-pixel by an active matrix circuit, which in turn adjusts the orientation of the liquid crystal molecules. The applied voltage is controlled digitally. The light field, propagating through the liquid crystal twice, acquires a phase shift dependent on the orientation of the liquid crystal molecules [71].

3.3.2. The Gerchberg-Saxton Algorithm

Shaping of ponderomotive potentials can be achieved in various ways. Using an SLM, the wave-front of an incoming light pulse can be shaped. If chosen appropriately, this phase modulation in the SLM plane can result in the desired light intensity distribution in the interaction plane (IP) after propagating through a specific optical setup.

The Gerchberg-Saxton algorithm (GSA) [72] allows for calculating the required phase modulation. In order to describe the GSA, the SLM plane and the target plane are defined. The SLM plane is the plane, on which the phase masks are implemented. The target plane, is the plane where a certain phase or intensity distribution is wanted. In the

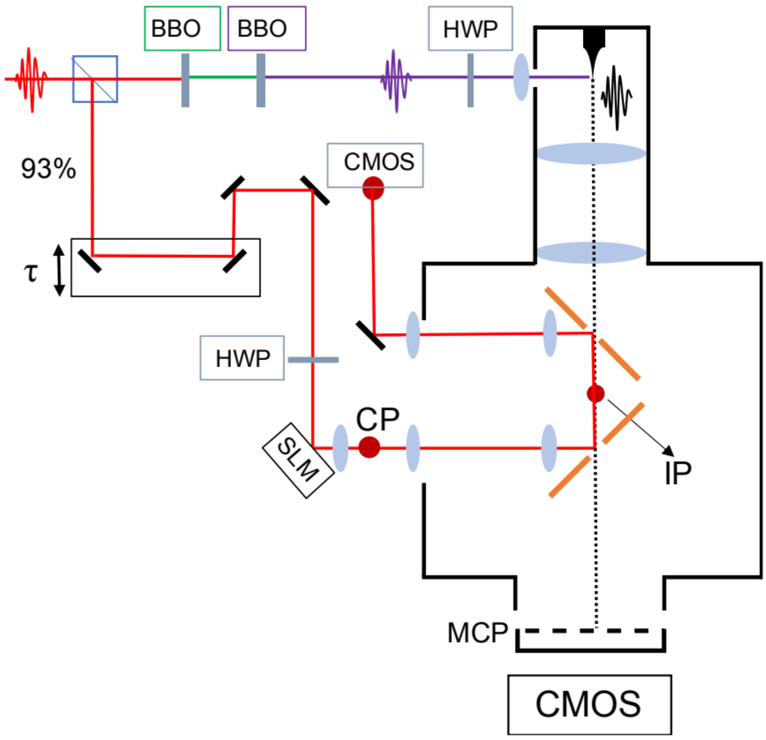

Figure 3.2.: Sketch of the experimental setup. The infrared (IR) pulse (red) is split by a beam splitter. One path leads through two BBO crystals, and the resulting ultra-violet (UV) beam (purple) is adjusted via a half-wave plate and a polarizer (HWP). The UV beam is then used to generate electron pulses (black) via the Schottky gun (black). The electron pulses propagate through the electron microscope column, i.e. condenser lens (upper) and objective lens (lower), including an objective aperture, before crossing the interaction plane (IP). Meanwhile, the IR path includes a delay stage to adjust the timing τ, a HWP, and the spatial light modulator (SLM). After the SLM, a lens focuses the IR in a plane (CP) conjugate to the IP. Two convex lenses in a 4f-system de-magnify the focus spot to the IP. The lower gold mirror reflects the IR such that it propagates anti-parallel to the electron pulse. After the interaction, the electron pulses are recorded via a microchannel plate (MCP) and a CMOS. The image was taken and adapted from Mihaila *et al.* [1].

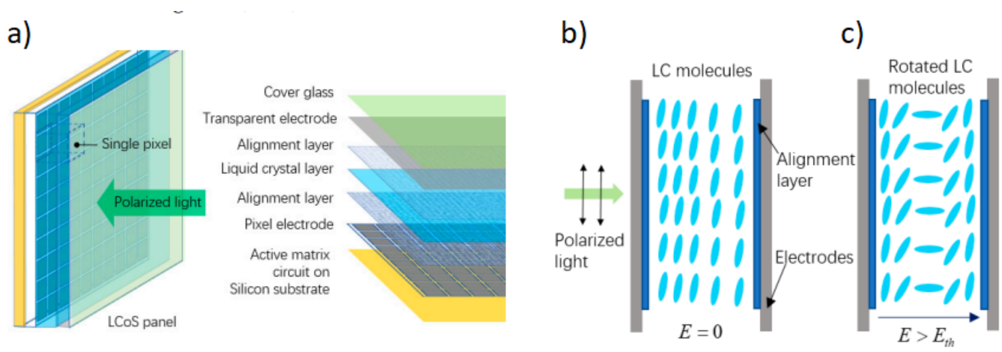

Figure 3.3.: a) Layer construction of a liquid crystal (LC) SLM. b) SLM without a phase mask. c) SLM with a phase mask, the applied pixel-wise voltage changes the orientation of the LC molecules, inducing a phase shift to the light field. The images were taken and adapted from Li and Cao [71].

original GSA, the target plane is in the SLM plane's far field. The target plane is the IP in this experiment. Phase modulation typically requires rather high powers. Therefore, the SLM is only used for phase modulation and not for amplitude modulation tool.

Depending on the required electron beam shape, the required intensity pattern, i.e. the target pattern, is known in the IP, just as the initial intensity pattern on the SLM plane.

A common GSA [72] has been modified [1] to suit the presented experimental setup. A common GSA iteratively propagates the wave function via Fourier transforms from IP to SLM plane and back with an amplitude modulation in each plane. Starting with the IP, an inverse fast Fourier transform (IFFT) is performed on the target field with an arbitrary phase $\phi_0(x, y)$ and with an amplitude $A_{IP}(x, y)$ defined as the square root of the target intensity. This shifts the pattern to the SLM plane with a phase of ϕ_1 and an amplitude of $A_1(x, y)$. In the SLM plane, the calculated amplitude $A_1(x, y)$ is replaced by the amplitude of the source $A_{source}(x, y)$, i.e. the laser amplitude that hits the SLM. Then, a fast Fourier transform (FFT) is performed to get back to the target plane, where, again, the calculated amplitude $A_2(x, y)$ is replaced by the target amplitude, while the phase is kept. Thus, the GSA implements the following process (omitting the (x,y) dependency in the notation):

$$A_{IP}e^{i\phi_0} \xrightarrow{IFFT} A_1 e^{i\phi_1} \rightarrow A_{source}e^{i\phi_1} \xrightarrow{FFT} A_2 e^{i\phi_2} \rightarrow A_{IP}e^{i\phi_2} \tag{3.1}$$

Then the iteration starts again with $\phi_2(x, y)$ and the steps are repeated until the calculated amplitude in the target plane $A_{2n}(x, y)$, with n iterations, matches the target amplitude. As soon as this is the case, the calculated phase in the SLM plane, i.e. $\phi_{2n-1}(x, y)$, is the applied phase mask that will yield the desired target intensity.

As described in Chapter 3.1, the laser beam is reflected on a mirror with a drilled hole in the centre within the sample chamber. This means that the hole has to be implemented in the GSA to avoid heavy intensity loss, chamber heating, and unaccounted phase changes, like diffraction effects from the hole edges, in the laser wave-front. The modification of the GSA [1] is done by implementing a beam block, which simulates the hole and is put in the GSA via additional Fresnel transformations. The FFT and IFFT is thus replaced by lens T_L and beam block T_{bb} transfer functions as sketched in fig. 3.4. This leads to a solution for the phase mask, where the intensity loss in the hole is only about 5% of the total pulse energy.

The SLM is a powerful tool. However, there are limitations due to the quantized nature of the pixel screen, i.e. limited diffraction efficiency and resolution, and due to the liquid crystal properties, i.e. only linearly polarized light can be used. The GSA, too, has computational limitations connected to its quantized nature. It can happen that, through multiple iterations, neighboring pixels acquire phase differences of up to π, which can lead to unwanted local destructive interference effects. These are visible in the recorded image via speckles.

Such speckles can be efficiently prevented by taking a quadratic instead of a constant initial phase [73]. However, in the modified GSA, a constant phase is more suitable [1]. Another way of suppressing speckles is by restricting the target amplitude only to the important signal region, which globally imposes fewer restrictions to the modified GSA, i.e. the pattern outside the signal region does not matter, except for intensity loss.

Furthermore, the IR path includes a 4f-setup to de-magnify the wave-front pattern further down. The lenses would introduce aberrations to the laser beam, but these are easily corrected by applying an additional aberration-correcting phase mask onto the SLM. This aberration correction phase mask uses Zernike polynomials [74], and their coefficients [1] are determined experimentally by recording the focus spots directly in the IP with the small CMOS.

3.4. The Microchannel Plate

The electron detection system used in the presented research is a two-fold assembly of microchannel plates (MCP) [75] from Tectra Gmbh (MCP-025-D-L-F-V-P43-6MI) with a total MCP diameter of 18.8mm and a channel diameter of 6μm. This is followed by a P43 phosphor screen that converts electrons to light, which is then recorded via a CMOS camera. In general, an MCP can be used as a detection system for electrons, ions, neutrons and photons, depending on the configuration.

A schematic profile of a single plate is seen in fig. 3.5a. For electron detection, the incident electron directly hits the first plate on the front surface and channels through the plate, i.e. through glass substrate channels, due to the applied voltage on the front and back end of the MCP. On its way to the back surface, the electron hits the walls, consisting of an emissive layer covered by a resistive layer, multiple times and kicks more electrons out of the emissive layer. The resistive layer contains the electrons within one channel leading to an electron cascade.

Thus, the incident electron cascades through two plates before hitting the phosphor screen, as schematically shown in fig. 3.5b. The phosphor screen radiates photons with a peak wavelength of emission of 545nm.

The used MCP is assembled in a chevron configuration of two microchannel plates and

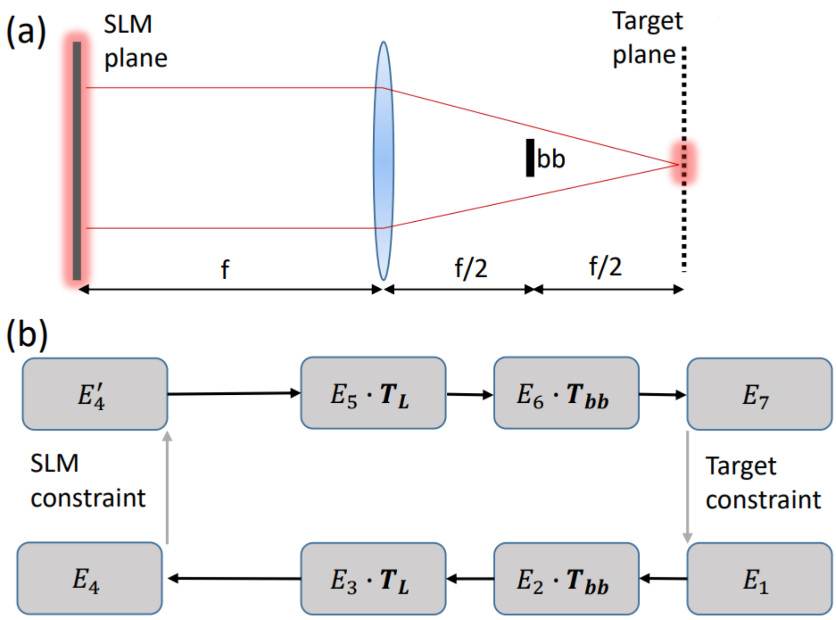

Figure 3.4.: a) Sketch of the laser beam path after the SLM, which has to be considered in the GSA. The laser wave front gets a phase pattern at the SLM plane and propagates through a lens. Before it reaches the focus spot in the target plane, a beam block is implemented to simulate the hole in the gold mirror. b) Sketch of the computation steps in the GSA. Starting from the target E_1, free propagation to the beam block yields E_2. E_2 is first propagated to the lens and then multiplied by the beam block transfer function T_{bb} to get to E_3. E_3 is then multiplied by the lens transfer function T_L. Another free propagation yields E_4 in the SLM plane. The amplitude of E_4 has to be changed to the original source amplitude, i.e. SLM constraint, to get E_4'. The whole process is then implemented in the other direction, i.e. SLM to target plane, where again the amplitude of E_7 is changed to the original target amplitude. This process is performed iteratively until the calculated target amplitude matches the original amplitude. The images were taken and adapted from Mihaila *et al.* [1].

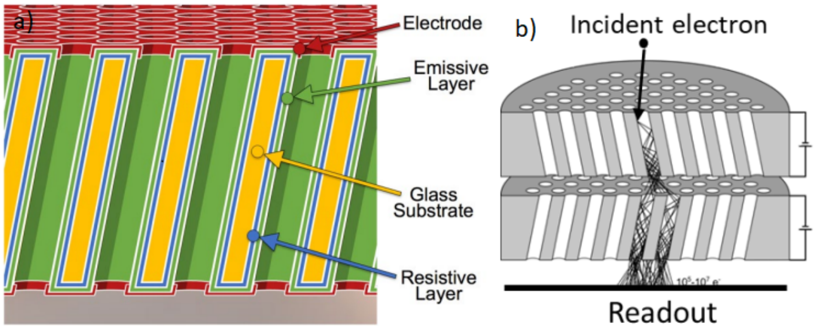

Figure 3.5.: a) Schematic profile of an MCP plate. The incident electron travels through the glass substrate (yellow) due to the applied voltage on the electrodes (red). On its way, it kicks out more electrons from the emissive layer (green), which are restricted to the channel by the resistive layer (blue). Thus, the electrons cascade through the plate. b) Schematic cascading of electrons in an MCP. The incident electron cascades through the two microchannel plates with a typical gain of $10^5 - 10^7$. In the presented research, the readout is a phosphor screen, followed by a CMOS. The images were taken and adapted from Cremer *et al.* [76].

a P43 phosphor screen. Skewed channels in the MCP help to suppress positive feedback of electrons by directing secondary electrons better through the channels and to increase the number of hits and subsequently the gain.

In the presented experiment, the second plate was set at 1.3kV and the P43 at 3.5kV, while the first plate was set to ground. With these settings, the gain was around 5×10^6 according to the datasheet of the MCP.

To record the emitted light from the P43, a CMOS (FLIR, GS3-U3-23S6M-C), with a peak sensitivity matching the scintillated light from the P43, is placed beneath a lens. The detected electron images were processed with a 2x2 median filter to avoid dead pixels.

To determine the resolution of the detection system, the point-spread function (PSF) is calculated. Five images were taken with the same voltage applied to the MCP as used in the research, i.e. 1.3kV and 3.5kV. The SEM was turned off such that the MCP only records single stray electrons within the electron microscope. An example image of this is shown in fig. 3.6a.

Single electrons were then identified via code, as described in appendix A.4, using the image processing software Fiji [77]. There, Otsu's segmentation method was carried out as well as re-processing via eroding, dilating and removing single outliers. The erosion operation works by moving a structuring element or kernel over the input image, pixel by pixel, and checking if all the pixels within the kernel are present in the image. If all the pixels in the kernel are present, the center pixel is retained in the output image, otherwise, it is removed. This process can be seen as shrinking the features of an image. Dilation can be seen as the opposite of erosion. The dilation operation is performed by moving a

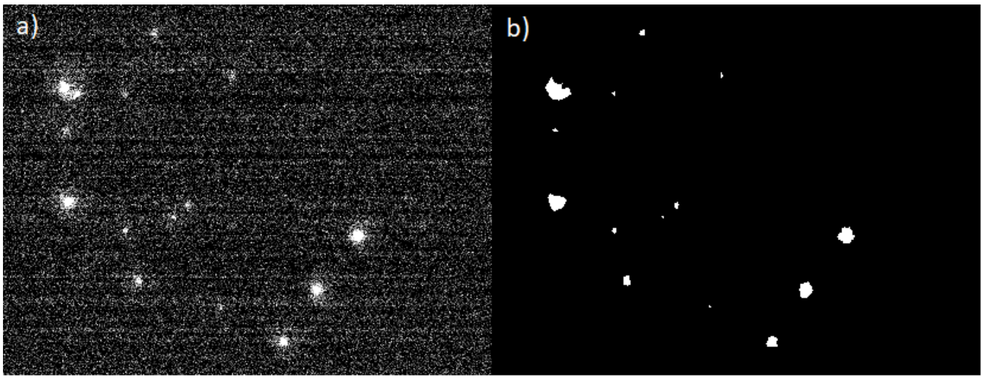

Figure 3.6.: a) Contrast-enhanced cropped image of the original image. b) Segmented and re-processed image.

structuring element over the image, pixel by pixel, and adding the center pixel if any of the pixels within the kernel are present in the image, leading to an expansion of image features. The combination of erosion ad dilation smooth out the identified electron spots. This leads to fewer single outliers that have to be removed while maintaining the overall shape of the electron spot.

An example image of this is shown in fig. 3.6b. This is done to determine the number of single electrons, their center pixel positions within the image, and their minor and major axis from an ellipsoid fitted around them.

The images were then analyzed with Python [78], which is also shown in appendix A.4. First, all data points, where the minor axis is less than 70% of the major axis, are removed since they have a high probability of signifying two particles. Then, using the center spot information from Fiji, a 32x32 pixel region of interest is defined around each spot as seen in fig. 3.7a. A two-dimensional Gaussian is fitted over the region of interest, as seen in fig. 3.7b, which gives an estimation of the peak position. The accuracy is not limited to the finite pixel size.

Then, the distance from the peak position to each pixel center is measured, and the pixel intensities are plotted against this distance r. A sketch of how the distances are measured is shown in fig. 3.8.

This measurement is carried out in a loop for every accountable single electron out of five full MCP images. Then all data points above 220μm are omitted to fit the important part of the data, which gives an array of 10974 data points with intensities versus the radii as seen in fig. 3.9a. To properly fit a function to this data, a Savitzky-Golay filter [79] (window size 601, polynomial 3) is applied to smooth the signal and fit a Voigt profile to the smoothed data as seen in fig. 3.9b. A Voigt profile is chosen, because it is a convolution of Lorentz and Gauss profile, offering more flexibility than a single Lorentz or Gauss profile.

The Voigt profile has a FWHM of 99.9μm and consists of the convolution of a Gaussian with 20.4μm FWHM and a Lorentzian with 95.2 FWHM. The uncertainty determined by the fit is 0.2μm, however, experience shows that the FWHM varies more than that with

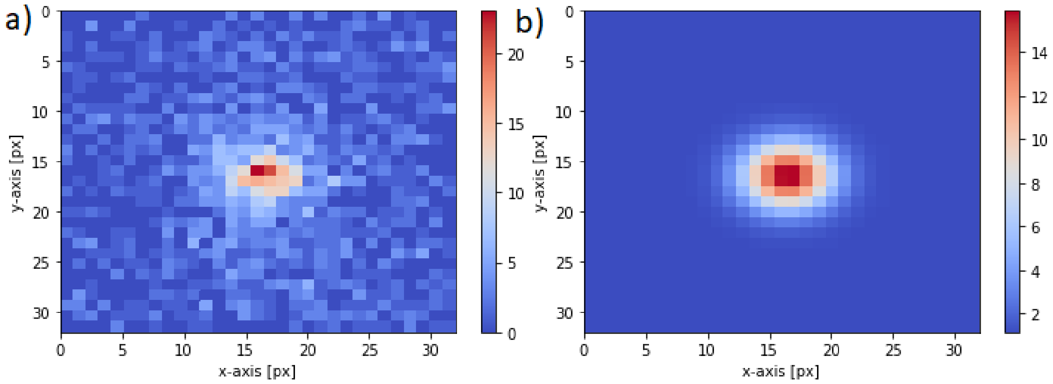

Figure 3.7.: a) Region of interest of a signal spot. b) Two-dimensional Gauss fit over the region of interest.

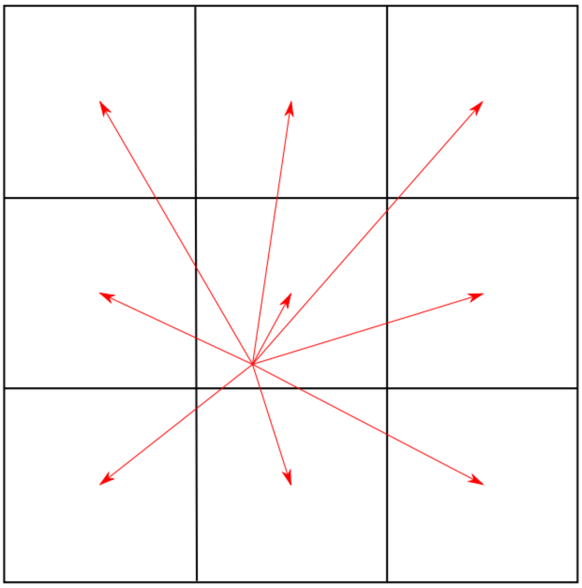

Figure 3.8.: Sketch of the distance measurement method. The black grid represents the pixels and the source point of the red arrows is the peak value of the Gaussian fit. The distances from the peak value to each pixel center are measured (red arrows), and saved. This is done over the whole region of interest.

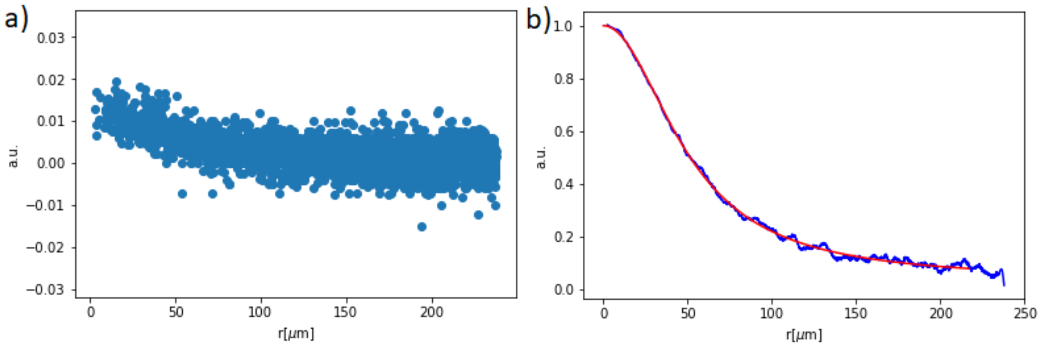

Figure 3.9.: a) Data points from the distance measurements. b) Smoothed curve (blue) from the data points of (a). Voigt profile fit (red) on the smoothed curve. Image (b) was taken from Mihaila *et al.* [1]

a varying amount of datapoints, i.e. 103μm for 8139 data points, although 99.9μm has a higher weight due to a higher number of data points. Thus, the FWHM of the Voigt profile is about $(100 \pm 4)\mu m$.

3.5. Alignment Procedure

The eventual alignment steps for each main component of the experiment are discussed in their respective chapter. This chapter describes the alignment procedure concerning the spatial and temporal overlap of electrons and light beam.

3.5.1. Triggering the Schottky Emitter

As mentioned in Chapter 3.2, a tungsten nano-tip is used as a Schottky electron gun, i.e. an electric potential is applied to the electron gun to lower the work function of electron emission. The work function is lowered to right above the emission threshold at the tip. A focused UV laser beam, polarized along the tip, is then used to overcome this threshold and generate a pulsed electron beam with low electron density, i.e. about 0.1 electrons per pulse.

Focusing the UV laser onto the nano-tip is a tedious task without a suitable alignment procedure. It is convenient to first heat the tip to over 1500K with an applied electric field, such that its black body radiation is in the visible light spectrum. Then, the visible light can be used to do back-alignment using two mirrors, i.e. from the nano-tip out to the laser beam path as defined by two irises. Thus, the UV should be aligned and hit the nano-tip, which can be further fine-tuned by directly looking at the intensity of the electron pulses.

3.5.2. Overlapping the Pulsed Electron and Laser Beam

To observe the phase modulation from free electron-light interactions, an overlap between the two pulses, both spatially and temporally, has to be achieved. Spatial overlap is comparatively easy to achieve and will be discussed later in this chapter. But since the inverse of the repetition rate of IR and electron pulse events is very high compared to the pulse duration, i.e. 1/R $\sim 1\mu s$ versus $\Delta t \sim 0.3ps$, it is rather cumbersome to achieve temporal overlap.

First, to get an estimation of the true overlapping scale, the Rayleigh length z_R is calculated and compared to the electron pulse duration. The Rayleigh length is the distance from focus at which the width of the Gaussian beam increases by $\sqrt{2}$. Within the Rayleigh length from the focus $A_z(\mathbf{r}, t) \approx 0$ holds in the paraxial approximation [38]. However, even above the Rayleigh length, the effects of the z-axis component of the vector field are small, further de-magnified by relativistic length contraction as seen in eq. 2.52. In the rest frame of the electron, the Rayleigh length is calculated via

$$z_R = \frac{\pi w_{00}'^2}{\lambda_L'} \, , \tag{3.2}$$

where w_{00}' is the beam waist in the electron rest frame, which is the same as in the lab frame due to its perpendicularity to the direction of propagation, i.e. $w_{00}' = w_{00} = 3.65\mu m$ for $7.3\mu m$ $1/e^2$-width. The wavelength λ_L' is the electron rest frame laser wavelength, which is acquired by Doppler shifting the laboratory wavelength via $\lambda_L' = \lambda_L \sqrt{(1 \pm \beta)/(1 \mp \beta)}$, with $\lambda_L = 1035nm$ and $\beta = 0.33$. Thus, the electron rest frame wavelength is 736nm.

Combining electron rest frame wavelength and the beam waist, the Rayleigh length is calculated to be $z_R = 56.9\mu m$. The electron pulse length is below 500fs [69] or 50μm. This is well within double the Rayleigh length, ensuring the whole electron pulse interacts with the laser pulse focus. Thus, phase modulation effects should be observable, and a delay stage step size of 666fs is enough to make sure that temporal overlap is not missed.

Such a small step size, however, would demand an incredible amount of different delay stage settings and is not feasible at all. First, because of the time it would take for data acquisition and second, because the deflection of electrons requires a high laser pulse energy, which might damage optical elements over such a long period of time.

Usually, the use of electron energy filters is the most common method to find spatial and temporal overlap [80], however, for this experiment, a multi-step process [1] is implemented consisting of three steps:

The first step is to use the scintillator to gain spatial overlap, as well as a good estimate for the temporal overlap. In this experiment, a plastic scintillator (BC-408) with a short rise time of 0.9ns and a radiation wavelength of 425nm is used. The plastic scintillator is placed on a small mechanical stage in the IP, as seen in Chapter 3.2. It is coated with a 5nm gold layer to avoid charging effects. Due to the low current in the pulsed electron setting, the damage to the scintillator is minimal. When an electron pulse hits the scintillator, the electrons excite the molecules in the scintillator. The excitation is followed by recombination, which leads to light emission in all directions. The CMOS that records the out-coupled laser light can also record the scintillated light after an electron pulse hits the scintillator. Thus, by first using the IR laser only, the exact location of the out-coupled IR is marked. Then the scintillator is used together with the electron beam, and the gun settings are changed, such that the scintillated light matches the location of the IR. This ensures spatial overlap between the IR and the electron beam in the IP.

To get a very rough estimate of the temporal overlap, the IR and electron path distances to the IP are measured with an ordinary measuring tape, which gives a timing mismatch of about 4ns.

For an improved estimate of the temporal overlap using the scintillator, the CMOS outside the SEM is replaced by a silicon photomultiplier (SiPM). The SiPM (Ketek, PM1125-WB PIN) is connected to an oscilloscope (Infiniium Keysight, MSOX3104T). To reach single photon sensitivity, an additional voltage amplifier (FEMTO HSA-Y) is connected to have a hundredfold signal enhancement. For the temporal overlap, the laser pulse trigger of the femtosecond laser is connected to the oscilloscope and used as a timing reference to the IR and the scintillated light. The scintillated light is thus recorded by the oscilloscope and the time difference from the maximum to the laser trigger is noted. Then the IR beam is recorded (100nJ pulse energy), and the delay stage is shifted such that the time difference between the IR pulse and the laser trigger is the same as the scintillated light and the laser trigger minus the rise time of the scintillator. This limits the timing mismatch to less than 200ps.

To further limit this mismatch, the scintillator is replaced by a copper grid with 10μm bar width. When hit by the focused laser beam (100nJ pulse energy), the copper produces a charged particle cloud in the immediate vicinity of the laser focus. This charged particle cloud has a rise time of about 7ps and a lifetime of over 30ps.

The copper grid is illuminated by a 100μm diameter electron pulse and detected by the MCP, such that the grid structure is clearly visible. If the cloud is present during the electron pulse, the electron beam image shows a clear deflection of electrons. By shifting the delay stage to the time when the electrons start to deflect, the timing mismatch can be limited to about 1ps. Furthermore, the copper grid is used to determine the electron beam width in the interaction region due to its well-known bar width.

After removing the copper grid and increasing the laser power (17.2μJ pulse energy), ponderomotive deflection is either already visible on the MCP, or a few steps away on the delay stage. Finally, after confirming ponderomotive deflection, the overlap is fine-tuned to the timing with the highest deflection intensity, as shown in fig. 3.10, achieving maximum temporal and spatial overlap. Assuming a Gaussian envelope over both pulses, the highest deflection intensity occurs when their centers are overlapping.

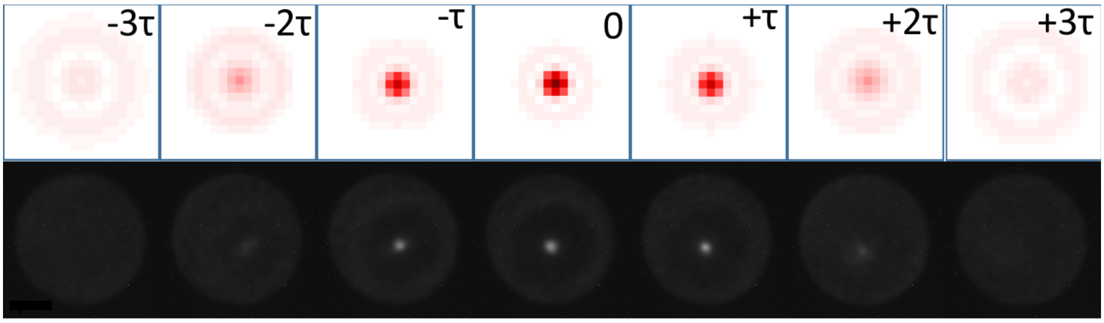

Figure 3.10.: Delay scan of ponderomotive deflection with a laser pulse energy of 6μJ and with a step size of $\tau = 666$fs. The upper row shows the used laser focus before getting de-magnified onto the interaction plane. The lower row shows the electron deflection as a result of the electron-photon interaction from the de-magnified upper-row laser focus spot. The highest deflection intensity is shown at zero τ. The image was taken and adapted from Mihaila *et al.*[1].

4. Results

The results obtained in this research are presented in the following chapter, where the theory as described in Chapter 2 is applied to understand the experiments conducted as part of this study. The experimental framework, as described in Chapter 3, facilitates the investigation of electron wave-front shaping via ponderomotive phase modulation in a modified scanning electron microscope (Chapter 3.2).

The theoretical phase modulation is derived in Chapter 2.5.2 via eq. 2.73. It can be rewritten in a more practical way with respect to experiments:

$$\varphi(x,y) = -\frac{\alpha}{2\pi(1+\beta)}\frac{E_L}{E_e}\frac{\lambda_L^2 I(x,y)}{\int \mathrm{d}x\mathrm{d}y I(x,y)} \tag{4.1}$$

The connection to classical mechanics, and thus to ray optics, is discussed in Chapter 2.5.3 via eq. 2.76. The classical momentum kick in the transverse plane is:

$$\Delta\mathbf{p}(x,y) = \hbar\nabla\varphi(x,y) \tag{4.2}$$

Figure 4.1 shows the experimental realization of phase modulation in comparison to wave optics and ray optics simulations. A laser pulse with a Gaussian intensity profile and a ring around it (fig. 4.1a) is ponderomotively interacting with a counter-propagating electron pulse. The interaction leads to phase modulation, or momentum kick, of the electron wave-front and, therefore, to a different electron intensity pattern (fig. 4.1b) measured by the microchannel plate (Chapter 3.4)

The laser focus spot in the interaction plane (IP) is set at the diffraction-limited minimum of 4.3μm FWHM and has a pulse energy of 6μJ. The electron beam diameter in the IP is set at 35μm, such that the ponderomotive interaction only occurs within the center of the electron pulse. The distance from the IP to the electron crossover is d_c = 5.9mm, with the IP above the crossover as sketched in fig. 3.1a. The electron acceleration energy is set at 30keV. Thus, considering the intensity pattern of the laser focus, the phase shift is up to 300π rad for the peak intensity.

Figures 4.1c and 4.1d demonstrate the results of wave optics simulations using eq. 4.1, as well as ray optics simulations, using eq. 4.2. Both simulations show good agreement with the experiment as well as with each other [1]. Note that this is in parts only the case, because of the limited spatial resolution of our detector (Chapter 3.4). The detector effectively averages over interference phenomena, that could not be explained in the ray optics picture [81].

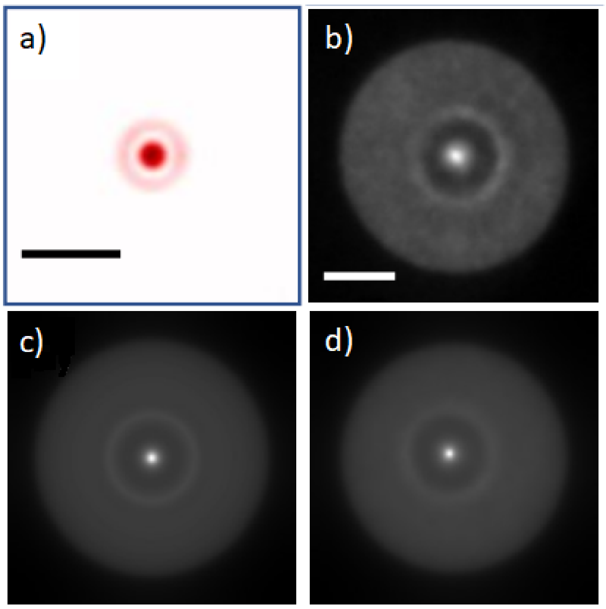

Figure 4.1.: a) Laser light intensity distribution before de-magnification (scalebar 93μm). The total laser pulse energy is 6μJ. b) Electron intensity distribution on the MCP after ponderomotive deflection by the laser in (a) (scalebar 1mm). c) Wave optics simulation of the ponderomotive deflection. A one-dimensional simulation is expanded assuming radial symmetry [81]. d) Ray optics simulation of the ponderomotive deflection. The images were taken and adapted from Mihaila *et al.* [1].

4.1. Creation of Ponderomotive Electron Lenses

As theoretically discussed in Chapter 2.7, the ability to modulate the transverse phase of an electron beam should enable both concave and convex ponderomotive electron lensing. The focus length of ponderomotive electron lenses, i.e. eq. 2.84 and 2.82, is

$$f_e = \pm\frac{(1+\beta)\pi^3}{2\alpha}\frac{E_e}{E_L}\frac{w^4}{\lambda_L^2\lambda_e}\ , \tag{4.3}$$

with positive and negative focus lengths for convex and concave lenses, respectively.

Figure 4.2 summarizes the necessary procedure for ponderomotive electron beam lensing. As discussed in Chapter 2.7, the laser intensity shapes used for concave and convex lenses are Gaussian (LG00) and Laguerre-Gaussian (LG10) modes, respectively, which are created by applying phase masks on the spatial light modulator (Chapter 3.3).

The top row of fig. 4.2 shows the mandatory phase masks to obtain the LG00 and LG10 modes. Figure 4.2a is the applied phase mask for diffraction around the hole in the gold mirror (Chapter 3.1) to prevent intensity loss. Figure 4.2b is the applied phase mask for aberration correction of the optical lenses. Thus, with the laser pulse initially having a LG00 intensity shape, fig 4.2a and 4.2b are applied to get a LG00 focus spot in the IP with a maximum peak intensity and minimum spot size . The LG00 mode has a measured $1/e^2$-width beam waist of $w_{00} = (3.65 \pm 18)\mu m$. Figure 4.2c shows the applied phase mask to create an LG10 mode [28], which is used together with fig. 4.2a and fig. 4.2b to get the respective LG10 mode in the IP. The LG10 mode has a measured $1/e^2$-width $w_{00} = (4.51 \pm 22)\mu m$.

The second row of fig. 4.2 shows the created laser light intensity patterns measured with a CMOS before getting de-magnified five times to the IP. Figure 4.2d is the LG00 mode with a laser pulse energy of 2.5μJ in the IP and fig. 4.2e is the LG10 mode with a laser pulse energy of 3.1μJ in the IP. Their respective horizontal intensity profiles are shown in the third row in fig. 4.2f and 4.2g. The negative and positive quadratic behavior of the intensities for eq. 4.3 are visible around the centres. Therefore, the electron beam crossover distance to the IP is set at around 241μm, such that the electron beam diameter in the IP is around 1.6μm.

The last row of fig. 4.2 shows the measured electron intensity distribution for an unaffected electron beam (fig. 4.2i) for an electron beam interaction with an LG00 mode (fig. 4.2h) and for an electron beam interacting with an LG10 mode (fig. 4.2j). Since the electron crossover occurs after the interaction, the concave lensing effect of the LG00 mode produces a smaller electron intensity area on the MCP than the unaffected beam. Similarly, the convex lensing effect of the LG10 mode produces a larger electron intensity area.

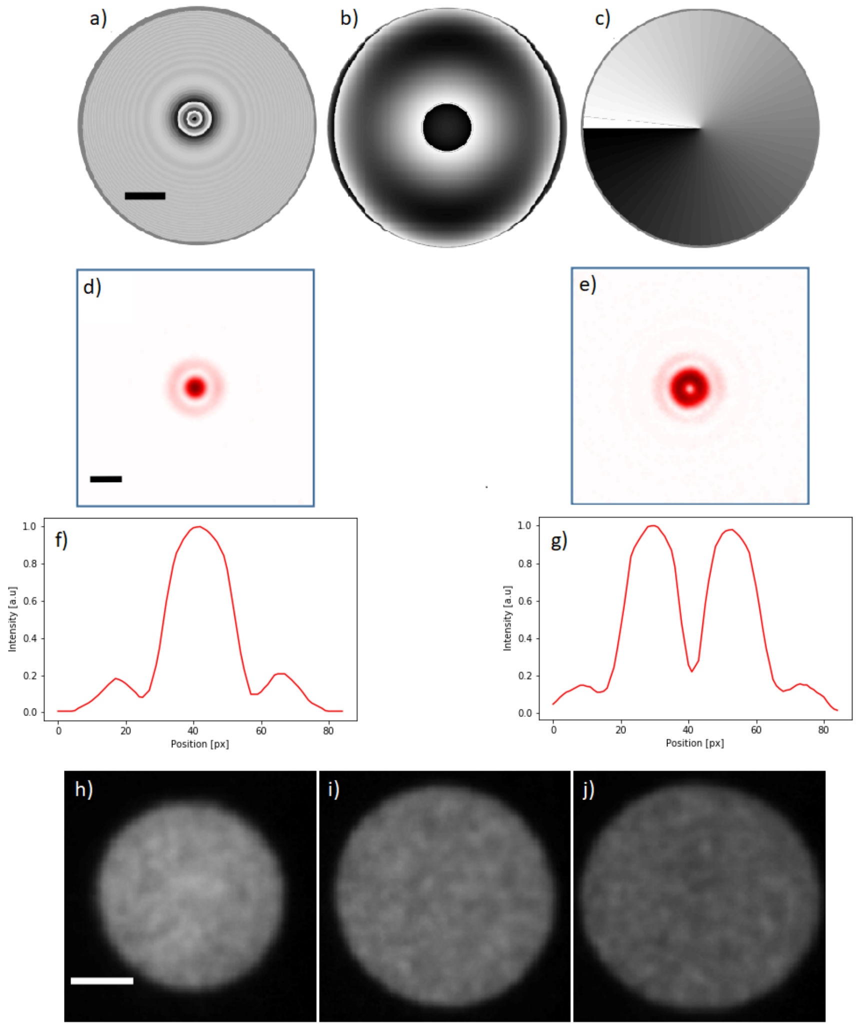

Figure 4.2.: First row (scalebar 1.9mm): Applied phase masks for a) imposing diffraction around the beam block, b) aberration correction of the optical system in front of the IP, and c) creation of an LG10 mode (right). Second row (scalebar 33μm): Measured laser intensities with a CMOS before getting de-magnified five times. d) Gaussian beam, created by implementing the diffraction phase mask (a) together with the aberration correction (b). e) LG10 mode, created by using all three phase masks from the top row. Third row: Respective intensity profiles from f) the Gaussian and g) the LG10 mode. Fourth row (scalebar 1mm): h) Concave lensing effect by the Gaussian beam. i) No ponderomotive lens implemented. j) Convex lensing effect with the LG10 mode. The electron focus takes place after the lensing for (i) and (j). The images have been taken and adapted from Mihaila *et al.* [1].

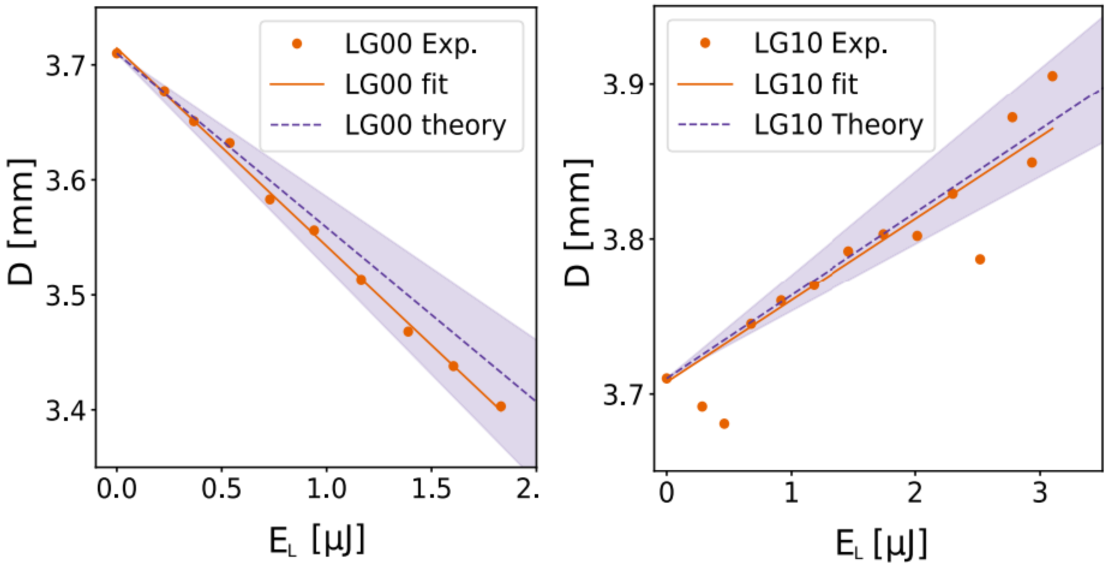

Figure 4.3.: Diameters of the electron beam on the MCP versus the laser pulse energy after interacting with the LG00 (left) and LG10 (right) laser modes. The dots (orange) represent the experimental data, the line (orange) is the fit to the data, and the dashed line (purple) is the theoretical relation between diameter and pulse energy. The shaded area illustrates the uncertainty region of the theoretical values due to the uncertainty of the beam waists. The images were taken and adapted from Mihaila *et al.* [1].

Figure 4.2(h-j) shows the electron beam's change of diameter D due to ponderomotive lenses with focus length f_e. Using eq. 4.3, the focal length can be used to calculate the expected diameter on the MCP via a wave optics or a ray optics model [1]. Furthermore, the MCP's electron diameters are determined by using Otsu's segmentation method in the image processing software Fiji [77] to get a segmented image. Then, fitting an ellipse to the image and using the geometric mean of the minor and major axis to get the radius of the electron beam.

The calculated diameters via wave optics model, together with the experimentally determined diameters are shown in fig. 4.3.

Verifying the accuracy of the ponderomotive lenses through the measured diameters on the MCP facilitates the determination of the experimental focus lengths with respect to the laser pulse energy $f_e(E_L)$. Since a good agreement between ray optics model and wave optics model has been shown [1], a simple ray optics approach, i.e. ABCD matrices, is used to determine the focus lengths:

$$\begin{pmatrix} R_{MCP} \\ \theta_{MCP} \end{pmatrix} = \begin{pmatrix} 1 & d \\ 0 & 1 \end{pmatrix} \begin{pmatrix} 1 & 0 \\ -\frac{1}{f_e} & 1 \end{pmatrix} \begin{pmatrix} R_0 \\ \theta_0 \end{pmatrix} \tag{4.4}$$

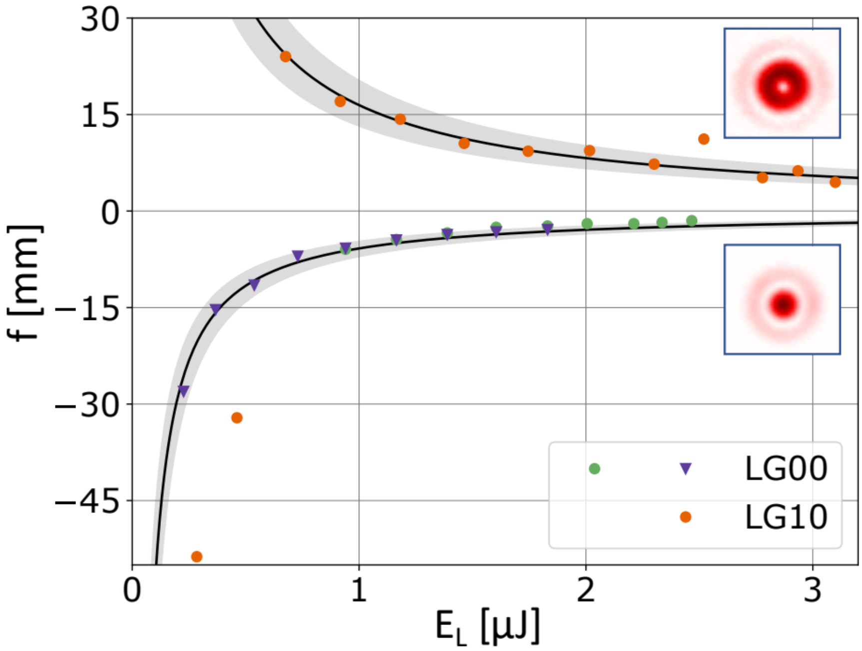

Figure 4.4.: Focus length as a function of the laser pulse energy for LG00 and LG10 laser modes. The modes are also shown in the inlets. The dots represent the experimental data while the line represents the theoretical values, with the grey shaded area as the uncertainty region due to the beam waist uncertainty. The image was taken and adapted from Mihaila *et al.* [1].

Here, $R_{MCP} = D/2$ is the beam radius on the MCP, θ_{MCP} is the respective convergence angle, $d = 550$mm is the distance between MCP and ponderomotive lens, $R_0 \approx 0.8\mu$m is the initial electron beam radius affected by the lens and θ_0 its respective convergence angle. The experimentally determined focus lengths are summarized in fig. 4.4 and most show good agreement with the theoretical values. However, when the observed radius R_{MCP} gets close to $R_0 + d\theta_0$, alignment becomes increasingly challenging, and a change of sign can occur due to misalignment as seen for two data points in fig. 4.4.

4.2. Programmable Arbitrary Electron Wave-Front Shaping

Equation 4.1 suggests that more complex shapes for the phase modulation of electron beams are possible if sufficient control over the intensity of the laser pulse wave-front in the IP is maintained. To test this, we use Zernike phase patterns as examples of programmable phase imprints. We program the SLM to display the Zernike polynomials related to trefoil, coma, and astigmatism, together with the necessary patterns for aberration correction (fig. 4.2b) and diffraction around the hole (fig. 4.2a). This leads to intensity patterns resembling aberrated focii, which are imprinted onto the electron wave. Free propagation

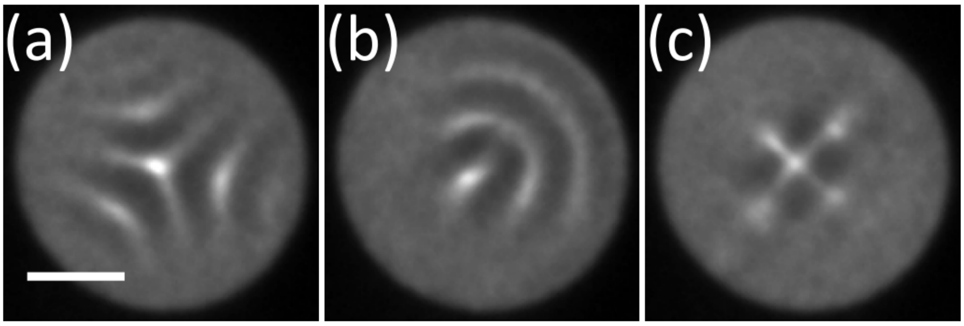

Figure 4.5.: Recorded electron intensities due to ponderomotive electron wave-front shaping. Trefoil (a), coma (b), and astigmatism (c) are imprinted onto the light wave-front via SLM. The resulting intensity pattern of the light causes an electron phase modulation. The presented images are the respective (a-c) electron intensity patterns (scalebar 1.1mm). The images were taken and adapted from Mihaila *et al.* [1].

then leads to the electron intensity distributions in fig. 4.5.

The laser pulse energy, as well as the electron crossover distance, are set at the same parameters as in Chapter 4 for the deflection measurement, i.e. $E_L = 6\mu$J and $d_c = 5.9$mm. The electron beam diameter is set at 48μm. Furthermore, considering the finite resolution of the laser focus spot in the IP, 10×10 pixels on the SLM are shaped for the chosen electron beam area.

As discussed in Chapter 3.3, a modified Gerchberg-Saxton (GSA) algorithm is used to shape the laser light intensity into arbitrary shapes. We use the GSA to create a phase mask (fig. 4.6a) that shapes the laser pulse intensity to look like a 'Smiley' (fig. 4.6)b. The 'Smiley' is imprinted onto the electron wave-front via eq. 4.1 and is then visible in the electron intensity distribution (fig. 4.6c). Thus, programmable arbitrary electron wave-front shaping is made possible via a ponderomotive phase modulation.

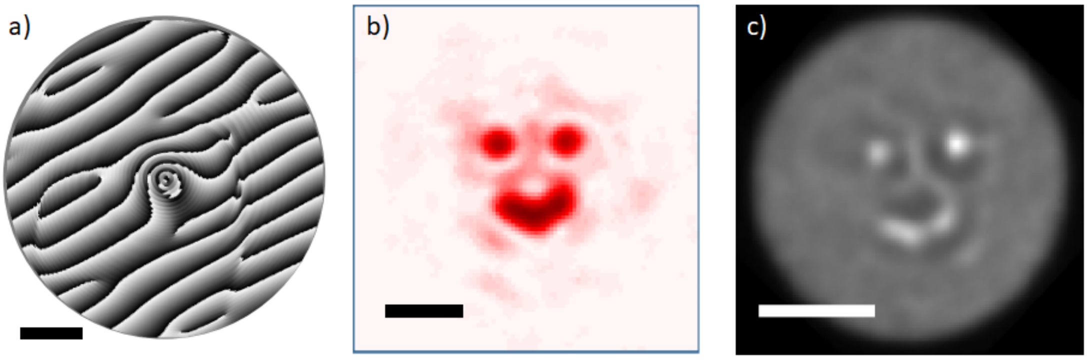

Figure 4.6.: a) SLM phase mask for a 'Smiley' phase pattern (scalebar 2.1mm). b) Laser focus intensity pattern of the created 'Smiley' before getting de-magnified (scalebar 70μm). Corresponding electron intensity pattern with the 'Smiley' incorporated through ponderomotive effects (scalebar 1.2mm). The images were taken and adapted from Mihaila *et al.* [1].

5. Discussion

Our results demonstrate that programmable, almost arbitrary electron wave-front shaping is experimentally achievable via phase modulation caused by ponderomotive interaction between counter-propagating electron and laser pulses [1]. This phase modulation is effectively represented by a scattering phase imposed onto the electron beam by the light field (Chapter 2.5.2). The primary limitations in the experiments are set by the SLM (Chapter 3.3.1), the laser pulse path from SLM to the interaction plane (Chapter 3.1), and the algorithm generating the phase masks for the desired light intensity patterns (Chapter 3.3.2).

Therefore, better control over the transverse electron beam phase can be achieved by having a more accurate understanding of the required phases implemented on the SLM. A possible next step would use machine learning algorithms [82] to enhance these experiments. Machine learning algorithms could be especially useful to get smooth phase masks. This could avoid unwanted interference between pixels. Additionally, the size of the hole in the mirror, which guides the laser beam to travel parallel to the electron beam, can be minimized, making it easier to diffract around it.

Phase modulation through ponderomotive interaction offers a distinct advantage in electron wave-front shaping as it is a loss-free process. This is a critical benefit, given the low electron signal in pulsed TEMs, which is less than one electron per pulse.

In addition, the experiments revealed the capability of producing both convex and concave lensing with focus lengths as small as 1.6mm (Chapter 4.3). It is worth mentioning that standard electron lenses cannot produce concave lensing, which makes this result especially significant.

The electron beam diameter in the IP is set up to 50μm, which provides for around 100 addressable pixels. Modern TEMs typically offer full coherence within this diameter, and spherical aberration correction also requires a similar number of addressable pixels [17]. However, experiments showed that spherical aberration correction can be achieved using a phase plate even with an electron beam diameter of 150μm [13]. To achieve ponderomotive phase modulation of up to 2π for a similar diameter, a laser pulse energy of approximately $11\mu J$ would be needed. This level of laser pulse energy is achievable within the setup (Chapter 3.1) and would result in around 950 addressable pixels [1].

Typically, TEMs use electron energies higher than the 30keV used in this study, which would result in a smaller phase shift. However, the experiment was operated in a high laser power regime. Only about 0.6nJ/μm^2 for 30keV and about 1.2nJ/μm^2 for 300keV are necessary to achieve a 2π phase shift. Thus, even electron wave-front shaping of 300keV electrons would be feasible with a similar laser. Furthermore, the resolution in the phase modulation can be improved by using shorter wavelengths.

6. Outlook and Conclusion

Compared to common electron optical setups, electron wave-front shaping with parallel-propagating light has several important advantages as it avoids inelastic scattering processes leading to extremely low electron loss. It further avoids, in comparison to solid structures, sub-aperture diffraction, charging effects, and decoherence.

The following paragraphs in Chapter 6.1 present ideas of applications that could be implemented using ponderomotive phase modulation.

6.1. Outlook

Phase Plates

Many samples in transmission electron microscopy couple extremely weakly to the incident electron beam. Imaging such samples shows almost no amplitude contrast, although the electron wave still acquires a position-dependent phase modulation from the specimen [83]. Similar to optical microscopy, i.e. Zernike phase contrast microscopy [84], the phase of the scattered part of the electron wave packet has to be shifted by $\pi/2$ with respect to the unscattered part in order to achieve maximum contrast. The optical or electron-optical element performing this phase shift is called a phase plate or Zernike phase plate.

There is a vast variety of different designs for electron wave phase plates that all have their respective advantages and disadvantages. An especially powerful phase plate is provided by arrays of electrostatic phase shifting cylindrical electrodes [17].

An electron-optical phase plate consisting of a laser light field as originally proposed by Müller *et al.* provides a way of performing loss-free phase shifts [26]. However, this phase plate is restricted to a single mode due to the cavity setting. While this provides a highly efficient phase plate for thin samples [85], thicker samples require more complex phase plates [86].

Consequently, being able to induce ultra-fast, spatially almost arbitrary phase shifts provides additional flexibility for phase contrast electron microscopy [1].

Aberration correction

Aberration correction is one of the most important challenges of electron microscopy and many different techniques were developed over the years. The types of aberrations are vast, i.e. astigmatism, chromatic aberration and, arguably the most important one to consider, spherical aberration.

Spherical aberration is an intrinsic problem of round electron lenses [33]. Early on, proposals for different geometries of electron lenses were made [87] in order to circumvent the problem. Experimentally, spherical aberration correction was finally realized by Haider *et al.* [45] and Krivanek *et al.* [88] by using non-rotationally symmetric multipole correctors, which was a kick-starter for numerous scientific discoveries [89].

But the research of aberration correction with a multitude of different techniques never stopped, as multipole correctors are costly to manufacture and are not easily implementable in an electron microscope, more often than not needing a new electron microscope altogether.

Spherical aberration is caused by the phase imprint that the electron beam acquires through the electron microscope column, i.e. the probe-forming electron lenses and apertures. This phase imprint χ can be written as a function of the electron beam radius in the transverse plane R and has the form:

$$\chi(R) = \frac{\pi}{2\lambda_e f_e^4}\left(C_s R^4 - 2\Delta f R^2\right) \tag{6.1}$$

The parameters C_s and Δf, which are determining the scaling of the spherical aberration, are the spherical aberration coefficient and the defocus respectively. The defocus, a length parameter on the z-axis determining the distance from the theoretical focus point, can be chosen, while the spherical aberration coefficient is determined by the electron microscope column. The radius $R = \sqrt{x^2 + y^2}$ is the radius in the transverse plane.

Thus, a phase modulation with light could correct for the spherical aberration phase modulation by simply setting $\chi(R) = -\varphi(R)$ [28], with the interaction plane in the same plane as the electron lens in question. The restriction of the interaction plane, however, is ultimately not necessary as long as the spherical aberration induced phase is known at any given point on the propagation axis. Furthermore, the arbitrariness of the defocus gives one more degree of freedom when trying to match the phase modulations. However, further studies of experimental implementations of light-based aberration correctors are necessary to examine their capabilities, especially with regard to the achievable noise levels [1], compared to current aberration correctors in electron microscopes [90].

The principle of spherical aberration correction with light is applicable for other aberrations as well [91], as they can be described by a phase modulation on the electron beam, making electron wave-front shaping with light a feasible and flexible tool for aberration correction in general.

Electron Vortex Sorter

Electron vortex sorters are tools to measure the spectrum of orbital angular momentum modes in electron beams [13] similar to the sorting principle in light optics [92]. There, different orbital angular momentum modes in a beam are separated by implementing a transformation from polar to Cartesian coordinates, such that the modes can be measured by spatially separated lines.

In light optics, two distinctively prepared lenses are used to perform the necessary beam transformations for the sorting mechanisms. Subsequently, a light field could be used for electron beams simulating the necessary electron lenses.

In other electron beam shaping experiments, electron vortex sorters were already experimentally achieved using electrodes [93], and further experiments using thin films were proposed by [94].

Wien Filter

An electron beam traversing a parallel-propagating light field has a lower group velocity within the light field (Chapter 2.4.1). Considering a light field with a uniform intensity, the electron pulse gets spatially shifted against the direction of propagation compared to a non-interacting electron pulse. This can be used in electron interferometry experiments to shift electron pulses against each other by tuning the light field's power. In similar experiments, such a longitudinal correction for electron beam paths in electron interferometry is shown with a Wien filter [62].

Multi-lens setup

It has been demonstrated that ponderomotive phase modulation offers a means of electron lensing. This holds promising potential for future applications, even to the extent of creating entire electron optical systems made up of ponderomotive electron lenses [1].

Exotic Beams

The creation of exotic beams can be achieved by applying specific phase modulations to an electron beam. Important examples are electron Airy [46], and Bessel [47] beams.

Airy beams, theoretically predicted by Berry and Balazs [95] and experimentally realized with light by Siviloglou *et al.* [96], are self-healing beams. This implies that they reconstruct their intensity profiles in the far-field after partially being blocked. They also have the interesting property of self-acceleration, which implies that the highest intensity of the transverse Airy function shape of the beam traverses around a parabolic trajectory while the center of mass propagates in a straight line. Airy beams in light optics are usually generated by modulating the phase of the light.

Voloch-Bloch *et al.* [46] experimentally realized the generation of electron Airy beams by performing a cubic phase modulation onto an electron beam using a nano-scale hologram. Following this idea, cubic phase modulations of electron beams could also be realized through ponderomotive forces.

Similar to Airy beams, Bessel beams are self-healing and further provide a basis for other self-healing beam shapes [97]. Additionally, a Bessel beam of zeroth order provides the smallest central spot size in comparison to other common beam shapes [98].

Following light optics implementation again, Grillo *et al.* [47] showed the generation of electron Bessel beams by performing a conical phase modulation using a nano-fabricated kinoform. Again, parallel-propagating free electron-light interaction could provide the necessary phase modulations for generating Bessel beams. Electron Bessel beams are of particular interest in electron tomography [99].

6.2. Conclusion

Electron wave-front shaping using ponderomotive phase modulation could offer a wide range of applications as detailed in Chapter 6.1. Most of these applications are already in use via different phase modulation mechanisms and are often specific to one research goal. Utilizing programmable ponderomotive electron wave-front shaping, multiple applications can be accomplished using just one setup due to its versatility. This is made possible by the highly flexible SLM.

A crucial consideration is that the various tools used for electron microscopy research generally do not prevent the possibility of incorporating an additional light-field setup. This opens up the possibility of combining conventional electron microscope setups with ponderomotive phase modulation.

Bibliography

[1] Marius Constantin Chirita Mihaila, Philipp Weber, Matthias Schneller, Lucas Grandits, Stefan Nimmrichter, and Thomas Juffmann. Transverse electron-beam shaping with light. *Phys. Rev. X*, 12:031043, Sep 2022.

[2] Louis De Broglie. *Recherches sur la théorie des quanta*. PhD thesis, Migration-université en cours d'affectation, 1924.

[3] C. Davisson and L. H. Germer. The scattering of electrons by a single crystal of nickel. *Nature*, 119:558–560, 1927.

[4] Max Knoll and Ernst Ruska. Das elektronenmikroskop. *Zeitschrift für physik*, 78(5):318–339, 1932.

[5] Rachel Courtland. The microscope revolution that's sweeping through materials science. *Nature*, 563(7732):462–464, 2018.

[6] Eva Nogales. The development of cryo-em into a mainstream structural biology technique. *Nature methods*, 13(1):24–27, 2016.

[7] Harald H Rose. Historical aspects of aberration correction. *Journal of electron microscopy*, 58(3):77–85, 2009.

[8] M Haider, P Hartel, H Müller, S Uhlemann, and J Zach. Current and future aberration correctors for the improvement of resolution in electron microscopy. *Philosophical Transactions of the Royal Society A: Mathematical, Physical and Engineering Sciences*, 367(1903):3665–3682, 2009.

[9] Halina Rubinsztein-Dunlop, Andrew Forbes, Michael V Berry, Mark R Dennis, David L Andrews, Masud Mansuripur, Cornelia Denz, Christina Alpmann, Peter Banzer, Thomas Bauer, et al. Roadmap on structured light. *Journal of Optics*, 19(1):013001, 2016.

[10] Philipp Michael Pelz, Wen Xuan Qiu, Robert Bücker, Günther Kassier, and RJ Miller. Low-dose cryo electron ptychography via non-convex bayesian optimization. *Scientific Reports*, 7(1):1–13, 2017.

[11] Hiroshi Okamoto, Tatiana Latychevskaia, and Hans-Werner Fink. A quantum mechanical scheme to reduce radiation damage in electron microscopy. *Applied physics letters*, 88(16):164103, 2006.

[12] Thomas Juffmann, Andrés de los Ríos Sommer, and Sylvain Gigan. Local optimization of wave-fronts for optimal sensitivity phase imaging (lowphi). *Optics Communications*, 454:124484, 2020.

[13] Dolev Roitman, Roy Shiloh, Peng-Han Lu, Rafal E Dunin-Borkowski, and Ady Arie. Shaping of electron beams using sculpted thin films. *ACS photonics*, 8(12):3394–3405, 2021.

[14] Roy Shiloh, Roei Remez, Peng-Han Lu, Lei Jin, Yossi Lereah, Amir H Tavabi, Rafal E Dunin-Borkowski, and Ady Arie. Spherical aberration correction in a scanning transmission electron microscope using a sculpted thin film. *Ultramicroscopy*, 189:46–53, 2018.

[15] Benjamin J McMorran, Amit Agrawal, Ian M Anderson, Andrew A Herzing, Henri J Lezec, Jabez J McClelland, and John Unguris. Electron vortex beams with high quanta of orbital angular momentum. *science*, 331(6014):192–195, 2011.

[16] Amir H Tavabi, Marco Beleggia, Vadim Migunov, Alexey Savenko, Ozan Öktem, Rafal E Dunin-Borkowski, and Giulio Pozzi. Tunable ampere phase plate for low dose imaging of biomolecular complexes. *Scientific reports*, 8(1):1–5, 2018.

[17] Jo Verbeeck, Armand Béché, Knut Müller-Caspary, Giulio Guzzinati, Minh Anh Luong, and Martien Den Hertog. Demonstration of a 2× 2 programmable phase plate for electrons. *Ultramicroscopy*, 190:58–65, 2018.

[18] Giulio Guzzinati, Armand Béché, Hugo Lourenço-Martins, Jérôme Martin, Mathieu Kociak, and Jo Verbeeck. Probing the symmetry of the potential of localized surface plasmon resonances with phase-shaped electron beams. *Nature Communications*, 8(1):14999, 2017.

[19] Amir H Tavabi, Paolo Rosi, Enzo Rotunno, Alberto Roncaglia, Luca Belsito, Stefano Frabboni, Giulio Pozzi, Gian Carlo Gazzadi, Peng-Han Lu, Robert Nijland, et al. Experimental demonstration of an electrostatic orbital angular momentum sorter for electron beams. *Physical review letters*, 126(9):094802, 2021.

[20] Brett Barwick, David J Flannigan, and Ahmed H Zewail. Photon-induced near-field electron microscopy. *Nature*, 462(7275):902–906, 2009.

[21] Giovanni M Vanacore, I Madan, G Berruto, K Wang, E Pomarico, RJ Lamb, D McGrouther, I Kaminer, B Barwick, F Javier García de Abajo, et al. Attosecond coherent control of free-electron wave functions using semi-infinite light fields. *Nature communications*, 9(1):1–11, 2018.

[22] Nahid Talebi. Strong interaction of slow electrons with near-field light visited from first principles. *Physical Review Letters*, 125(8):080401, 2020.

[23] Christoph T Hebeisen, German Sciaini, Maher Harb, Ralph Ernstorfer, Thibault Dartigalongue, Sergei G Kruglik, and RJ Dwayne Miller. Grating enhanced ponderomotive scattering for visualization and full characterization of femtosecond electron pulses. *Optics express*, 16(5):3334–3341, 2008.

[24] Martin Kozák, Norbert Schönenberger, and Peter Hommelhoff. Ponderomotive generation and detection of attosecond free-electron pulse trains. *Physical review letters*, 120(10):103203, 2018.

[25] Martin Kozák, Timo Eckstein, Norbert Schönenberger, and Peter Hommelhoff. Inelastic ponderomotive scattering of electrons at a high-intensity optical travelling wave in vacuum. *Nature Physics*, 14(2):121–125, 2018.

[26] Osip Schwartz, Sara L. Axelrod, Jeremy J.and Campbell, Carter Turnbaugh, Robert M. Glaeser, and Holger Müller. Laser phase plate for transmission electron microscopy. *Nature Methods*, 16, oct 2019.

[27] F. J. García de Abajo. Optical excitations in electron microscopy. *Rev. Mod. Phys.*, 82:209–275, Feb 2010.

[28] F. Javier García de Abajo and Andrea Konečná. Optical modulation of electron beams in free space. *Phys. Rev. Lett.*, 126:123901, Mar 2021.

[29] P. D. Nellist, M. F. Chisholm, N. Dellby, O. L. Krivanek, M. F. Murfitt, Z. S. Szilagyi, A. R. Lupini, A. Borisevich, W. H. Sides, and S. J. Pennycook. Direct sub-angstrom imaging of a crystal lattice. *Science*, 305(5691):1741–1741, 2004.

[30] Ondrej L Krivanek, Tracy C Lovejoy, Niklas Dellby, Toshihiro Aoki, R W Carpenter, Peter Rez, Emmanuel Soignard, Jiangtao Zhu, Philip E Batson, Maureen J Lagos, Ray F Egerton, and Peter A Crozier. Vibrational spectroscopy in the electron microscope. *Nature*, 514(7521):209–212, October 2014.

[31] Christopher Bäuerle, D Christian Glattli, Tristan Meunier, Fabien Portier, Patrice Roche, Preden Roulleau, Shintaro Takada, and Xavier Waintal. Coherent control of single electrons: a review of current progress. *Reports on Progress in Physics*, 81(5):056503, apr 2018.

[32] Mike L Jenkins and Mark A Kirk. *Characterisation of radiation damage by transmission electron microscopy.* CRC Press, 2000.

[33] O_ Scherzer. Über einige fehler von elektronenlinsen. *Zeitschrift für Physik*, 101(9):593–603, 1936.

[34] A Howie. Photon interactions for electron microscopy applications. *The European Physical Journal-Applied Physics*, 54(3):33502, 2011.

[35] AK Singh and S Chandra. Electron acceleration by ponderomotive force in magnetized quantum plasma. *Laser and Particle Beams*, 35(2):252–258, 2017.

[36] Brian WJ McNeil and Neil R Thompson. X-ray free-electron lasers. *Nature photonics*, 4(12):814–821, 2010.

[37] T. H. Maiman. Stimulated Optical Radiation in Ruby. *Nature*, 187(4736):493–494, August 1960.

[38] Hans-A Bachor and Timothy C Ralph. *A guide to experiments in quantum optics*. John Wiley & Sons, 2019.

[39] Martin J Booth. Adaptive optical microscopy: the ongoing quest for a perfect image. *Light: Science & Applications*, 3(4):e165–e165, 2014.

[40] Pere Clemente, Vicente Durán, Enrique Tajahuerce, Jesús Lancis, et al. Optical encryption based on computational ghost imaging. *Optics letters*, 35(14):2391–2393, 2010.

[41] Reza Nasiri Mahalati, Ruo Yu Gu, and Joseph M Kahn. Resolution limits for imaging through multi-mode fiber. *Optics express*, 21(2):1656–1668, 2013.

[42] Libor Mrňa, Martin Šarbort, Šimon Řeřucha, and Petr Jedlička. Adaptive optics for control of the laser welding process. In *EPJ Web of Conferences*, volume 48, page 00017. EDP Sciences, 2013.

[43] Paul J Campagnola and Leslie M Loew. Second-harmonic imaging microscopy for visualizing biomolecular arrays in cells, tissues and organisms. *Nature biotechnology*, 21(11):1356–1360, 2003.

[44] Stefan W Hell and Jan Wichmann. Breaking the diffraction resolution limit by stimulated emission: stimulated-emission-depletion fluorescence microscopy. *Optics letters*, 19(11):780–782, 1994.

[45] Max Haider, Harald Rose, Stephan Uhlemann, Eugen Schwan, Bernd Kabius, and Knut Urban. A spherical-aberration-corrected 200 kv transmission electron microscope. *Ultramicroscopy*, 75(1):53–60, 1998.

[46] Noa Voloch-Bloch, Yossi Lereah, Yigal Lilach, Avraham Gover, and Ady Arie. Generation of electron airy beams. *Nature*, 494(7437):331–335, 2013.

[47] Vincenzo Grillo, Ebrahim Karimi, Gian Carlo Gazzadi, Stefano Frabboni, Mark R Dennis, and Robert W Boyd. Generation of nondiffracting electron bessel beams. *Physical Review X*, 4(1):011013, 2014.

[48] Tyler R Harvey, Jordan S Pierce, Amit K Agrawal, Peter Ercius, Martin Linck, and Benjamin J McMorran. Efficient diffractive phase optics for electrons. *New Journal of Physics*, 16(9):093039, 2014.

[49] Maryam Khoshouei, Mazdak Radjainia, Wolfgang Baumeister, and Radostin Danev. Cryo-em structure of haemoglobin at 3.2 å determined with the volta phase plate. *Nature communications*, 8(1):1–6, 2017.

[50] Andrea Konečná and F Javier García de Abajo. Electron beam aberration correction using optical near fields. *Physical Review Letters*, 125(3):030801, 2020.

[51] H. Batelaan. Colloquium: Illuminating the kapitza-dirac effect with electron matter optics. *Rev. Mod. Phys.*, 79:929–941, Jul 2007.

[52] P. L. Kapitza and P. A. M. Dirac. The reflection of electrons from standing light waves. *Mathematical Proceedings of the Cambridge Philosophical Society*, 29(2):297–300, 1933.

[53] P. H. Bucksbaum, D. W. Schumacher, and M. Bashkansky. High-intensity kapitza-dirac effect. *Phys. Rev. Lett.*, 61:1182–1185, Sep 1988.

[54] Phillip L. Gould, George A. Ruff, and David E. Pritchard. Diffraction of atoms by light: The near-resonant kapitza-dirac effect. *Phys. Rev. Lett.*, 56:827–830, Feb 1986.

[55] Daniel L. Freimund, Kayvan Aflatooni, and Herman Batelaan. Observation of the kapitza–dirac effect. *Nature*, 413:142–143, 2001.

[56] Jeremy J. Axelrod, Sara L. Campbell, Osip Schwartz, Carter Turnbaugh, Robert M. Glaeser, and Holger Müller. Observation of the relativistic reversal of the ponderomotive potential. *Phys. Rev. Lett.*, 124:174801, May 2020.

[57] Peter W Hawkes and Erwin Kasper. *Principles of electron optics: Wave Optics*, volume 3. Academic press, 1996.

[58] L. Reimer and H. Kohl. *Transmission Electron Microscopy.* Springer Series in Optical Sciences, 5th edition, 2008.

[59] Ding-Shyue Yang, Omar F Mohammed, and Ahmed H Zewail. Scanning ultrafast electron microscopy. *Proceedings of the National Academy of Sciences*, 107(34):14993–14998, 2010.

[60] Justin Peatross and Michael Ware. Physics of light and optics: a free online textbook. In *Frontiers in Optics*, page JWA64. Optical Society of America, 2010.

[61] A. Messiah. *Quantum Mechanics.* Dover Publications, 1966.

[62] Marc Nicklaus and Franz Hasselbach. Wien filter: A wave-packet-shifting device for restoring longitudinal coherence in charged-matter-wave interferometers. *Phys. Rev. A*, 48:152–160, Jul 1993.

[63] Max Born and Emil Wolf. *Principles of optics: electromagnetic theory of propagation, interference and diffraction of light.* Elsevier, 2013.

[64] Yuuki Uesugi, Yuichi Kozawa, and Shunichi Sato. Electron round lenses with negative spherical aberration by a tightly focused cylindrically polarized light beam. *Physical Review Applied*, 16(1):L011002, 2021.

[65] Ajanta Barh, Peter John Rodrigo, Lichun Meng, Christian Pedersen, and Peter Tidemand-Lichtenberg. Parametric upconversion imaging and its applications. *Advances in Optics and Photonics*, 11(4):952–1019, 2019.

[66] L. Reimer. *Scanning Electron Microscopy.* Springer Series in Optical Sciences, 2th edition, 1998.

[67] Peter Hommelhoff, Yvan Sortais, Anoush Aghajani-Talesh, and Mark A Kasevich. Field emission tip as a nanometer source of free electron femtosecond pulses. *Physical review letters*, 96(7):077401, 2006.

[68] Johannes Hoffrogge, Jan Paul Stein, Michael Krüger, Michael Förster, Jakob Hammer, Dominik Ehberger, Peter Baum, and Peter Hommelhoff. Tip-based source of femtosecond electron pulses at 30 kev. *Journal of Applied Physics*, 115(9):094506, 2014.

[69] M Kozák, J McNeur, N Schönenberger, J Illmer, A Li, A Tafel, P Yousefi, T Eckstein, and P Hommelhoff. Ultrafast scanning electron microscope applied for studying the interaction between free electrons and optical near-fields of periodic nanostructures. *Journal of Applied Physics*, 124(2):023104, 2018.

[70] A Muller and John Grazul. Optimizing the environment for sub-0.2 nm scanning transmission electron microscopy. *Journal of electron microscopy*, 50(3):219–226, 2001.

[71] Rujia Li and Liangcai Cao. Progress in phase calibration for liquid crystal spatial light modulators. *Applied Sciences*, 9(10):2012, 2019.

[72] Ralph W Gerchberg. A practical algorithm for the determination of plane from image and diffraction pictures. *Optik*, 35(2):237–246, 1972.

[73] Tomoyoshi Shimobaba, Takashi Kakue, Yutaka Endo, Ryuji Hirayama, Daisuke Hiyama, Satoki Hasegawa, Yuki Nagahama, Marie Sano, Minoru Oikawa, Takashige Sugie, et al. Improvement of the image quality of random phase-free holography using an iterative method. *Optics Communications*, 355:596–601, 2015.

[74] Vasudevan Lakshminarayanan and Andre Fleck. Zernike polynomials: a guide. *Journal of Modern Optics*, 58(7):545–561, 2011.

[75] Joseph Ladislas Wiza et al. Microchannel plate detectors. *Nucl. Instrum. Methods*, 162(1-3):587–601, 1979.

[76] Till Cremer, Bernhard W Adams, Melvin Aviles, Camden D Ertley, Michael R Foley, Alexey Lyashenko, Michael J Minot, Mark A Popecki, Travis Rivera, Michael E Stochaj, et al. Recent developments in next-generation microchannel plates for particle identification applications. *UV, X-Ray, and Gamma-Ray Space Instrumentation for Astronomy XXI*, 11118:169–183, 2019.

[77] Johannes Schindelin, Ignacio Arganda-Carreras, Erwin Frise, Verena Kaynig, Mark Longair, Tobias Pietzsch, Stephan Preibisch, Curtis Rueden, Stephan Saalfeld, Benjamin Schmid, et al. Fiji: an open-source platform for biological-image analysis. *Nature methods*, 9(7):676–682, 2012.

[78] Wes McKinney. *Python for data analysis: Data wrangling with Pandas, NumPy, and IPython.* " O'Reilly Media, Inc.", 2012.

[79] Abraham Savitzky and Marcel JE Golay. Smoothing and differentiation of data by simplified least squares procedures. *Analytical chemistry*, 36(8):1627–1639, 1964.

[80] Sang Tae Park, Milo Lin, and Ahmed H Zewail. Photon-induced near-field electron microscopy (pinem): theoretical and experimental. *New Journal of Physics*, 12(12):123028, 2010.

[81] Matthias Schneller. Simulation of electron-light interactions, 2022.

[82] Steven R Spurgeon, Colin Ophus, Lewys Jones, Amanda Petford-Long, Sergei V Kalinin, Matthew J Olszta, Rafal E Dunin-Borkowski, Norman Salmon, Khalid Hattar, Wei-Chang D Yang, Renu Sharma, Yingge Du, Ann Chiaramonti, Haimei Zheng, Edgar C Buck, Libor Kovarik, R Lee Penn, Dongsheng Li, Xin Zhang, Mitsuhiro Murayama, and Mitra L Taheri. Towards data-driven next-generation transmission electron microscopy. *Nature Materials*, 20(3):274–279, March 2021.

[83] H Müller, Jian Jin, R Danev, J Spence, H Padmore, and R M Glaeser. Design of an electron microscope phase plate using a focused continuous-wave laser. *New Journal of Physics*, 12(7):073011, jul 2010.

[84] Frits Zernike. Phase contrast, a new method for the microscopic observation of transparent objects. *Physica*, 9(7):686–698, 1942.

[85] Dorian Bouchet, Jonathan Dong, Dante Maestre, and Thomas Juffmann. Fundamental bounds on the precision of classical phase microscopes. *Physical Review Applied*, 15(2):024047, 2021.

[86] Stewart A Koppell, Yonatan Israel, Adam J Bowman, Brannon B Klopfer, and Mark A Kasevich. Transmission electron microscopy at the quantum limit. *Applied Physics Letters*, 120(19):190502, 2022.

[87] O Scherzer. The theoretical resolution limit of the electron microscope. *Journal of Applied Physics*, 20(1):20–29, 1949.

[88] OL Krivanek, N Dellby, and AR Lupini. Towards sub-å electron beams. *Ultramicroscopy*, 78(1-4):1–11, 1999.

[89] Stephen J Pennycook. The impact of stem aberration correction on materials science. *Ultramicroscopy*, 180:22–33, 2017.

[90] Stephan Uhlemann, Heiko Müller, Peter Hartel, Joachim Zach, and Max Haider. Thermal magnetic field noise limits resolution in transmission electron microscopy. *Physical review letters*, 111(4):046101, 2013.

[91] Martin Linck, Peter Hartel, Stephan Uhlemann, Frank Kahl, Heiko Müller, Joachim Zach, Max Haider, Marcel Niestadt, Maarten Bischoff, Johannes Biskupek, et al. Chromatic aberration correction for atomic resolution tem imaging from 20 to 80 kv. *Physical review letters*, 117(7):076101, 2016.

[92] Gregorius CG Berkhout, Martin PJ Lavery, Johannes Courtial, Marco W Beijersbergen, and Miles J Padgett. Efficient sorting of orbital angular momentum states of light. *Physical review letters*, 105(15):153601, 2010.

[93] Benjamin J McMorran, Tyler R Harvey, and Martin PJ Lavery. Efficient sorting of free electron orbital angular momentum. *New Journal of Physics*, 19(2):023053, 2017.

[94] Vincenzo Grillo, Amir H Tavabi, Federico Venturi, Hugo Larocque, Roberto Balboni, Gian Carlo Gazzadi, Stefano Frabboni, Peng-Han Lu, Erfan Mafakheri, Frédéric Bouchard, et al. Measuring the orbital angular momentum spectrum of an electron beam. *Nature Communications*, 8(1):1–6, 2017.

[95] Michael V Berry and Nandor L Balazs. Nonspreading wave packets. *American Journal of Physics*, 47(3):264–267, 1979.

[96] GA Siviloglou, J Broky, Aristide Dogariu, and DN Christodoulides. Observation of accelerating airy beams. *Physical Review Letters*, 99(21):213901, 2007.

[97] Julio C Gutiérrez-Vega, MD Iturbe-Castillo, and S Chávez-Cerda. Alternative formulation for invariant optical fields: Mathieu beams. *Optics letters*, 25(20):1493–1495, 2000.

[98] David McGloin and Kishan Dholakia. Bessel beams: diffraction in a new light. *Contemporary physics*, 46(1):15–28, 2005.

[99] Paul A Midgley and Rafal E Dunin-Borkowski. Electron tomography and holography in materials science. *Nature materials*, 8(4):271–280, 2009.

A. Appendix

For the sake of simplicity of this text, if there is no sum sign within a calculation, i.e. $\sum$, Einstein sum convention is used for indices appearing twice.

The Levi-Civita symbol ϵ_{ijk} is defined by

$$\epsilon_{ijk} = \begin{cases} 1 & \text{if } (i,j,k) \text{ is even permutation} \\ -1 & \text{if } (i,j,k) \text{ is odd permutation} \\ 0 & \text{if } i=j,\ i=k,\ \text{or } j=k \end{cases} , \tag{A.1}$$

while the Dirac-Delta distribution is defined by

$$\delta_{ij} = \begin{cases} 1 & \text{if } i=j \\ 0 & \text{if } i \neq j \end{cases} \tag{A.2}$$

Furthermore, $\mathcal{I}_n$ denotes a unit matrix of order n.

A.1. Mathematical Properties of Pauli Matrices

The Pauli matrices σ_i are three 2x2 matrices of the form:

$$\sigma_1 = \begin{pmatrix} 0 & 1 \\ 1 & 0 \end{pmatrix} , \quad \sigma_2 = \begin{pmatrix} 0 & -i \\ i & 0 \end{pmatrix} , \quad \sigma_3 = \begin{pmatrix} 1 & 0 \\ 0 & -1 \end{pmatrix} \tag{A.3}$$

The vector operator $\vec{\sigma}$, therefore, describes a vector with three components, whereas the components are the three Pauli matrices. Naturally, a vector multiplication of this vector operator with a general vector $\mathbf{a}$ can be expressed as:

$$(\vec{\sigma}\mathbf{a}) = (\mathbf{a}\vec{\sigma}) = a_1\sigma_1 + a_2\sigma_2 + a_3\sigma_3 = \begin{pmatrix} a_3 & a_1 - ia_2 \\ a_1 + ia_2 & -a_3 \end{pmatrix} \tag{A.4}$$

Furthermore, the Pauli matrices satisfy the commutation relations:

$$\{\sigma_i, \sigma_j\} = 2\delta_{ij}\mathcal{I}_2 \tag{A.5}$$

$$[\sigma_i, \sigma_j] = 2i\epsilon_{ijk}\sigma_k \tag{A.6}$$

It is easily verified that the Pauli matrices are hermitian and satisfy the relations $\sigma_1^2 = \sigma_2^2 = \sigma_3^2 = \mathcal{I}_2$. The commutation relations, i.e. eq. A.5 and A.6, are enough to calculate the following Pauli matrices relations:

$$(\mathbf{a}\vec{\sigma})(\mathbf{b}\vec{\sigma}) = (\mathbf{ab})\mathcal{I}_2 + i(\mathbf{a} \times \mathbf{b})\mathcal{I}_2 \tag{A.7}$$

$$(\vec{\sigma}\mathbf{a})\sigma_i(\vec{\sigma}\mathbf{a}) = 2a_i(\mathbf{a}\vec{\sigma}) - \mathbf{a}^2\sigma_i \tag{A.8}$$

Equation A.7 can proven via

$$\begin{aligned}(\mathbf{a}\vec{\sigma})(\mathbf{b}\vec{\sigma}) = a_i b_j \sigma_i \sigma_j = a_i b_j(2i\epsilon_{ijk}\sigma_k + \sigma_j\sigma_i) &= a_i b_j(2i\epsilon_{ijk}\sigma_k + 2\delta_{ji}\mathcal{I}_2 - \sigma_i\sigma_j)\\ \implies 2a_i b_j \sigma_i \sigma_j &= 2a_i b_i \mathcal{I}_2 + 2i\epsilon_{ijk} a_i b_j \sigma_k\\ \implies (\mathbf{a}\vec{\sigma})(\mathbf{b}\vec{\sigma}) &= (\mathbf{ab})\mathcal{I}_2 + i(\mathbf{a}\times\mathbf{b})\mathcal{I}_2 \ ,\end{aligned}$$

and equation A.8 via

$$\begin{gathered}(\vec{\sigma}\mathbf{a})\sigma_i(\vec{\sigma}\mathbf{a})\\ = a_j a_n \sigma_j \sigma_i \sigma_n\\ = a_j a_n(\delta_{ji}\mathcal{I}_2 + i\epsilon_{jik}\sigma_k)\sigma_n\\ = a_i a_n \sigma_n + i a_j a_n \epsilon_{jik}(\delta_{kn} + i\epsilon_{knl}\sigma_l)\\ a_i a_n \sigma_n + i\epsilon_{jin} a_j a_n - a_j a_n(\delta_{jn}\delta_{il} - \delta_{jl}\delta_{in})\sigma_l\\ = a_i a_n \sigma_n - i\epsilon_{ijn} a_j a_n \mathcal{I}_2 - a_n a_n \sigma_i + a_i a_n \sigma_n\\ = 2a_i(\mathbf{a}\vec{\sigma}) - i(\mathbf{a}\times\mathbf{a})_i\mathcal{I}_2 - \mathbf{a}^2\sigma_i\\ = 2a_i(\mathbf{a}\vec{\sigma}) - \mathbf{a}^2\sigma_i\end{gathered}$$

A.2. Derivation of the Plane Wave 4-Component Spinor

The Dirac equation for a free electron is

$$[m_e c^2\beta + c\hbar\vec{\alpha}\mathbf{k}]\Psi(\mathbf{r},t) = i\hbar\partial_t\Psi(\mathbf{r},t) \ , \tag{A.9}$$

with the matrices

$$\beta = \begin{pmatrix}\mathcal{I}_2 & 0\\ 0 & -\mathcal{I}_2\end{pmatrix}, \quad \vec{\alpha} = \begin{pmatrix}0 & \vec{\sigma}\\ \vec{\sigma} & 0\end{pmatrix} \ . \tag{A.10}$$

The plane wave solution for the 4-component spinor wave function reads in general as:

$$\Psi^{\pm}(\mathbf{r},t) = \Psi^{\pm}_{\mathbf{k}j} e^{i(\mathbf{kr}\mp E_{\mathbf{k}}t/\hbar)} \ , \tag{A.11}$$

with the 4-component spinor amplitude $\Psi^{\pm}_{\mathbf{k}j}$ usually being split up into two 2-component spinors $\chi_{\mathbf{k}j}$ and $\chi'_{\mathbf{k}j}$.

Carrying out both the time derivative ∂_t on the right hand side and the momentum operator on the left hand side, i.e. $\mathbf{k} = -i\nabla$, eq. A.9 reduces to the unperturbed eigenvalue equation:

$$\begin{pmatrix} m_e c^2 & c\hbar(\vec{\sigma}\mathbf{k})\\ c\hbar(\vec{\sigma}\mathbf{k}) & -m_e c^2\end{pmatrix}\begin{pmatrix}\chi_{\mathbf{k}j}\\ \chi'_{\mathbf{k}j}\end{pmatrix} = \pm E_k\begin{pmatrix}\chi_{\mathbf{k}j}\\ \chi'_{\mathbf{k}j}\end{pmatrix} \ , \tag{A.12}$$

Hence, $\Psi^{\pm}_{\mathbf{k}j}$ are eigenstates to the energy eigenvalue equation A.12, which leads to two-times-two coupled equations, i.e. two for positive and two for negative energy solutions.

The coupled equations lead to solutions for the 4-component spinor, with the normalization constants A_k^+ and A_k^-:

$$\Psi_{\mathbf{k}j}^+ = A_k^+ \begin{pmatrix} \chi_{\mathbf{k}j} \\ \frac{\hbar c(\vec{\sigma}\mathbf{k})}{E_k+mc^2}\chi_{\mathbf{k}j} \end{pmatrix} \quad , \qquad \Psi_{\mathbf{k}j}^- = A_k^- \begin{pmatrix} -\frac{\hbar c(\vec{\sigma}\mathbf{k})}{E_k+mc^2}\chi'_{\mathbf{k}j} \\ \chi'_{\mathbf{k}j} \end{pmatrix} \tag{A.13}$$

Since the two 2-component spinors are separated regarding positive and negative energy solutions, a suitable representation is $\chi_{\mathbf{k}j} = \chi'_{\mathbf{k}j} = N_k \hat{\mathbf{s}}_j$ with the normalized 2-component spinors: $\hat{\mathbf{s}}_j$:

$$\hat{\mathbf{s}}_1 = \begin{pmatrix} 1 \\ 0 \end{pmatrix} \quad , \qquad \hat{\mathbf{s}}_2 = \begin{pmatrix} 0 \\ 1 \end{pmatrix} \quad , \qquad N_k = 1 \tag{A.14}$$

The normalization constants are obtained by setting the normalization requirement for the 4-component spinors, i.e. $(\Psi_{\mathbf{k}j}^\pm)^\dagger \Psi_{\mathbf{k}j}^\pm = 1$. Thus, the two normalized 4-component spinors are:

$$\Psi_{\mathbf{k}j}^+ = \sqrt{\frac{E_k+mc^2}{2E_k}} \begin{pmatrix} \hat{\mathbf{s}}_j \\ \frac{\hbar c(\vec{\sigma}\mathbf{k})}{E_k+mc^2}\hat{\mathbf{s}}_j \end{pmatrix} \quad , \qquad \Psi_{\mathbf{k}j}^- = \sqrt{\frac{E_k+mc^2}{2E_k}} \begin{pmatrix} -\frac{\hbar c(\vec{\sigma}\mathbf{k})}{E_k+mc^2}\hat{\mathbf{s}}_j \\ \hat{\mathbf{s}}_j \end{pmatrix} \tag{A.15}$$

A.3. Mathematical Properties of the 4-Component Spinors

The normalized 4-component spinors as shown in eq. A.15 can be rewritten by using the relativistic relation $E_k = \sqrt{m^2c^4 + \hbar^2c^2\mathbf{k}^2} = \gamma mc^2$ via

$$\Psi_{\mathbf{k}j}^+ = A \begin{pmatrix} \hat{\mathbf{s}}_j \\ B(\vec{\sigma}\mathbf{k})\hat{\mathbf{s}}_j \end{pmatrix} \quad , \qquad \Psi_{\mathbf{k}j}^- = A \begin{pmatrix} -B(\vec{\sigma}\mathbf{k})\hat{\mathbf{s}}_j \\ \hat{\mathbf{s}}_j \end{pmatrix} \quad , \tag{A.16}$$

with the constants $A = \sqrt{(\gamma+1)/(2\gamma)}$ and $B = (\hbar c)/(mc^2(\gamma+1))$. Furthermore, the following relations for the normalized 2-component spinors hold:

$$(\hat{\mathbf{s}}_j)^\dagger \hat{\mathbf{s}}_{j'} = \delta_{jj'} \ , \qquad \sum_j \hat{\mathbf{s}}_j (\hat{\mathbf{s}}_j)^\dagger = \mathcal{I}_2 \tag{A.17}$$

Thus, the 4-component spinors satisfy the following relations:

$$[\Psi_{\mathbf{k}_0 l}^\pm]^\dagger \Psi_{\mathbf{k}_0 j}^\pm = \delta_{lj} \tag{A.18}$$

$$[\Psi_{\mathbf{k}_0 l}^\mp]^\dagger \Psi_{\mathbf{k}_0 j}^\pm = 0 \tag{A.19}$$

$$[\Psi_{\mathbf{k}_0 l}^\pm]^\dagger \alpha_i \Psi_{\mathbf{k}_0 j}^\pm = \pm \frac{v_i}{c}\delta_{lj} \tag{A.20}$$

$$[\Psi_{\mathbf{k}_0 l}^\mp]^\dagger \alpha_i \Psi_{\mathbf{k}_0 j}^\pm = \hat{\mathbf{s}}_l^\dagger [\sigma_i - (1-1/\gamma)\hat{v}_i(\hat{\mathbf{v}}\vec{\sigma})]\hat{\mathbf{s}}_j = (\mathbf{b}_{lj})_i \tag{A.21}$$

Furthermore, it is convenient to expand relation A.21 to get

$$(\mathbf{A}(\mathbf{r},t)\mathbf{b}_{lj})(\mathbf{b}_{jj'}\mathbf{A}(\mathbf{r},t)) = \delta_{lj'}\left(A_x^2(\mathbf{r},t) + A_y^2(\mathbf{r},t) + \frac{1}{\gamma^2}A_z^2(\mathbf{r},t)\right) \;, \tag{A.22}$$

with $\hat{\mathbf{v}}$ in z-direction, i.e. $\hat{\mathbf{v}} = \hat{\mathbf{z}}$.

The following calculations prove relations A.18 to A.22.

Proof of the 4-component spinor amplitude relation A.18 using the Pauli matrix relation A.7:

$$\begin{aligned}
[\Psi^+_{\mathbf{k}_0 l}]^\dagger \Psi^+_{\mathbf{k}_0 j} &= A^2 \hat{\mathbf{s}}_l^\dagger (\mathcal{I}_2 + B^2\mathbf{k}^2)\hat{\mathbf{s}}_j = \hat{\mathbf{s}}_l^\dagger\left(\frac{\gamma+1}{2\gamma} + \frac{\gamma^2-1}{2\gamma(\gamma+1)}\right)\hat{\mathbf{s}}_j = \hat{\mathbf{s}}_l^\dagger\hat{\mathbf{s}}_j = \delta_{lj}\\
[\Psi^-_{\mathbf{k}_0 l}]^\dagger \Psi^-_{\mathbf{k}_0 j} &= A^2 \hat{\mathbf{s}}_l^\dagger (B^2\mathbf{k}^2 + \mathcal{I}_2)\hat{\mathbf{s}}_j = \hat{\mathbf{s}}_l^\dagger\left(\frac{\gamma^2-1}{2\gamma(\gamma+1)} + \frac{\gamma+1}{2\gamma}\right)\hat{\mathbf{s}}_j = \hat{\mathbf{s}}_l^\dagger\hat{\mathbf{s}}_j = \delta_{lj}
\end{aligned}$$

Proof of the 4-component spinor amplitude relation: A.19

$$[\Psi^\mp_{\mathbf{k}_0 l}]^\dagger \Psi^\pm_{\mathbf{k}_0 j} = A^2\hat{\mathbf{s}}_l^\dagger(-B(\vec{\sigma}\mathbf{k}) + B(\vec{\sigma}\mathbf{k}))\hat{\mathbf{s}}_j = 0$$

Proof of the 4-component spinor relation A.20, using the Pauli matrix commutation relation A.5 and the relativistic momentum relation for plane waves $\mathbf{p} = \hbar\mathbf{k} = \gamma m\mathbf{v}$:

$$[\Psi^\pm_{\mathbf{k}_0 l}]^\dagger \alpha_i \Psi^\pm_{\mathbf{k}_0 j} = \pm A^2 B\hat{\mathbf{s}}_l^\dagger(\vec{\sigma}(\vec{\sigma}\mathbf{k}) + (\vec{\sigma}\mathbf{k})\vec{\sigma})\hat{\mathbf{s}}_j = \pm\frac{\hbar}{2\gamma mc}\hat{\mathbf{s}}_l^\dagger(2\mathbf{k}\mathcal{I}_2)\hat{\mathbf{s}}_j = \pm\frac{\mathbf{v}}{c}\delta_{lj}$$

Proof of the 4-component spinor amplitude relation A.21, using the Pauli matrix relation A.8 and the relativistic relation $\mathbf{p} = \hbar\mathbf{k} = \gamma m\mathbf{v} = \sqrt{E_k^2 - m^2c^4} = mc^2\sqrt{\gamma^2-1}$:

$$\begin{aligned}
&[\Psi^\mp_{\mathbf{k}_0 l}]^\dagger \alpha_i \Psi^\pm_{\mathbf{k}_0 j} =\\
&= A^2\hat{\mathbf{s}}_l^\dagger(\sigma_i - B^2(\vec{\sigma}\mathbf{k})\sigma_i(\vec{\sigma}\mathbf{k}))\hat{\mathbf{s}}_j =\\
&= \hat{\mathbf{s}}_l^\dagger\left(\frac{\gamma+1}{2\gamma}\sigma_i - \frac{(\gamma^2-1)}{2\gamma(\gamma+1)}(\vec{\sigma}\hat{\mathbf{v}})\sigma_i(\vec{\sigma}\hat{\mathbf{v}})\right)\hat{\mathbf{s}}_j =\\
&= \hat{\mathbf{s}}_l^\dagger\left(\frac{\gamma+1}{2\gamma}\sigma_i - \frac{(\gamma-1)}{2\gamma}(2\hat{v}_i(\hat{\mathbf{v}}\vec{\sigma}) - \sigma_i)\right)\hat{\mathbf{s}}_j =\\
&= \hat{\mathbf{s}}_l^\dagger\left(\frac{\gamma+1}{2\gamma}\sigma_i + \frac{\gamma-1}{2\gamma}\sigma_i + \frac{(\gamma-1)}{\gamma}\hat{v}_i(\hat{\mathbf{v}}\vec{\sigma})\right)\hat{\mathbf{s}}_j =\\
&= \hat{\mathbf{s}}_l^\dagger(\sigma_i + (1-1/\gamma)\hat{v}_i(\hat{\mathbf{v}}\vec{\sigma}))\hat{\mathbf{s}}_j = (\mathbf{b}_{lj})_i
\end{aligned}$$

Proof of the 4-component spinor amplitude relation A.22, using the Pauli matrix relations A.7 and A.8:

$$
\begin{aligned}
&\sum_j (\mathbf{A}(\mathbf{r},t)\mathbf{b}_{lj})(\mathbf{b}_{jj'}\mathbf{A}(\mathbf{r},t)) \\
&= \sum_j \mathbf{A}(\mathbf{r},t)\hat{\mathbf{s}}_l^\dagger(\vec{\sigma} - (1-\frac{1}{\gamma})\hat{\mathbf{z}}\sigma_3)\hat{\mathbf{s}}_j\hat{\mathbf{s}}_j^\dagger(\vec{\sigma} - (1-\frac{1}{\gamma})\hat{\mathbf{z}}\sigma_3)\hat{\mathbf{s}}_{j'}\mathbf{A}(\mathbf{r},t) \\
&= \hat{\mathbf{s}}_l^\dagger((\mathbf{A}(\mathbf{r},t)\vec{\sigma})^2 + (1-\frac{1}{\gamma})^2 A_z^2(\mathbf{r},t)\mathcal{I}_2 - (1-\frac{1}{\gamma})A_z(\mathbf{r},t)(\sigma_3(\mathbf{A}(\mathbf{r},t)\vec{\sigma}) + (\mathbf{A}(\mathbf{r},t)\vec{\sigma})\sigma_3))\hat{\mathbf{s}}_{j'} \\
&= \hat{\mathbf{s}}_l^\dagger\left(\mathbf{A}^2(\mathbf{r},t)\mathcal{I}_2 + \left(1+\frac{1}{\gamma^2}-\frac{2}{\gamma}\right)A_z^2(\mathbf{r},t)\mathcal{I}_2 - \left(1-\frac{1}{\gamma}\right)2A_z^2(\mathbf{r},t)\mathcal{I}_2\right)\hat{\mathbf{s}}_{j'} \\
&= \delta_{lj'}\left(A_x^2(\mathbf{r},t) + A_y^2(\mathbf{r},t) + \frac{1}{\gamma^2}A_z^2(\mathbf{r},t)\right)
\end{aligned}
$$

A.4. The Point-Spread Function of the Detection System

As mentioned in Chapter 3.4, the point-spread function (PSF) of the electron detection system is found by recording single electrons and fitting a Voigt profile over their intensity. The analysis of the electrons is done in a multi-step process using analyzing tools in Fiji [77] and Python [78].

A.4.1. Image processing via Fiji

First, the electron image and the dark are opened and subtracted in Fiji:

```
1  open("electron_image.bmp");
2  open("dark.bmp");
3  imageCalculator("Subtract create","electron_image.bmp","dark.bmp");
4  selectWindow("dark.bmp");
5  run("Close");
6  selectWindow("electron_image.bmp");
7  run("Close")
8  selectWindow("Result of electron_image.bmp");
9  run("Brightness/Contrast...");
10 run("Enhance Contrast", "saturated=0.35");
11 run("Close");
```

Here, the "close" commands are used in order to close all the images that are unnecessary for further analysis. After this code, only the dark subtracted electron image is selected in row 8, and its contrast is enhanced (rows 9-11) for better visualization, as shown in fig. 3.6a.

This image is then segmented to find the single electrons:

```
setAutoThreshold("Otsu dark");
run("Threshold...");
setThreshold(3, 255);
run("Convert to Mask");
run("Close");
run("Remove Outliers...", "radius=2 threshold=50 which=Dark");
```

```
7 run("Dilate");
8 run("Erode");
```

Segmentation is implemented using the Otsu method (rows 1-4) and further processed by removing outliers with a pixel radius of 2 (row 6). Finally, in order to get more homogeneous masks, the image is eroded and dilated again (rows 7-8), giving a processed image as shown in fig. 3.6b.

Finally, the electron masks are analyzed, and their center and ellipsoidal fit are determined. The results are then saved in a text file:

```
run("Set Measurements...", "area center fit redirect=None decimal=0");
run("Analyze Particles...", "  show=[Count Masks] exclude clear add
    display");
run("Close");
saveAs("Results", "Results.txt");
```

A.4.2. Single Electron Fitting via Python

In order to analyze the electron image via Python, the following packages have been installed:

```
import numpy as np
from matplotlib import pyplot as plt
from scipy import optimize
import scipy.special as ssp
from matplotlib import cm
import cv2
import scipy.signal as ssig
```

Then, the original electron image as well as the dark image are loaded in grey scale and subtracted, giving a two-dimensional array of floating numbers:

```
imagefile = r'electron_image.bmp'
img = cv2.imread(imagefile, 0)
imgfloat = img.astype(float)
dark = r'dark.bmp'
img_dark = cv2.imread(dark, 0)
img_darkfloat = img_dark.astype(float)
image_dark_cor = img-img_dark.clip(None,img)
image_dark_cor_float = imgfloat-img_darkfloat
```

To load the text file with the saved properties of the electrons, the following commands are used:

```
value_table = r'Results.txt'
rows        = np.loadtxt(value_table, skiprows=1)[:,0]
area        = np.loadtxt(value_table, skiprows=1)[:,1]
centre_xpos = np.loadtxt(value_table, skiprows=1)[:,2]
centre_ypos = np.loadtxt(value_table, skiprows=1)[:,3]
major       = np.loadtxt(value_table, skiprows=1)[:,4]
minor       = np.loadtxt(value_table, skiprows=1)[:,5]
```

The whole image is separated into regions of interest, where a single electron marks the center. However, if two or more electrons are in the same region of interest, both electrons are omitted for the analysis:

```
RoI = 32
centre_xpos_new = np.loadtxt(value_table, skiprows=1)[:,2]
centre_ypos_new = np.loadtxt(value_table, skiprows=1)[:,3]
m = 0
while m < len(centre_xpos):
    for n in range(m, len(centre_xpos)-1):
        if abs(centre_xpos[m]-centre_xpos[1+n]) <= RoI and abs(
    centre_ypos[m]-centre_ypos[1+n]) <= RoI:
            centre_xpos_new[m] = 0
            centre_ypos_new[m] = 0
            centre_xpos_new[1+n] = 0
            centre_ypos_new[1+n] = 0
    m = m+1
centre_xpos_new = np.delete(centre_xpos_new, np.where(centre_xpos_new ==
    0))
centre_ypos_new = np.delete(centre_ypos_new, np.where(centre_ypos_new ==
    0))
```

Now, all electron masks with a minor axis that is not at least 70% of the major axis are omitted since they are likely two electrons close to each other. Thus, new arrays for the center positions are made:

```
for l in range (0,len(minor)):
    if (minor[l]/major[l]) < 0.3:
        centre_xpos_new[l] = 0
        centre_ypos_new[l] = 0
centre_xpos_new = np.delete(centre_xpos_new, np.where(centre_xpos_new ==
    0))
centre_ypos_new = np.delete(centre_ypos_new, np.where(centre_ypos_new ==
    0))
```

All the regions of interest are saved in separate two-dimensional arrays:

```
for i in range(0,len(centre_xpos_new)):
    height_limit_upper =  int(centre_ypos_new[i]-RoI/2)
    height_limit_lower =  int(centre_ypos_new[i]+RoI/2)
    width_limit_left   =  int(centre_xpos_new[i]-RoI/2)
    width_limit_right  =  int(centre_xpos_new[i]+RoI/2)
    globals()['roi'+str(i+1)] = image_dark_cor[height_limit_upper:
    height_limit_lower,width_limit_left:width_limit_right]
    globals()['roifloat'+str(i+1)] = image_dark_cor_float[
    height_limit_upper:height_limit_lower,width_limit_left:
    width_limit_right]
```

The following part of the code defines the two-dimensional Gaussian and applies it to all regions of interest (rows 3-27). Then, the distance from the fitted center to each pixel center is measured and saved in an array. Each of these distances has the data value of the intensity assigned to it (rows 29-34). The values of distances and intensities for all regions of interest are then saved into two large arrays (rows 1-2 and 35-36):

```
large_R_array = np.array([])
large_data_array = np.array([])
def gauss_2d(arg, B, A, wx, wy, xc, yc):
    return B + A*np.exp((-2*((arg[0]-xc)**2)/wx**2)-(2*((arg[1]-yc)**2)/
    wy**2))
for j in range(1, len(centre_xpos_new)):
    roi = globals()['roi'+str(j)]
    x = np.linspace(0, len(roi), len(roi))
    y = np.linspace(0, len(roi), len(roi))
    X, Y = np.meshgrid(x,y)
    x_1d = X.reshape((1, np.prod(roi.shape)))
    y_1d = Y.reshape((1, np.prod(roi.shape)))
    grid = np.vstack((x_1d, y_1d))
    data = roi.reshape((1, np.prod(roi.shape)))
    centre = np.where(roi==max(data[0]))
    guessB = min(data[0])
    guessA = max(data[0])
    guesswx = 0.5
    guesswy = 0.5
    guessxc = centre[1][0]
    guessyc = centre[0][0]
    guess = (guessB, guessA, guesswx, guesswy, guessxc, guessyc)
    bnds_lower = np.array([0, min(data[0]), 0.1, 0.1, 0, 0 ])
    bnds_upper = np.array([np.mean(data[0]), min(data[0])+max(data[0]),
    len(roi), len(roi), len(roi), len(roi) ])
    bnds = np.vstack((bnds_lower,bnds_upper))
    popt_gauss_2d, pcov_gauss_2d = optimize.curve_fit(gauss_2d, grid,
    data[0],guess, bounds = bnds)
    globals()['parameters_roi'+str(j)] = popt_gauss_2d
    globals()['parameters_uncertainty_roi'+str(j)] = np.sqrt(np.diag(
    pcov_gauss_2d))

    roifloat = globals()['roifloat'+str(j)]
    datafloat = roifloat.reshape((1, np.prod(roifloat.shape)))
    datafloat = datafloat/sum(datafloat[0])
    X1, Y1 = (X-popt_gauss_2d[4]), (Y-popt_gauss_2d[5])
    R_matrix = np.sqrt(X1**2+Y1**2)
    R_array = R_matrix.reshape((1, np.prod(R_matrix.shape)))
    large_R_array = np.append(super_R_array, R_array[0])
    large_data_array = np.append(super_data_array, datafloat[0])
```

Next, the region of interest is made even smaller since it can already be seen that the fitted two-dimensional Gaussian profiles are much smaller, and therefore, many data points use unnecessary computational memory:

```
R_array_new=np.array([])
img_array_new = np.array([])
for i in range(0, len(super_R_array)):
    if super_R_array[i]<10:
        R_array_new= np.append(R_array_new, super_R_array[i])
        img_array_new=np.append(img_array_new, super_data_array[i])
```

Now, a Savitzky-Golay filter [79] is applied to smooth out the data. Therefore, a sorting rule for the two arrays has to be implemented first:

```
sorting = R_array_new.argsort()
r = px_value_MCP*R_array_new[sorting]
c = img_array_new[sorting]
c_smoothed = ssig.savgol_filter(c, 601, 3)
```

Ultimately, a Voigt profile is fitted over the smoothed data:

```
def V(x, alpha, gamma, Offs_V, Amp_V):
    sigma = alpha / np.sqrt(2 * np.log(2))
    return Offs_V + Amp_V*np.real(ssp.wofz((x + 1j*gamma)/sigma/np.sqrt(2)))/sigma/np.sqrt(2*np.pi)
popt_c_V, pcov_c_V  = optimize.curve_fit(V, r, c_smoothed,guess_V)
```

A.5. Magnitude Estimations for Phase Modulation

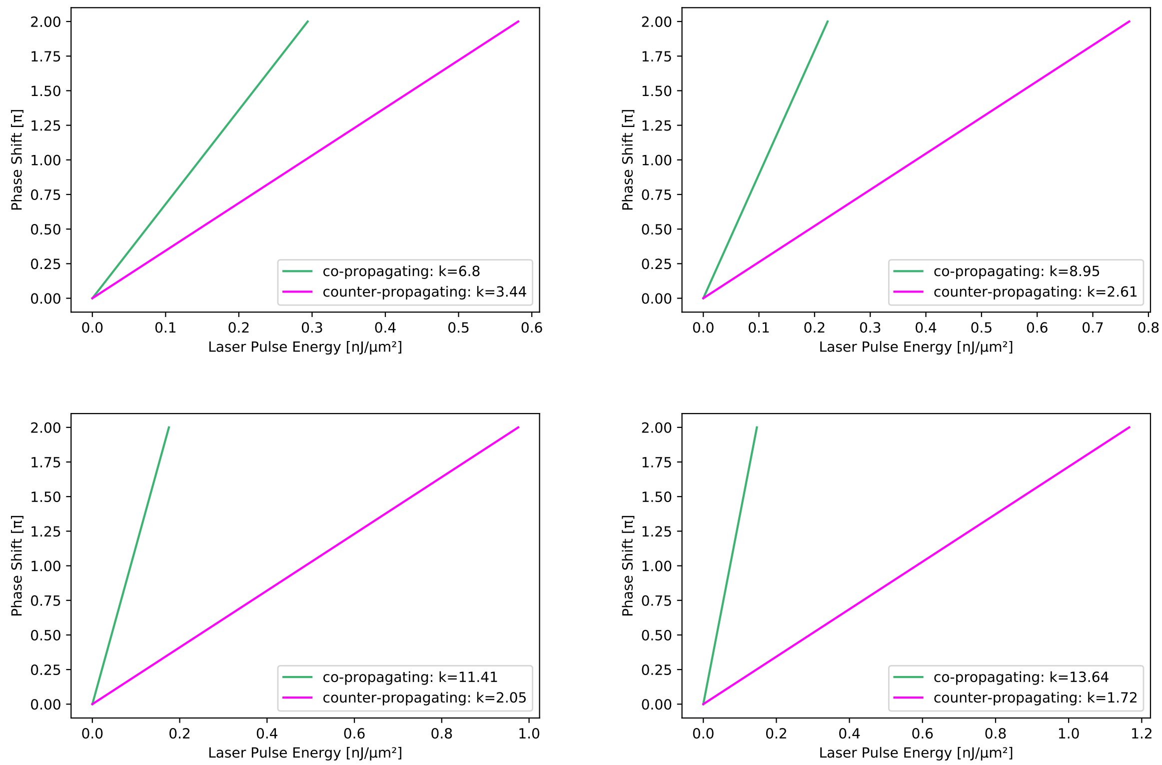

Figure A.1.: Magnitudes of the phase modulation versus the laser pulse energy per area. The electron acceleration energies are 30keV (top-left), 100keV (top-right), 200keV (bottom-left), and 300keV (bottom-right). The slopes k, such that $\varphi(E_L) = kE_L$, are written in the legend of the respective image.

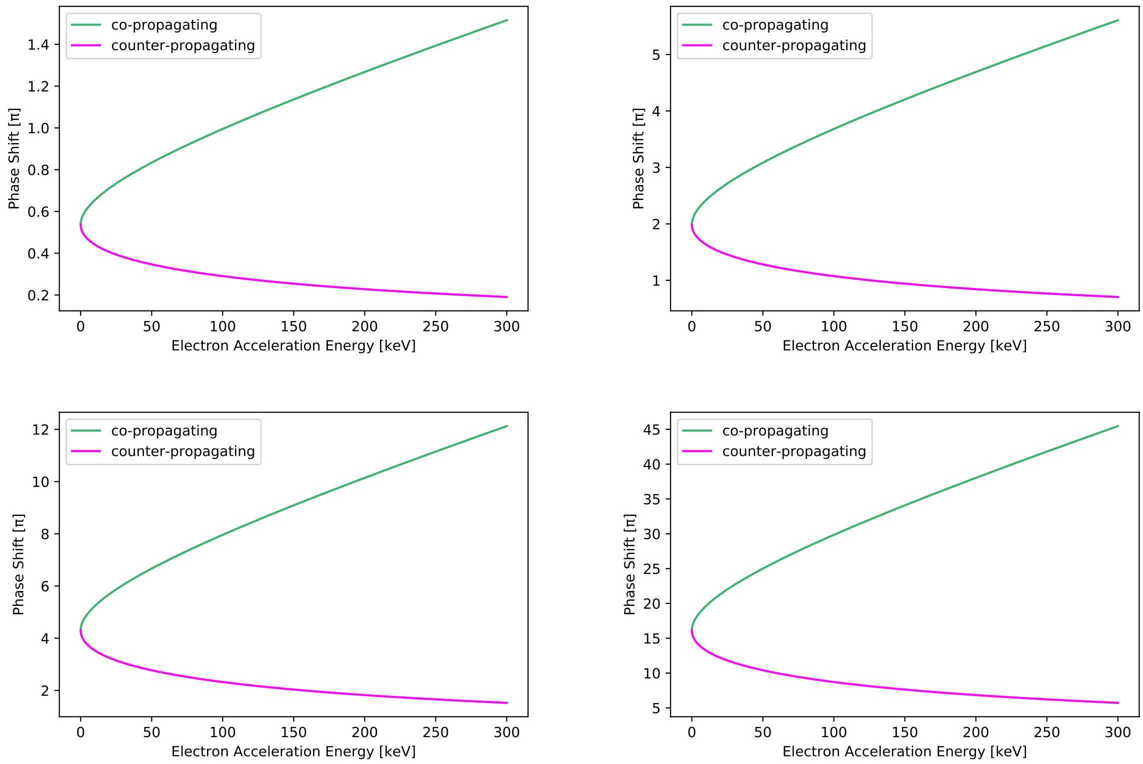

Figure A.2.: Magnitude of the phase shift versus the electron acceleration energy with a laser pulse energy per μm^2 of 100nJ (top-left), 370nJ (top-right), 800nJ (bottom-left) and 3μJ (bottom-right).